Double-Sided Arc Welding
of
AZ31B Magnesium Alloy Sheet

by

Gerald Shuck

A thesis
presented to the University of Waterloo
in fulfillment of the
thesis requirement for the degree of
Master of Applied Science
in
Mechanical Engineering

Waterloo, Ontario, Canada, 2013

AUTHOR'S DECLARATION

I hereby declare that I am the sole author of this thesis. This is a true copy of the thesis, including any required final revisions, as accepted by my examiners.
I understand that my thesis may be made electronically available to the public.

Gerald N. Shuck

Abstract

Magnesium alloys are of interest to the automotive industry because of their low density, high specific strength and potential to reduce overall vehicle weight and fuel consumption. In order to incorporate more magnesium components into automotive structures, efficient welding and joining techniques must be developed. Specifically, an efficient method of making butt-joint configuration welds must be found in order to facilitate the use of sheet magnesium alloys in the form of tailor-welded blanks for structural applications. However, existing welding processes, such as RSW, GTAW, GMAW, laser and hybrid laser-arc each have disadvantages when applied to the welding of magnesium alloy sheet in the butt-joint configuration.

The relatively new double-sided arc welding (DSAW) process has been shown to be capable of producing high quality, full-penetration, conduction-mode, fusion welds in aluminum alloy sheet, for tailor-welded blank applications. The DSAW process has not yet been applied to AZ31B magnesium alloy, which has thermo-physical and oxide forming properties similar to those of aluminum alloys. Therefore, in this study, the weldability of AZ31B magnesium alloy sheet, using the DSAW process has been explored.

Experimental, full-penetration, conduction-mode, butt-joint configuration welds were made in 2 mm thick, rolled AZ31B-H42 magnesium alloy sheet. The range of primary parameters of welding speed and welding power resulting in visually acceptable welds was determined. Acceptable welds have been produced using welding speeds ranging from 12 mm/s to 100 mm/s and welding powers from 1.6 kW to 8.7 kW. The influence of these parameters on the appearance, geometry, mechanical properties and microstructure of the resulting welds was investigated.

Optimal appearance, geometric profile and mechanical properties were obtained at the lowest welding speeds and powers. Under these conditions, mechanical properties of the weld metal were equivalent to those of the fully annealed (0-temper) base metal. However, progressive deterioration in appearance, geometry and mechanical properties occurred at higher welding speeds and powers.

The deterioration in mechanical properties was associated with 2 microstructural defects that were observed in welds made at higher welding speeds and powers: 1) the formation of larger amounts of $Mg_{17}Al_{12}$ β-phase particles, in undesirable connected morphology, at the grain boundaries, and 2) the formation of solidification shrinkage micro-porosity at these same inter-granular locations.

This research demonstrates that the DSAW process is capable of producing acceptable quality, full-penetration, conduction-mode, butt-joint welds in AZ31B magnesium alloy sheet at welding speeds up to 100 mm/s. However, in order to achieve the highest quality welds, low welding power, and, low welding speed, should be used. The highest quality welds were produced in the AZ31B magnesium alloy sheet using a welding speed of 12 mm/s and a welding power of 1.6 kW.

Acknowledgements

I would like to acknowledge my colleagues from the Centre for Advanced Materials Joining (CAMJ) group within the Mechanical Engineering Department at the University of Waterloo for the help and assistance freely given in the course of this work. I am particularly grateful to my supervisor, Professor David C Weckman for his guidance, support and patience during the 2 years spent working on this research.

Table of Contents

List of Figures

List of Tables

Chapter 1

Introduction

1.1 Light Alloys for Automotive Applications

For many years, automotive manufacturers have pursued strategies to achieve better fuel economy in the vehicles they produce. An important approach to improving fuel efficiency has been to reduce the overall mass of the vehicle and this has involved using lighter weight materials in all components wherever possible. Lightweight structural alloys such as aluminum and magnesium have been the focus of much research as candidates to replace heavier steel in many different automotive components [1]. Table 1.1 lists some relevant properties of representative alloys of aluminum, magnesium and steel. The difference in these properties, between the three materials, is the driving force behind the interest in increasing the use of light alloys in automotive structures.

Table 1.1: Relevant structural properties of magnesium, aluminum and steel. Source: ASM Handbook [2].

Property	Magnesium AZ31B	Aluminum 5182	Steel 1025
Density (g/cm^3)	1.77	2.65	7.8
Yield stress (MPa)	220	250	300
Specific strength (MNm/kg) (yield stress / density)	124	94	38

Comparing the specific strengths of the three materials strongly suggests that magnesium is the better choice from a strength-to-weight point of view. Of course, this is an over simplification and the case for magnesium is not quite so compelling. Issues of cost, service temperature suitability and manufacturability have to be considered. Nonetheless, the fact that magnesium has a very low density and reasonable strength makes it an attractive choice for use in weight sensitive applications.

Automotive parts produced by casting processes have been among the first to undergo a transition from ferrous to light alloys. Cast iron automotive components have largely been replaced by aluminum castings unless very high temperature service is required. Further evolution is occurring as aluminum is replaced by magnesium alloys in some components such as transmission housings, oil pans, valve covers, seat frames, instrument panel frames and other internal parts [3], [4]. Volkswagen in Europe and General Motors in North America both use up to 20 kg of magnesium alloy components per vehicle, according to one alloy supplier, Magnesium Elektron [5].

Cast components have been among the first candidates to be considered for weight reduction because their mass is often considerable. The casting process imposes minimum wall thicknesses that are often greater than those required purely for mechanical strength. Hence, castings often end up by being stronger than necessary, at least in some places. This is particularly true of cast iron, with its high density and strength, compared to aluminum or magnesium [6].

The use of wrought semi-finished forms of light alloys such as extrusions and rolled sheet in automotive structures has seen much slower progress [7]. A small number of more expensive, low production volume cars have been designed with all aluminum body shells. Examples include the Audi A8, Acura NSX, Jaguar XJ & XK models and the 2013 Range Rover. Magnesium panels have only yet been seen in exotic, specialty vehicles. Further significant reduction in vehicle mass could be achieved if some of the sheet steel used in automobiles could be replaced with aluminum or better yet, magnesium alloys. This has been slow to realize, with mass-market vehicle manufacturers incorporating sheet aluminum only in the form of hood and trunk panels [8]. No examples could be found of magnesium alloys presently being used in body panels of modern, mass-market vehicles, although manufacturers continue to explore the possibilities [9]. Figure 1.1, taken from Friedrich [7], illustrates the path of anticipated progression from using magnesium to make castings for interior components, to gradually increasing its use to include sheet metal components. According to Friedrich, Volkswagen expects to see the progression towards the use of sheet magnesium in automobiles as occurring over a time period greater than 10 years.

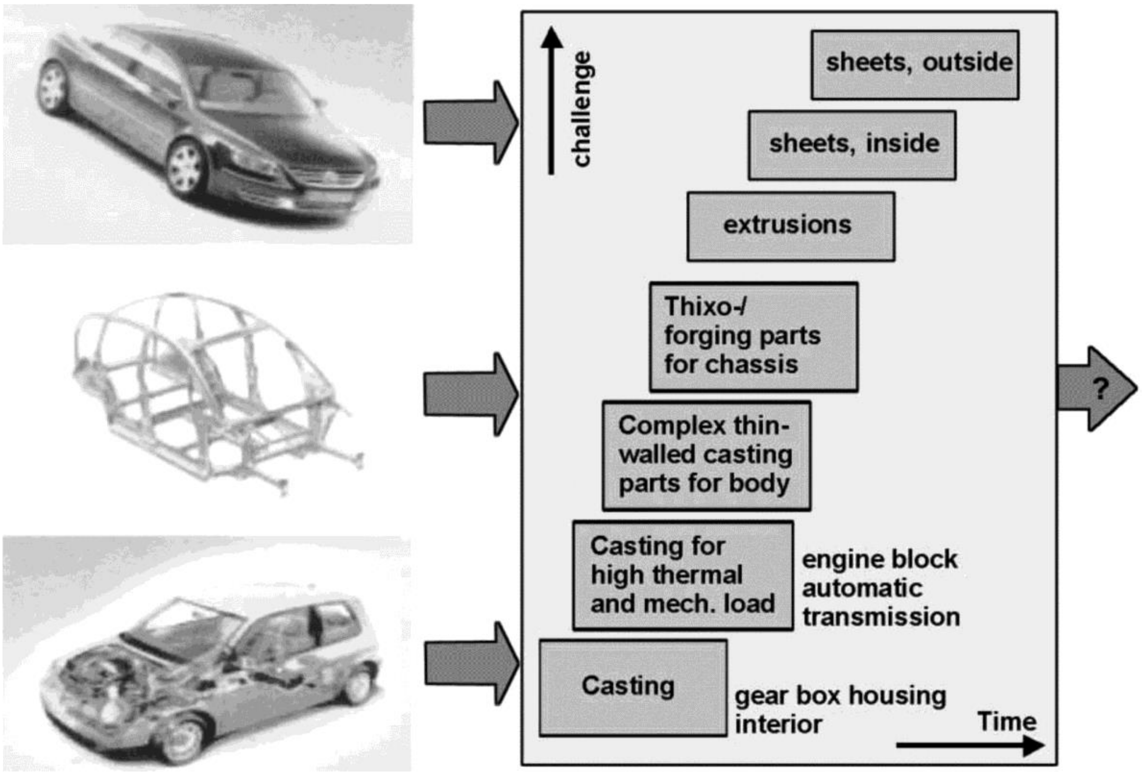

Figure 1.1: Progression of increasing use of magnesium in vehicle manufacture. (Adapted from Friedrich **[7]** and used with permission)

1.2 Obstacles to Increased use of Wrought Magnesium Alloys

There are several obstacles that impede the increased use of magnesium sheet products in the automotive industry. The most obvious is the present cost difference between a typical magnesium sheet and a sheet of mild steel. However, cost is dependent on production volume and it is reasonable to expect the presently high cost of magnesium alloy sheet to come down considerably, should production volume increase [1]. Moreover, direct material cost comparisons, whether on the basis of weight, volume or even specific strength, is deceiving. Account has to be taken of the overall cost of manufacturing a given design [10].

Engineering obstacles to the increased use of sheet magnesium alloys in automobiles include poor room temperature formability [11], corrosion susceptibility [12] and a lack of expertise in welding and joining techniques [13]. One essential area of welding and joining technology that is presently lacking is the ability to make butt-joints in thin magnesium alloy sheet. Such joining of sheet components is required, for example, to make tailor-welded blanks for subsequent forming into structural components. Since the use of more tailor-welded blanks is likely to be a future trend [14], an efficient method of joining sheet magnesium, in the butt-joint configuration, is a prerequisite to its increased use by the auto and other transportation vehicle industries.

1.3 Considerations for Welding Magnesium Alloys

Magnesium has several important physical characteristics that affect its weldability. Among them are the thermo-physical properties listed in Table 1.2 These properties are meaningful when compared to those of a typical aluminum alloy and a low carbon steel.

Table 1.2: Thermo-physical properties of magnesium, aluminum and steel that affect the weldability of the alloy. Sources: ASM Handbook [2], Smithell's Light Metals Handbook [15] and recent measurement experiments [16].

	Magnesium AZ31B	Aluminum 5182	Steel 1025
Melting point (liquidus) (K)	903	911	~1770
Boiling point (K)	1370	2670	2750
Thermal conductivity, k (W/m·K)	96	123	40
Specific heat, C_p (J/kg·K)	1050	904	660
Density, ρ (kg/m^3)	1770	2650	7800
Thermal diffusivity, α (m^2/s)	52×10^{-6}	51×10^{-6}	7.8×10^{-6}
Coef. of thermal expansion (1/K)	26×10^{-6}	26×10^{-6}	14×10^{-6}

1.3.1 Thermal Properties

Referring to Table 1.2, one of the most significant thermal characteristics of magnesium is that the melting and boiling points are very close together. This means that fusion welding is possible, provided the liquid is heated to within only a narrow temperature range between 903 K (630 °C) and 1370 K (1100 °C). The heat input has to be carefully controlled to maintain a temperature in this range. It would be very easy for the heat from any fusion welding process to raise the temperature of the metal above 1370 K (1100 °C) and for the metal to boil away. If this occurs, several consequences are possible: 1) the boiling liquid metal will spatter over the weld and welding equipment, 2) magnesium may condense on cooler surfaces adjacent to the weld, 3) magnesium vapour may escape the shielding gas envelope and turn into white smoke, as magnesium oxide welding fume or, in the extreme, 4) a magnesium fire may be ignited.

The thermal conductivity of magnesium is somewhat lower than that of aluminum, but together with a lower density and only slightly higher specific heat, this means that less heat is required to form and maintain a molten weld pool. This characteristic is described by the composite property, *thermal diffusivity*, which is defined as follows:

$$\alpha = \frac{k}{\rho \cdot C_p} \tag{1}$$

where α is the thermal diffusivity (m^2/s), k is the thermal conductivity (W/m·K), ρ is the density (kg/m^3) and C_p is the specific heat (J/kg·K). Thermal diffusivity is easier to measure experimentally than thermal conductivity. It is also a more useful measure of the overall requirement for heat input in a fusion welding process, for a given material.

The coefficient of thermal expansion of magnesium is high, similar to that of aluminum, and this implies that distortion could be a problem in welding. Consequently, welding jigs and fixtures need to be substantial and other techniques to alleviate distortion may need to be applied. The welding of thin magnesium alloy sheet is particularly susceptible to distortion problems.

1.3.2 Chemical Reactivity

Magnesium is well-known to be a highly reactive metal that will burn intensely in the presence of air if it becomes sufficiently hot to initiate combustion. To prevent fires, care must be taken to ensure adequate shielding of the molten weld pool surface with an inert shielding gas. Fine magnesium particles are used in pyrotechnics and are recognized as a fire hazard in machining and grinding operations involving magnesium alloys [17].

It is also widely known that magnesium corrodes rapidly in a damp environment. Bare magnesium items do not retain their shiny lustrous appearance for long, even in mild indoor conditions [12]. The magnesium metal initially reacts with atmospheric oxygen to form a thin layer of magnesium oxide, according to:

$$Mg + \frac{1}{2}O_2 \rightarrow MgO \tag{2}$$

This reaction occurs quickly and the surface film, after 10 s in dry air, has been measured to be approximately 2 nm thick [18]. Unlike aluminum, the oxide layer formed on magnesium does not constitute a passivating protective barrier to further corrosion [19]. This is attributed to the reaction products having a Pilling-Bedworth ratio of 0.81. The thin layer of magnesium oxide is porous to oxygen molecules and allows for the reaction to continue, thickening the oxide layer until it becomes a visible, dull grey skin, 100 nm thick, several days later [18]. The oxide layer is also porous to water molecules and allows a second hydration reaction to occur if any water vapour molecules are present:

$$Mg + 2H_2O \rightarrow Mg(OH)_2 + H_2 \tag{3}$$

Hydrogen gas is evolved in this reaction and small bubbles can be seen to form on the surface of clean magnesium, a few seconds after immersion in distilled water. The surface layer that builds up on magnesium is, therefore, a combination of magnesium oxide and magnesium hydroxide. In a dry environment, the layer is predominantly magnesium oxide, but becomes predominantly magnesium hydroxide as more water vapour is available [20]. The magnesium hydroxide reaction product has a Pilling-Bedworth ratio of >2 and therefore forms a flakey, spalling surface layer. Magnesium hydroxide is hygroscopic and attracts more water molecules from the air, to form $Mg(OH)_2 \cdot 3H_2O$. The 3 water molecules then react preferentially with more magnesium and the corrosion continues [20]. Spalling of the corrosion products from the surface leads to fresh magnesium metal being exposed to more corrosion. The surface layer continues to grow and eventually forms a loosely adhering white powdery layer.

The corrosion products described above are very harmful to any fusion welding process for several reasons. They neither dissolve nor melt in the liquid magnesium weld pool due to their high melting temperatures and they contaminate the weld by introducing discontinuities [21]. They are also abundant sources of elemental hydrogen that will readily dissolve in the molten metal weld pool during the welding process, leading to hydrogen porosity in the solidified weld metal. Accordingly, great care is required to remove all traces of hydrated oxides from the surface of magnesium alloy sheets prior to fusion welding. Careful shielding of the molten weld pool is also essential to prevent any further contact with atmospheric oxygen or humidity in the air during the welding process [21].

1.4 Mechanical Properties of Fusion Welded AZ31B-H24 Magnesium Alloy

Magnesium crystallizes into a hexagonal close packed (HCP) structure. At room temperature, slip occurs in the basal {0001} planes and twinning occurs in the pyramidal {1012} planes. Adjacent grains are unlikely to be favourably aligned to allow much deformation and inter-granular cracks may form. Consequently, magnesium alloys have low ductility at room temperature [22]. The AZ31B alloy typically exhibits maximum elongations of about 10% - 12% in the H24 temper; perhaps rising to about 15% -18% in the annealed condition. These values are much lower than those of mild steel, which may easily exceed 30% [22].

At temperatures above 225°C, magnesium alloys have better ductility, as the more numerous prismatic {1100} planes become active and allow slip to occur in more directions. Adjacent grains are then more likely to have favourably aligned slip planes and ductility is much improved [22]. For this reason, magnesium sheet is almost always formed at elevated temperatures.

Magnesium alloys can rely on various strengthening mechanisms in order to achieve useful levels of mechanical strength. Solid-solution strengthening, by the addition of small amounts of aluminum or zinc is a common method of improving the strength of the pure metal. Strengthening by grain size reduction is another method to improve strength in wrought forms like rolled sheet [17]. Precipitation hardening by the formation of small, finely dispersed particles of hard intermetallic compounds is a third method of improving the mechanical properties of commercial magnesium alloys [23] [24]. The benefits that these grain size and precipitation strengthening techniques impart to the alloy are lost when the magnesium alloy is fusion welded, as the fusion zone metal is melted and re-cast. Partitioning and micro-segregation of the alloy components occurs upon solidification, so that locally, there is either too little or too much solute concentration for optimal solid-solution strengthening [25].

The fusion zone microstructure in an AZ31B magnesium alloy weld is normally dendritic, with rounded, non-facetted dendrites of solute-lean magnesium, surrounded by material much richer in solute. Most welding processes will produce large dendrites, but smaller dendrites are possible if the cooling rate is fast enough. The very last metal to freeze will have the highest solute concentration and may approach the eutectic composition of Mg -33wt%Al. Normally, coupled growth of the eutectic does not occur. Rather, a divorced eutectic will typically form with separate solute-rich α-magnesium and a brittle intermetallic β-phase, $Mg_{17}Al_{12}$ [17]. The β-phase forms along grain boundaries and seriously degrades the ductility of the alloy. Solidification shrinkage of magnesium can be enough to cause hot cracking in the resulting welds, especially in regions where the aluminum content is less than 6 wt% Al [25].

The adjacent partially melted zone and heat affected zone (HAZ) of an AZ31B magnesium fusion weld will undergo grain growth, to varying degrees, depending on the amount of heat conducted into the surrounding metal. Therefore, the strengthening derived from grain refinement or strain hardening during mechanical processing is also lost in the immediate vicinity of the weld. Finely dispersed second-phase particles of Mn_5Al_8 in the HAZ coalesce and grow, as a result of heating, to become fewer and larger, so that the precipitation hardening effect is also diminished [26].

1.5 Fusion Welding Processes for Magnesium Alloys

Wrought magnesium semi-finished forms have not traditionally been joined by welding, due to the considerations discussed in the preceding two sections. Joining by the use of aluminum rivets, was the process of choice for assembling sheet magnesium components used by the aerospace industry up to the 1960s [27]. However, riveting is a labour intensive process and some suitable welding technology was needed if magnesium was to gain acceptance outside of the defense industry, where cost is a lower priority.

Fusion welding of magnesium alloys grew out of the need to repair defects in magnesium alloy castings. Experience in making these repairs has shown that many magnesium alloys can be successfully welded, as long as proper methods are employed to account for the particular characteristics of magnesium alloys. These methods can be summarized into the following 4 points [21]:

1. Precise control of the heat input into the weld.
2. Scrupulous attention to the cleanliness of the weld.
3. Total shielding of the weld pool from the atmosphere.
4. Some form of mitigation against shrinkage distortion.

Gas Tungsten Arc Welding (GTAW) has been considered the cleanest of the traditional welding heat sources and as such, has been the natural choice of technology for welding such reactive metals as magnesium. It can be carried out manually, but great skill is required to manipulate the weld pool and therefore some form of automated welding system is more commonly used. Autogenous welds are possible if the fit-up is carefully prepared, otherwise filler metal strips can be laid in the groove [21].

Gas Metal Arc Welding (GMAW) has been the preferred technology for the welding of steel, due to the high deposition rates that are possible, the ease of automation and the energy efficiency of the process. However, the GMAW process suffers from inherent problems, if applied to magnesium. The filler wire must travel through the length of the arc column, during which time it is heated above its boiling point, resulting in spattering and evaporation loss. Research to adapt this process for magnesium alloys, using novel pulsed waveforms is ongoing [28]. Second is the problem of economically producing the filler wire. Magnesium wire is presently drawn down to size in a costly and time consuming process, involving many small draw steps with interspersed heat treatments [29].

Resistance Spot Welding (RSW) of magnesium alloys is quite feasible, given that the electrical conductivity is between that of aluminum and steel. However, the results can be inconsistent because the process parameters are very critical [30]. Also, it should be noted that the RSW process is applicable only to lap-joints, not the butt-joint configuration, required for making tailor welded blanks.

Laser welding of magnesium has received much attention over the years, as researchers attempt to take advantage of the high welding speeds theoretically possible with this high energy density heat source, operating in the keyhole mode [13]. However, laser welding systems are very capital intensive and laser welding speeds are presently limited by the tendency to form gas porosity and undercut defects at high speed when welding magnesium alloys [31]. Various combinations of laser-arc hybrid heat sources have also been investigated and the results look promising, as the synergistic effect between the laser beam and the arc becomes better understood [32].

All of the above welding technologies are normally applied to one side of the work-piece. When welding magnesium sheet material, however, some form of shielding protection from the atmosphere is also required for the back surface of the sheet. This may involve a variety of different arrangements, but they all require access to the reverse side of the sheet. One relatively new welding method that could be used to advantage to join magnesium sheet in the butt-joint configuration, while overcoming many of the deficiencies of other welding processes when used to weld magnesium, is the Double-Sided Arc Welding (DSAW) process.

1.6 Double-Sided Arc Welding (DSAW)

The Double-Sided Arc Welding (DSAW) process was invented and patented by Zhang and Zhang [33], at the University of Kentucky in 1999. Shown schematically in Figure 2, it involves the use of two welding torches, one on each side of the work. The torches are connected in series to one power supply, forming one welding circuit with an arc established between the two torches. When the work is fed through the arc column, the arc splits into 2, with the sheet material in between. The welding current passes through the thickness direction of the metal, thereby applying heat and shielding to the top and bottom surface of the joint simultaneously.

The DSAW system can be configured to use either GTAW or Plasma Arc Welding (PAW) torches. Plasma Arc Welding (PAW) is a further development of GTAW in which the arc plasma is directed, in the form of a jet, through a small orifice at the tip of the welding torch [34]. PAW torches are more fully described in the following Sub-Section 1.6.1.

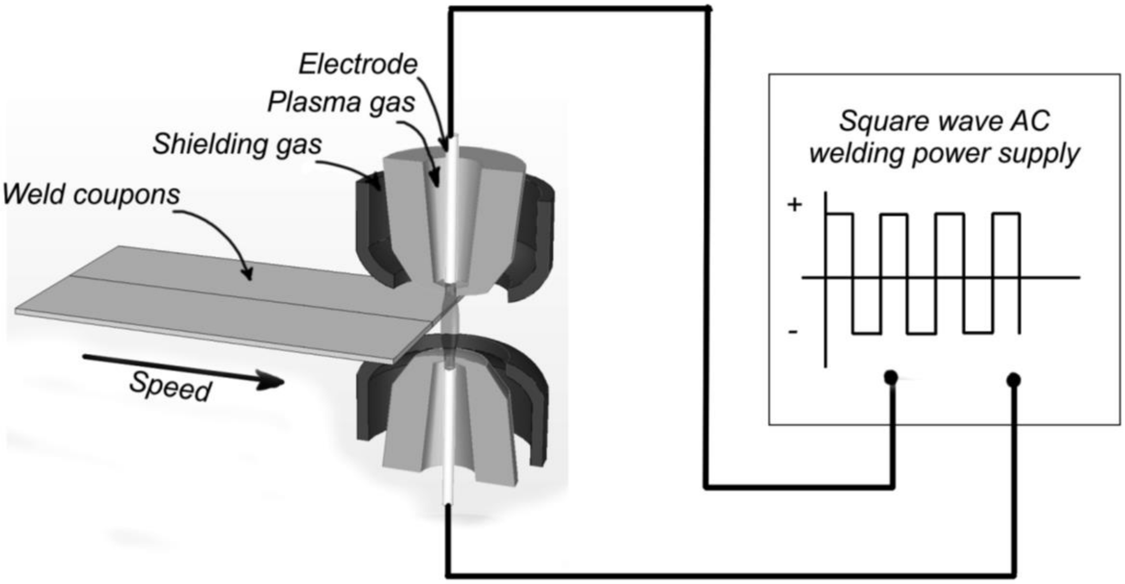

Figure 1.2: Schematic representation of the double-sided arc welding process with 2 PAW torches.

The DSAW process was originally applied by Zhang & Zhang [35] to making butt-joint welds in thick aluminum plates in the vertical-up position, using keyhole-mode welding. Applications include the welding of process industry tanks and other vessels as well as ship hull plate made in a range of aluminum, steel and stainless steel alloys [35]. It was subsequently adapted to the horizontal position, conduction-mode welding of AA5182 aluminum alloy thin sheet by Kwon & Weckman and others at the University of Waterloo [36] [37] [38] [39] [40] [41]**.**

The DSAW process has several inherent advantages that can be usefully applied to the welding of thin magnesium sheet in the butt-joint configuration, as envisioned in this study:

1. The process can produce a very symmetrical weld with little or no angular distortion of the sheet material [42].
2. Complete joint penetration can be achieved with a fairly narrow weld, since there is a heat source on both surfaces of the metal.
3. Both sides of the weld can have the same high quality surface appearance.

4. The electric arc that provides the heat source is also responsible for the cathodic cleaning action on the surface of the sheet; an important advantage that does not occur with a laser heat source [43]**.**
5. The process uses mature technology that is already available to industry and is well understood. Investment in capital intensive equipment is not required in order to use the process. An existing welding power supply can be connected to appropriate torches for minimal cost, as an inexpensive way to experiment with the process.

Many variations of heat sources have been investigated in the last decade in order to advance the state of the art of welding magnesium alloys. So far, no studies have been published on the joining of magnesium alloy sheets using the DSAW process.

1.6.1 Plasma Arc Welding (PAW)

Plasma Arc Welding (PAW) is a further development and refinement of GTAW that involves directing a stream of ionized argon plasma past a tungsten electrode and through a small orifice in the welding torch tip, onto the weld surface. In this way, the arc is constrained into a narrow jet of plasma and a higher energy density is achieved. The plasma arc is narrower and more columnar in shape than the unconstrained GTAW arc, which is typically bell-shaped. PAW torches produce a high energy-density heat source, without the high costs associated with a laser system. They are capable of operating in the conventional conduction welding mode and also the keyhole welding mode, when the power is increased [44].

Figure 1.3 shows the construction details of a PAW torch and illustrates the principle of operation. Plasma gas passes through the narrow passage between the electrode tip and the torch body. Starting the plasma arc requires a pilot arc to be struck between the electrode and the torch body.

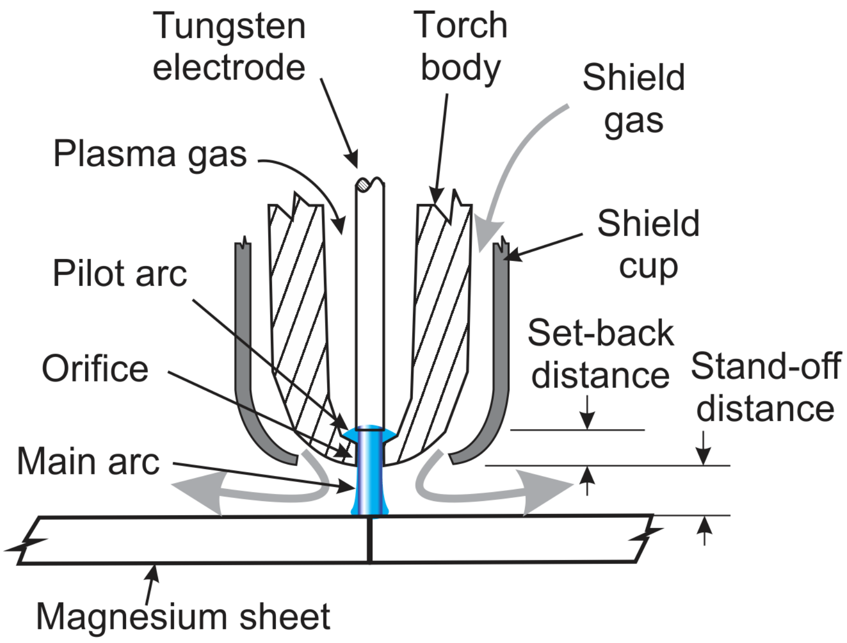

Figure 1.3: Detail of a PAW torch.

The pilot arc heats the plasma gas to an ionized, conducting state. From this point, the jet of plasma gas is an electrical conductor and the main arc can then switched on. The main welding arc current flows between the electrode, through the conducting jet of plasma, and the work-piece [34].

The added complexity of the PAW system brings with it another set of welding process variables that need to be established and controlled. However, the DSAW system takes advantage of the characteristics of the PAW torch to permit a relatively long welding arc to be easily switched on and off. The flow of plasma gas through the orifice involves the considerations of orifice geometry, plasma gas pressure and plasma gas flow rate. These variables have been found to be critical to the success of the process [45]. The arc length is the sum of the torch to workpiece distance (referred to as the stand-off distance) and the distance between the electrode and the orifice (known as the set-back distance) [34]. In the interests of process efficiency, a short arc is desirable, in order to keep the arc voltage as low as possible for a given current. There are practical limits to how short the arc can be set. Small set-back distances require the electrode tip to be ground to a truncated cone in order not to contact the orifice [36].

These narrowed electrode shapes do not conduct heat away from the tip as well as blunt electrodes. They are prone to the electrode tip melting into a ball-shaped end, with possible electrical short-circuiting between the electrode and the torch body [46]. The torch stand-off distance also has a lower limit. There must be sufficient distance between the torch and the weld pool surface to prevent any possibility of short-circuiting between the torch body and the work-piece.

PAW torches are capable of achieving high energy densities that approach those of lasers and are capable of operating in both conduction-mode and keyhole-mode, at higher powers [34]. In keyhole mode, they can produce deep, narrow welds at high welding speeds. PAW process equipment is available at considerably lower capital cost than equivalent size laser systems. For this reason, it is an attractive alternative to laser welding. However, the plasma-arc is not as stable as a laser beam and requires careful adjustment of parameters. Frequent maintenance of the electrode and plasma orifice is also required [47].

1.6.2 Arc Physics

It has long been recognized that the heat generated in a welding arc is not shared equally between the anode and the cathode surfaces. In a DC welding arc, about 70% of the heat is produced at the anode, where the electrons give up their kinetic, thermal and work function energies to the surface of the material they strike [43]. For this reason, the workpiece is often made to be the anode (referred to as DC Electrode Negative or DCEN) when GTAW welding. This arrangement takes advantage of the anode heat, rather than have it wasted in the tungsten electrode.

There is another physical process, referred to as cathodic cleaning or cathodic etching, which is important when fusion welding aluminum and magnesium alloys. These alloys have tenacious coherent oxide surface layers, with melting points well above the melting point and even boiling point of the alloy. Cathodic cleaning occurs on the cathode surface and involves the stripping away of the solid surface oxides from the metal [48]. The precise mechanism behind cathodic cleaning is still the subject of investigation and debate, but it is likely to involve electrons leaving the electrically conducting cathode surface and dislodging the attached non-conducting oxide layer on the way out. Another theory suggests that the oxide layer is removed as a result of the bombardment of the cathode surface by the more massive positive argon ions from within the plasma gas [43]. When welding alloys such as aluminum and magnesium, it is possible to make the work-piece the cathode (referred to as DC Electrode Positive or DCEP), in order to promote cathodic cleaning of the weld surface. In this case, a higher welding power is used, to compensate for the lower heat in the cathode and a heavier tungsten electrode in a water-cooled torch is used to carry away the extra heat evolved at the anode [47].

1.6.3 Variable Polarity Wave-forms in Welding

In order to take advantage of both anode heat and cathodic cleaning simultaneously, some form of alternating polarity can be used. In the past, this has involved using a simple welding transformer to produce a 60 Hz line frequency, sinusoidal AC waveform. The resulting welding circuit spends equal time in the electrode-negative and electrode-positive modes, giving a large degree of cathodic cleaning and heat balanced between workpiece and electrode. However, the sinusoidal waveform is not ideal for welding, because a significant fraction of the AC cycle time is spent at low current when the polarity crosses zero. The arc extinguishes during these low current periods and is, therefore, discontinuous and not very stable [47].

Modern power electronic components have allowed welding power supplies to produce square-wave AC outputs, which have almost no switch-over time, as shown in Figure 1.2 [49]. The arc is essentially continuous and switches polarity without extinguishing. Further, the square-wave is not restricted to the 60 Hz line frequency, nor must it be balanced in time and magnitude. Most welding power supplies now permit frequency adjustment from several tens, to several hundred Hz. More importantly, they also provide pulse width modulation to control the fraction of time spent in electrode positive or electrode negative modes. The fraction of time spent in electrode negative mode is denoted by θ, and is calculated thus:

$$\theta = \frac{t_{EN}}{t_{EN} + t_{EP}} \tag{2.1}$$

where t_{EN} is the time spent in a periodic square wave form with electrode negative and t_{EP} is the time spent with electrode positive polarity. The magnitude of the welding currents in EP and EN is also adjustable. The EN polarity fraction is denoted by β, and is defined as:

$$\beta = \frac{|I_{EN}|}{|I_{EN}| + |I_{EP}|} \tag{2.2}$$

where I is the welding current and the subscripts have the same meaning as in Equation 2.1. By adjusting θ and β, the degree of welding penetration and cathodic cleaning action can be controlled. These parameters were originally investigated by Okada *et al.* [50] in the early 1980s.

1.7 Research Objective and Thesis Organization

The DSAW process has been shown to be a feasible and practical method for producing high quality, conduction-mode, butt-joint configuration welds in thin aluminum sheet. Magnesium alloys present similar welding challenges, having thermo-physical and oxide properties that are similar to those of aluminum. There are several potential advantages in the DSAW process that could be useful in the welding of magnesium alloy sheet. Advantages, such as a well-controlled heat source; cathodic cleaning; shielding on both sides; symmetrical weld profile; minimum angular distortion, could all be of value, yet the DSAW process has not previously been applied to magnesium alloys. Therefore, the objective of this research was to explore the weldability of AZ31B-H24 magnesium alloy sheet in the butt-joint configuration using the DSAW process.

Process parameter ranges were identified that produce acceptable welds and optimal welding parameters were found. The resulting welds were examined and characterized using standard metallurgical laboratory techniques. The mechanical properties of the welds were determined by hardness testing, transverse tensile testing and longitudinal tensile testing of the weld fusion zone metal, distinct from the surrounding base metal.

In the following Chapter 2, a review of the current state of knowledge in the field of welding magnesium alloys is presented. Chapter 3 describes the experimental work carried out as part of this research. Details of the welding equipment, materials and procedures are given. The activities involved in the analysis of the welded joints are described. Chapter 4 includes all of the experimental results reported in this work. The results are discussed in the context of the existing published work in the field. Finally, a summary of the work and the conclusions that can be made are presented in Chapter 5.

Chapter 2

Literature Review

2.1 Welding Processes for Magnesium Alloys

Magnesium alloys are described as being “readily welded” in the Welding Handbook of the American Welding Society [51]. Specifically, AZ31B magnesium alloy is described as having “excellent” weldability by both Resistance Spot Welding (RSW) and Gas Tungsten Arc Welding (GTAW). Other possible processes that might be used to weld this alloy include electron beam welding, laser beam welding and stud welding.

This chapter summarizes the present state of research into welding methods that are suitable for joining AZ31B magnesium alloy, particularly with a view to efficient mass production. The surveyed literature describes the welding of AZ31B magnesium alloys as being generally prone to: 1) solidification shrinkage cracking, 2) porosity defects and 3) weld contamination due to the extreme reactivity of magnesium at high temperatures. All of the research described in the literature has focused on identifying ways to overcome the problems in these 3 areas.

2.1.1 Resistance Spot Welding (RSW)

Resistance Spot Welding (RSW) of lap joints is by far the most common method of assembling the sheet metal components of manufactured products, including automobile bodies. Figure 2.1 shows a schematic representation of the process. It involves applying force to and electrical current through overlapping sheets of metal via 2 water-cooled copper electrodes. The resulting resistive heating melts the sheet metal at the sheet interface to form a fusion zone or weld “nugget”. RSW is the mainstay of the automobile assembly industry and is widely applied to welding of sheet steel in the lap-joint configuration. RSW is extremely efficient, when applied to steel, in so far as it is very fast, uses simple and fairly low-cost equipment, and is tolerant of considerable variance in welding parameters and part fit-up quality [52].

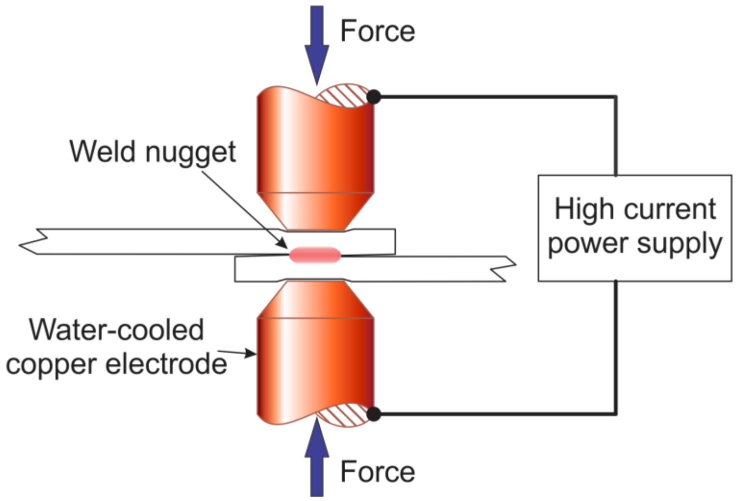

Figure 2.1: Schematic representation of the Resistance Spot Welding (RSW) process.

The RSW process can also be applied to aluminum; however, in that case, the process becomes somewhat less attractive, due to material properties that are less conducive to the RSW process. Much higher electrical currents are required in aluminum, to achieve the same heating effect as in steel, due to aluminum's low resistivity. Thus, bigger and more expensive power supplies are required to resistance spot weld aluminum alloy sheet. There is also much greater erosion and wear of the electrode tips, which adds to the overall process cost. Nonetheless, RSW is still the process of choice for assembling over-lapping sheet aluminum components, as used by the auto industry [53].

There is much less published research available on RSW of magnesium alloys, reflecting the small amount of magnesium sheet metal used by industry. Recent interest in magnesium for automotive structures has started to change this situation and the number of published works is increasing. Magnesium alloys can be joined by RSW as long as the parameters are carefully set to account for the electrical resistivity, thermal diffusivity and yield stress of the metal [54].

In 2012, Babu *et al.* [55] reported that the RSW heat input parameters were quite sensitive when welding magnesium alloys and that expulsion of liquid metal would occur at higher than optimal heat input, thus compromising the mechanical strength of the joint. They also noted that inclusions of contaminants in the weld could be a problem and that shrinkage of the fusion zone on solidification could result in a collapsed zone at the center of the nugget, thereby weakening the joint.

Xiao *et al.* [23] described the solidification processes within the weld nugget of RSW welded magnesium alloys in detail. They recognized the role of very small intermetallic particles of Mn_5Al_8 as nucleation sites to promote a fine grain structure within the weld nugget and went on to experiment with inoculation of the weld site with pure titanium powder to enhance this grain refining effect [56]. The optimal size of the inoculating particles was established and an improvement in the microstructure of the resulting welds was reported.

It should be noted that RSW is applicable to the lap-joint configuration only. Therefore, although RSW will certainly find application in some areas of sheet metal assembly, it is not a candidate to produce butt-joint configuration welds, as would be required in the production of tailor-welded blanks.

2.1.2 Friction Stir Welding (FSW)

Friction Stir Welding (FSW) is a solid-state welding process in which a rotating tool is used to apply frictionally generated heat and plastically deform the metal to form an autogenous weld joint. Figure 2.2 shows the process schematically in the butt-joint configuration. A wide variety of tool geometries have been tried [57] but most tools consist of a pin with a helical profile on the outside that plastically stirs the metal. The tool has a shoulder which is kept at the height of the material surface and leaves a flat processed weld surface behind the slowly advancing tool. The lap-joint configuration is also possible, by making the pin long enough to protrude into both layers of the material. The FSW process results in a processed zone of highly deformed material with a very fine grain structure. Normally, the heat generated is sufficient to soften the metal but not melt it. The process has certain advantages over fusion processes, in that the metallurgical defects normally associated with solidification are avoided [57]. This is a particularly attractive feature of the process, when applied to magnesium, compared to conventional fusion welding processes [54].

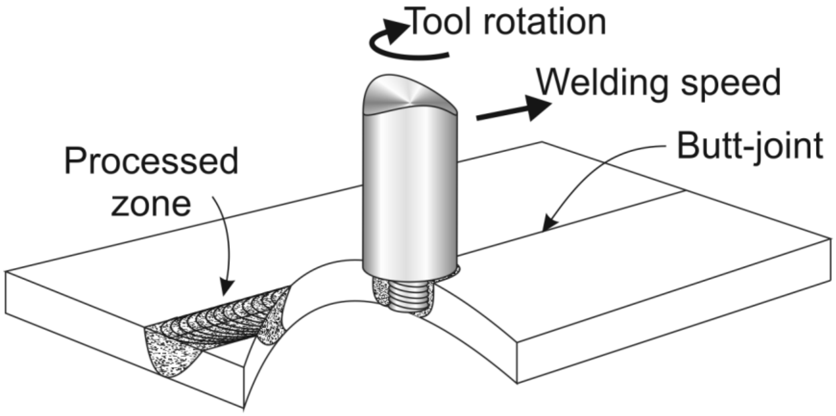

Figure 2.2: Schematic representation of the Friction Stir Welding (FSW) process.

In recent work by Afrin *et al.* [58], the strength of friction stir welded magnesium alloys was examined. The resulting very fine grain structure of the mechanically processed zone suggests that the process could produce a very strong joint. They found that although the mechanically processed zone had a higher hardness than the base metal, there was significant softening of material in the heat affected zone (HAZ). Consequently, upon tensile testing, all of the joints failed in the HAZ.

Kostka *et al.* [59] used the FSW process to make dissimilar butt-joint welds between sheets of magnesium AZ31B and aluminum AA6040. They found that the relatively low temperatures attained during FSW reduced the tendency to form intermetallic compounds that are usually associated with welding magnesium to aluminum. As such, the process has advantages when applied to Al-Mg dissimilar joints.

Commin *et al.* [60] looked more closely at FSW of the AZ31B magnesium alloy, with a view to using the process to join large magnesium panels in aerospace applications. The strain and temperature fields on both the advancing and retreating side of the rotating FSW tool were investigated. They also established a process parameter window and concluded that optimal microstructure resulted when the processed zone reached a temperature 670 K (400 °C). The authors calculated that FSW welds in AZ31B magnesium alloy may suffer from considerable residual stress in the surrounding material, especially on the retreating side of the tool. No details of grain growth in the HAZ were reported and the mechanical properties were established by micro-hardness measurement only. The highest welding speed reported was 30 mm/s.

All of the researchers above have recognized that the FSW process is limited by a slow welding speed and the high mechanical forces that have to be resisted by robust welding fixtures [58] [59] [60] [61]. Hence, magnesium alloys, which are relatively soft and in any case require slow welding speeds, make good candidates to be welded by this process. It may be noted that the reported problems of grain growth in the HAZ and residual stress in the surrounding metal are essentially the same as those experienced in fusion welding processes.

Friction stir welding (FSW) is a promising solid-state welding process that can be applied to lap-joint or butt-joint configurations without the attendant metallurgical problems of solidification in the weld zone. However, it is presently limited to high value, specialty items, due to slow welding speeds and the requirement for special fixtures to withstand the considerable contact forces involved [60].

2.1.3 Gas Metal Arc welding (GMAW)

Gas metal arc welding (GMAW) is not normally used with magnesium alloys and most authorities, including the American Welding Society, state that magnesium cannot be welded using the conventional GMAW process [51]. The main difficulty stems from the low boiling point of magnesium, which causes the filler wire to vaporize explosively as it is fed into the arc plasma. This prevents transfer of liquid metal to the weld pool in a stable stream of small droplets. The result is extreme spatter and inconsistent metal deposition [62]. Nonetheless, the GMAW process is attractive to industry for several reasons and has been widely applied to the welding of steel and aluminum alloys. It offers the advantages of high deposition rates, energy efficiency, tolerance of moderate gaps and the ability to introduce desirable alloying elements into the weld metal, via the filler wire. The GMAW process is also readily automated [63].

The problem of adapting the GMAW process for use with magnesium alloys has been studied principally by Rethmeier *et al.* [64], Song *et al.* [62] and Gao *et al.* [65]; the latter investigating a laser-GMAW hybrid system. These researchers all note the requirement to precisely control the heat input, such that the filler wire melts without boiling. The approach has been to use a multi-level, pulse-modulated waveform to control the electrical power input. These experimental power supplies produce pulsed waveforms consisting of a very short, high current pulse, sufficient to melt a section of wire, followed by a longer pulse of much lower current. The low current pulse facilitates metal transfer with minimal heat input, and avoids boiling the filler wire [66]. It has only recently become feasible to produce these complex waveforms, with new developments in power electronic switching devices, such as the Insulated Gate Bipolar Transistor [49]. Such sophisticated waveform control is likely to become available in commercial welding power supplies in the near future.

Gas metal arc welding (GMAW), favoured by industry for its high productivity when applied to steel, is not yet properly adapted for use with magnesium alloys. Research focuses on pulsed waveforms that can control the heat input to avoid boiling of the filler wire [62]. Associated research is also required to allow economical production of filler wire materials for magnesium alloys [29].

2.1.4 Gas Tungsten Arc Welding (GTAW)

The Gas Tungsten Arc Welding (GTAW) process has long been considered the natural choice for welding reactive metals such as Al, Mg and Ti due to its characteristic ability to provide good shielding of the weld from contamination [34]. Square-wave AC welding current is always used in these cases, in order to take advantage of the cathodic cleaning action, described in Chapter 1. The process has, therefore, been extensively researched by those interested in welding magnesium alloys [67] [68]. Often, the research involves comparing welds made using GTAW to those made by other welding processes [61].

Figure 2.3 shows a representation of the GTAW process, including the resulting full penetration, butt-joint weld made in AZ31B magnesium alloy sheet, as reported in the surveyed literature. An electric arc (a), often bell-shaped, is maintained between a non-consumable tungsten electrode (b) and the work. Inert shielding gas (c) is fed through a surrounding nozzle (d) to blanket the molten weld pool and the surrounding hot base metal with a protective atmosphere. The resulting weld will usually have a smooth top surface as shown at (e). This surface is likely to be slightly under-filled because of magnesium loss to evaporation and the small amount of drop-through shown at (f). The fusion zone (g) is likely to approximate a semi-circle, typically twice as wide as it is deep, depending on the patterns of fluid flow within the molten weld pool [69]. A heat affected zone (HAZ) (h) will extend to some distance into the base metal, on either side of the fusion zone, where the heating and cooling that takes place during the welding process has altered the base metal microstructure and properties.

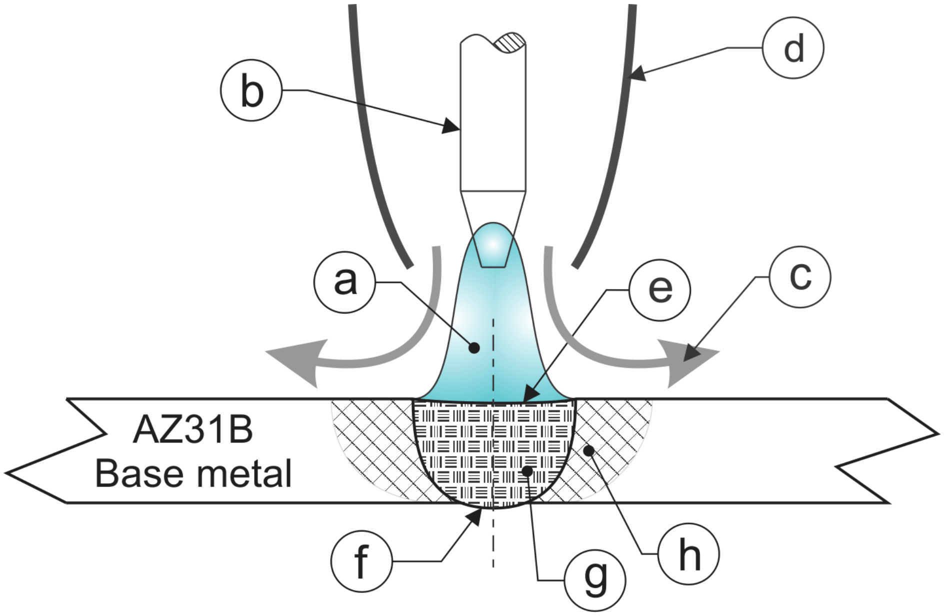

Figure 2.3: Cross-section through an ideal full-penetration GTAW butt-joint weld, made in AZ31B magnesium alloy.

In 2002, Sun *et al.* [70] compared welds made in AZ31B magnesium alloy using GTAW, with others made using laser heat sources. With both welding processes, the importance of surface preparation and proper shielding of the hot metal during welding were noted. The authors described the now well established differences in the microstructure of welds made with low (GTAW) and high (laser) energy density heat sources. They noted that GTAW welds were characteristically shallow with respect to width, had a significant HAZ adjacent to the weld and a course grained, dendritic fusion zone. Conversely, laser welds could be made deep and narrow, had a very small HAZ and a fine grained fusion zone.

In 2006, Liu *et al.* [67] experimented with cold-wire fed automated GTAW welds in AZ31B magnesium alloy. They compared the welds made with filler wire to those made autogenously and reported that weld penetration was deeper if filler wire was not used but did not elaborate further. The welds without filler failed in the HAZ, whereas those made with AZ61 filler wire failed in the fusion zone. The authors attributed this difference to larger fusion zone grain sizes in the joints with filler wire, due to the extra heat input (and associated lower cooling rate) required to melt the wire. They did not address the possibility that the AZ61 filler wire had raised the aluminum content of the AZ31 base metal in the fusion zone and that this had caused more brittle β-phase $Mg_{17}Al_{12}$ material to be formed at the grain boundaries.

In 2010, Padmanaban *et al.* [61] compared the mechanical properties of welded joints of AZ31B magnesium alloy made by GTAW, FSW and laser processes. They reported joint efficiencies of 85% for GTAW joints and 98% and 99% for FSW and laser joints, respectively. They did not specify the temper condition of the base metal, but their stress-strain curve for the base metal (UTS: 190 MPa) suggests it was fully annealed. The GTAW welds all failed in the HAZ and they state that this was due to the considerable grain growth that occurred. Grain sizes were not quantified, but their micrographs show grains of around 40 μm in size.

In subsequent work, Padmanaban *et al.* [71] reported on the fatigue behaviour of these same welded joints. They found that the GTAW joints were somewhat less resistant to fatigue than either FSW or LBW welded joints. Specifically, they reported a 12 % higher fatigue exponent in the Paris power law [72] for GTAW welds than for laser welds. They attributed this difference in fatigue performance to differences in grain size in the fusion zones of the welds. The GTAW welds had larger FZ grains than the welds made with the other two processes. This is a reasonable suggestion but the authors did not quantify the difference in fusion zone grain sizes between the processes.

Gas tungsten arc welding (GTAW), used with a variable polarity square wave-form, continues to be a suitable process for welding magnesium alloys in maintenance and repair operations. However, low power and low welding speeds are required in order to avoid the typical problems of hot cracking and porosity. The process is, therefore, not very attractive for high volume manufacturing applications.

2.1.5 Laser Beam Welding (LBW)

The use of lasers as a heat source for welding magnesium has been studied extensively [13] [31] [73] [74] [75]. A 2006 review by Cao *et al.* [13] provides a thorough overview of the main issues, including a description of the key-hole mode of welding, in which a deep pocket of metal vapour is formed and maintained in the weld pool. The traditional low energy density arc welding power sources, when applied to wrought magnesium alloys, all result in the formation of a significant HAZ and a fusion zone microstructure with larger grains than the base metal. These effects naturally lead to lower mechanical properties in the welded joint. However, the use of a high energy density heat source, such as a laser beam, has the potential to leave practically no HAZ and a smaller fusion zone grain size than that of the base metal [13]. On these grounds, laser welding offers the possibility of welds with mechanical properties superior to those of the surrounding base metal. Unfortunately, other aspects of this high speed, high energy-density process are more detrimental to the resulting welded magnesium alloy joint.

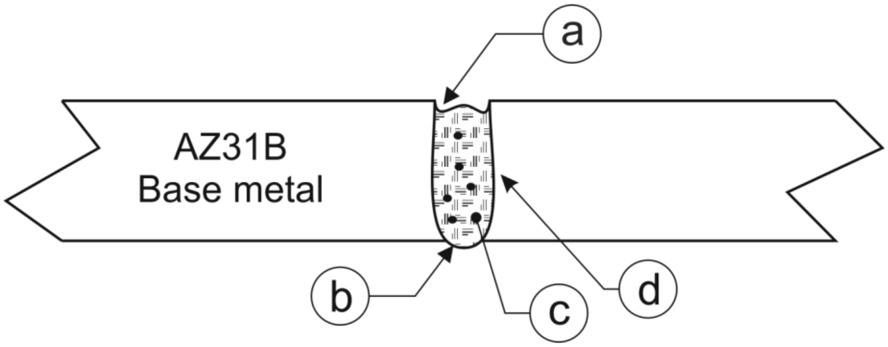

Figure 2.4: Typical keyhole-mode laser butt-joint weld made in AZ31B.

Figure 2.4 shows a cross-section of a typical keyhole-mode laser butt-joint weld, made in AZ31B magnesium alloy, as reported in the surveyed literature. The undercut top surface (a) is much more pronounced in a laser weld, compared to a typical GTAW weld due to vaporization of the magnesium. A small amount of drop-through (b) is to be expected in a full-penetration weld. Hydrogen porosity and occluded vapour porosity (c) has been reported as a problem by many researchers investigating laser welding of magnesium alloys [31]. It appears that the deep, narrow weld profile, coupled with the high welding speed, prevents the gas bubbles from escaping the weld pool before it solidifies [74]. The HAZ is typically very narrow (d) or even indiscernible, at a macro-scale.

In 2008, Coehlo *et al.* [73] gave a detailed report of their experiments in producing autogenous butt-joint welds in AZ31B magnesium alloy at speeds of up to 90 mm/s, using a 2.2 kW Nd:YAG laser beam. They achieved narrow, full-penetration welds, with minimal porosity and good cross-sectional profile. There was no significant undercut or drop-through. These welds had a very fine fusion zone grain structure and good mechanical properties. In transverse tensile testing, fracture always occurred in the base metal, indicating a high quality fusion zone. They also performed longitudinal tensile testing on miniature specimens extracted from the fusion zone. These tests confirmed the superior mechanical properties of the fusion zone metal. Maximum elongation was 20% compared to 24 % for the annealed AZ31B base metal.

In 2010, Kim *et al.* [74] reported on the use of a Nd:YAG laser to make autogenous welds in sheet AZ31B magnesium alloy in the butt-joint configuration. After experiencing initial difficulties obtaining adequate shielding conditions, they achieved visually acceptable welds at welding speeds between 50 mm/s and 100 mm/s using a beam power of around 1.5 kW. Joint efficiencies were reported to be up to 100 % of base metal properties and porosity was negligible. The microstructure in the fusion zone was not reported, but macrographs of the weld profile showed a characteristic narrow, full-penetration weld with good surface appearance.

Laser welding using a Nd:YAG laser beam directed through a fiber-optic cable offers the possibility of welding magnesium in the keyhole-mode, due to a very high energy density. Increased welding speeds are possible as a result [13]; however, other defects remain, such as excessive vaporization and poor weld bead quality. Geometrically poor weld profiles with undercut and drop-through have been reported when laser welding magnesium alloys [46]. Gas porosity is generally a bigger problem when laser welding, because the gas bubbles have less opportunity to escape the weld pool [74].

The use of a high energy density laser heat source offers the advantage of higher welding speeds than those achievable with arc-based heat sources. Other desirable weld features may include a finer fusion zone microstructure and a smaller HAZ. However, the susceptibility of magnesium welds to hydrogen porosity is worse, under these conditions. Laser welds are prone to undercut and drop-through defects that inevitably occur in mass production. Finally, the high capital cost of laser welding equipment must be considered as a disadvantage to the process.

2.1.6 Hybrid Laser-Arc Welding

Hybrid laser-arc welding refers to the simultaneous use of both laser and arc heat on the same weld pool surface in order to take advantage of the desirable characteristics of both heat sources. It has been reviewed in 1999 by Tusek and Suban [76], 2005 by Bagger and Olsen [77] and in 2009 by Ribic *et al.*

[78]. The advantage of the hybrid heat source lies in the synergy between the laser beam and the arc plasma that results in weld characteristics superior to those obtained from either heat source separately [79]. The resulting weld profile is a combination of the characteristic profiles of laser and arc welds and is shown in Figure 2.5.

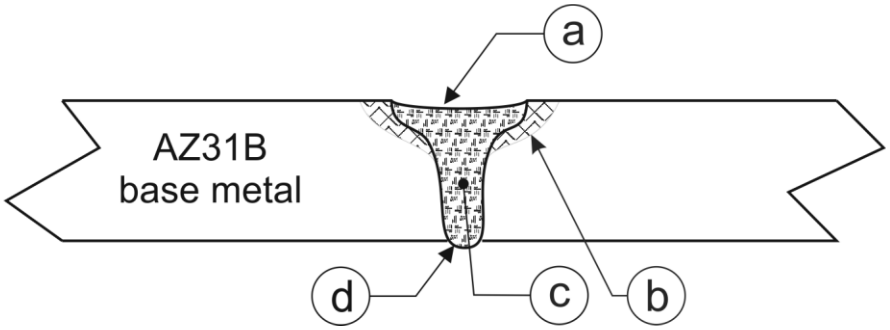

Figure 2.5: Cross-section through a typical laser-GTAW hybrid butt-joint weld in AZ31B magnesium alloy sheet.

In the upper part of the weld, the arc heat flux dominates and a wide, shallow weld pool forms, with a characteristic smooth surface at (a). A small HAZ forms in the top portion of the sheet as a result of heat conduction into the surrounding base metal at (b). In the lower part of the weld, the laser heat dominates, and the fusion zone is narrow (c), without any significant HAZ. The lower surface of the weld is much the same as the laser weld, with some drop-through (d).

The action of the laser beam passing through the arc plasma has a further effect of anchoring the arc to a single spot, rather than it being in constant movement over a given area. This arc stabilizing effect has been investigated and reported by Chen and Liu [80], Mahrle and Beyer [81] and others. Chen and Liu [80] have also proposed a physical mechanism for the stabilizing effect. This effect is important, because it is a method of constraining the arc heat source to a smaller area than it would otherwise occupy. The arc is therefore of a higher energy density. Also, by eliminating the tendency for the arc to wander, spattering is greatly reduced. Hybrid laser-arc welds are somewhat more tolerant of gaps between the parts than a similar laser weld [78]. The augmentation of a welding arc with a laser beam may not require a very powerful laser beam to be effective. Liu *et al.* [32] used a 300 W Nd:YAG laser to augment a 100 Amp GTAW arc and reported all of the above beneficial results.

Obviously, a hybrid laser-arc welding system is a complex piece of equipment with many additional parameters to be adjusted. It is also expensive to acquire and maintain, due to the high cost of lasers. Such systems are likely to be attractive to industry, only if the capital cost of laser equipment continues to decline.

Hybrid laser-arc welding has been shown to offer the beneficial characteristics of both laser and arc heat sources. The synergy is based on the attraction of the arc to the laser spot [80]. The laser constricts and confines the electric arc to one location and effectively increases the energy density of the arc. The electric arc, meanwhile, imparts a smooth top surface to the weld bead and allows the escape of hydrogen bubbles more easily. It is possible that some form of laser-augmented electric arc welding will eventually emerge as the favoured technology for welding magnesium, if the cost of laser power supplies continues to fall.

2.1.7 Double-sided arc welding (DSAW)

The double-sided arc welding (DSAW) process was introduced earlier, in Section 1.4 and shown schematically in Figure 1.2. The configuration can be used with either 2 GTAW torches, 2 PAW torches or one of each. Whichever type of torch is selected, the process has the advantage of adding heat to the weld simultaneously from both sides of the sheet.

The DSAW process was successfully applied by its inventors, Zhang and Zhang [33], for key-hole mode welding of steel and aluminum plates in the vertical-up position and showed that welds with greater depth-to-width ratio could be produced by the double-sided configuration than possible by the conventional single-sided arc welding processes [35]. They also demonstrated a smaller heat affected zone, finer microstructure and absence of angular distortion in welds made in 6 mm to 12 mm thick 6061 aluminum alloy plates [82]. The finer microstructure was attributed to a faster cooling rate in the relatively narrow, full-penetration, double-sided welds. They also suggested that the current flow, directly through the thickness direction of the plate, brings other benefits in terms of induced fluid flow in the weld pool [83].

The DSAW configuration has been subsequently investigated at the University of Waterloo by Kwon [36] [39] [40], Moulton [37] [41] and Joshi [38] in the horizontal position, to produce full penetration, conduction-mode welds in thin AA5182 aluminum alloy sheet. Kwon [36] [40] made butt-joint configuration welds in 1.2 mm thick sheet at speeds of up to 60 mm/s with satisfactory results. She determined that optimal cathodic cleaning was achieved when the waveform parameters of θ and β were both set to 50 %. This is to be expected, since each side of the sheet would presumably need the same degree of cathodic cleaning and heat input. At very low welding speeds, the weld pool was wider than the arc column and was therefore not completely cleaned by the action of the arc. Mechanical properties of the welds were good; with joint efficiencies over 90 % and no deterioration in mechanical properties with increasing welding speed. Kwon and Weckman [39] also developed an analytical thermal model of the DSAW process that could predict the weld bead geometry, based on the welding parameters.

Moulton [37] [41] examined the butt-joining of dissimilar thicknesses of AA5182 aluminum alloy sheet, as would be typical in the production of tailor welded blanks. He showed that it was possible to obtain a smooth transition between the thicker and thinner sheet by careful alignment of the torch centerlines towards the thicker sheet. Acceptable DSAW welds were made using welding speeds up to 100 mm/s; however, the mechanical properties of the welds were found to decrease as welding speed increased above 40 mm/s. The best mechanical properties were found in welds made at 25 mm/s. The deterioration in mechanical properties, particularly elongation, was found to be caused by the onset of solidification shrinkage micro-porosity at the higher welding speeds. This micro-porosity was unavoidable, due to the characteristically long weld pool tail associated with high speed welds and the low thermal gradient that exists at the interface. Thus, a wider mushy zone with consequent choking-off of the fluid flow at the dendrite roots during solidification occurs under these conditions, resulting in micro-porosity [25]. The ductility and formability of the welded sheet were found to be best when the DSAW welds were made at low welding speeds. This was attributed to an absence of micro-porosity at such low welding speeds.

Joshi [38] examined the use of the double-sided arc welding system to make seam and spot welds in the same AA5182 aluminum alloy sheet in the lap-joint configuration. He found that visually acceptable seam welds could be produced at speeds of up to 70 mm/s, but mechanical properties were poor. Tensile testing of low speed welds showed joint efficiencies of around 40 %. These reduced mechanical properties were found to be caused by oxide tails in the fusion zone. Joshi suspected that the inside faces of the over-lapped sheets, hidden from the cathodic cleaning action of the arc, were the source of the entrained oxides. He reported fewer oxide tails when rigorous pre-weld surface cleaning measures were taken. Spot welds made with the double-sided arc welding system were adequate, from the standpoint of shear strength, but not without defects. Crater cracks, micro-porosity and oxide inclusions were the common flaws seen. All of the spot-welds were found to have a full-penetration pin-hole in the center, due to piping from both sides of the weld, caused by solidification shrinkage during final solidification of the stationary spot welds.

2.2 Summary of Current State of Research

Current research into welding and joining of magnesium alloys aims to widen the presently available range of processes that can be used to join these alloys. Lowering the cost and improving the quality of the resulting joints is seen as essential to allowing increased use of magnesium alloys in manufactured products.

The well-established method of joining sheet material using resistance spot welding (RSW) has been shown to produce good results with magnesium alloys, as long as the parameters are carefully set. A new generation of equipment that incorporates variable current and force control should allow the process to be successfully used to join magnesium alloys in the lap-joint configuration. However, seam welds, in the butt-joint configuration require a different technology.

The traditional, low energy density arc-welding processes have all been explored for use with AZ31B magnesium alloy, as well as the solid-state FSW process. The GTAW process, using square-wave AC, has been shown to be the most satisfactory of the traditional fusion welding techniques. All processes are sensitive to parameter settings and require the use of low welding speeds, in order to produce reasonable quality welds.

High energy density welding heat sources, such as lasers, have naturally been the subject of research in order to achieve higher welding speeds. However, lasers are expensive and do not provide the beneficial cathodic cleaning action of an electric arc. This is particularly useful when welding reactive metals, such as magnesium. While lasers have been shown to achieve higher welding speeds than electric-arc processes, they also have disadvantages, when applied to AZ31B magnesium alloy, in terms of weld bead geometry and susceptibility to porosity defects. Some of these disadvantages can be overcome by the use of hybrid laser-arc heat sources but these systems add complexity and cost.

Plasma arc welding (PAW) may offer a compromise technology of a fairly high energy density, without the cost and complexity of a laser-augmented heat source. PAW has its own set of additional parameters and maintenance requirements but retains the benefit of cathodic cleaning, whereas a laser heat source does not. The plasma-arc heat source has been successfully used in the double-sided configuration, at the University of Waterloo and elsewhere, to investigate the benefits of simultaneously welding from both sides of the sheet metal. The benefits of DSAW have been demonstrated, when applied to keyhole-mode welding of steel and aluminum plate and particularly when applied to conduction-mode welding of aluminum alloy sheet. However, DSAW has never before been applied to magnesium alloy sheet, in the butt-joint configuration.

In the following Chapter 3, a series of welding experiments are described, in which a DSAW system, using 2 plasma torches, is used to make full-penetration, autogenous, conduction-mode welds in AZ31B magnesium alloy sheet, in the butt-joint configuration.

Chapter 3

Experimental Apparatus and Procedures

3.1 Double-Sided Arc Welding System

A double-sided arc welding system was used for these experiments, comprising the following main components: (1) a power supply, (2) two identical vertically opposed plasma arc welding torches, (3) two plasma consoles, (4) a cooling system, (5) a traversing welding fixture, (6) a welding speed control system and (7) a data acquisition system. The system is shown schematically in Figure 3.1.

The system is the latest configuration of many of the same components that have been used by previous researchers at the University of Waterloo. The power supply, the traversing welding fixture and the data acquisition and control system are the same as used by Kwon and Weckman in 2003 [36] [39] [40], Moulton and Weckman in 2008 [37] [41] and Joshi and Weckman in 2010 [38]. The system has proved reliable in accurately recording welding parameters in experiments conducted by these researchers.

3.1.1 The Power Supply

A standard Miller®™ Aerowave®™ brand 300 Amp, constant current, square-wave AC welding power supply was used for these experiments. It provided independent control of: welding current, square-wave frequency, square-wave balance between Electrode Positive and Electrode Negative mode (θ) and proportion of time in each of Electrode Positive and Negative mode (β). For the purposes of this research, θ and β were both set to 50 %, as was done by Kwon [36] [39] [40], Moulton [37] [41] and Joshi [38] in their previous work.

3.1.2 Double-Sided Arc Welding Torches

Two identical plasma arc torches, designed and manufactured by B&B Precision Machine, Inc. of Owens Cross Roads, Alabama, USA, were arranged in vertical alignment, above and below the workpieces. This patented design of plasma arc torch has been found to be durable and allows easy maintenance of the tungsten electrode and the orifice without disturbing the coolant circuit inside the torch. Provision was made for precise vertical position adjustment to allow various stand-off distances to be used.

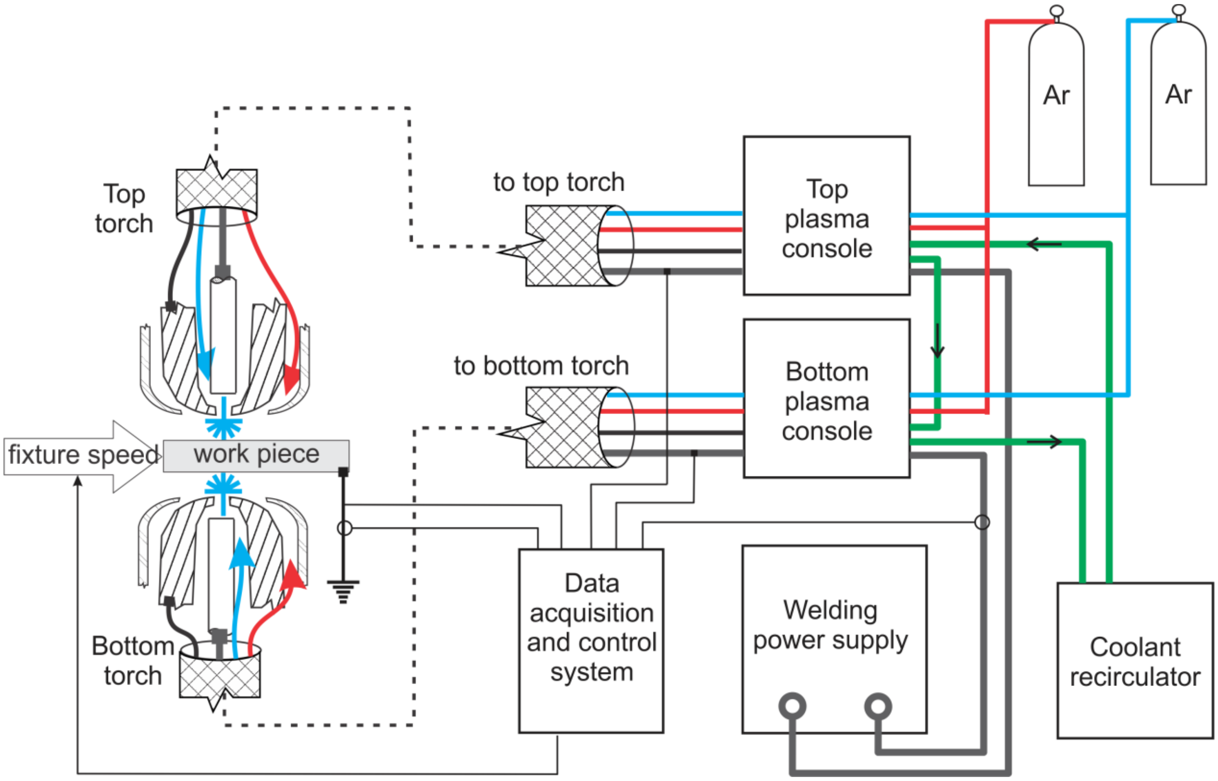

Figure 3.1: Schematic representation of the double-sided arc welding system used in these experiments.

A pair of custom made trailing shielding gas diffusers were manufactured and attached to both torches, positioned just clear of the workpiece surface, behind the weld pool. The diffusers consisted of machined aluminum blocks with porous nickel screens that blanketed the weld surfaces with argon, behind the hot weld pool. Argon shielding gas was fed separately to each device, via flow meters on the front of the plasma consoles. Figure 3.2 shows two views of one of the plasma torches, fitted with the trailing shield attachment.

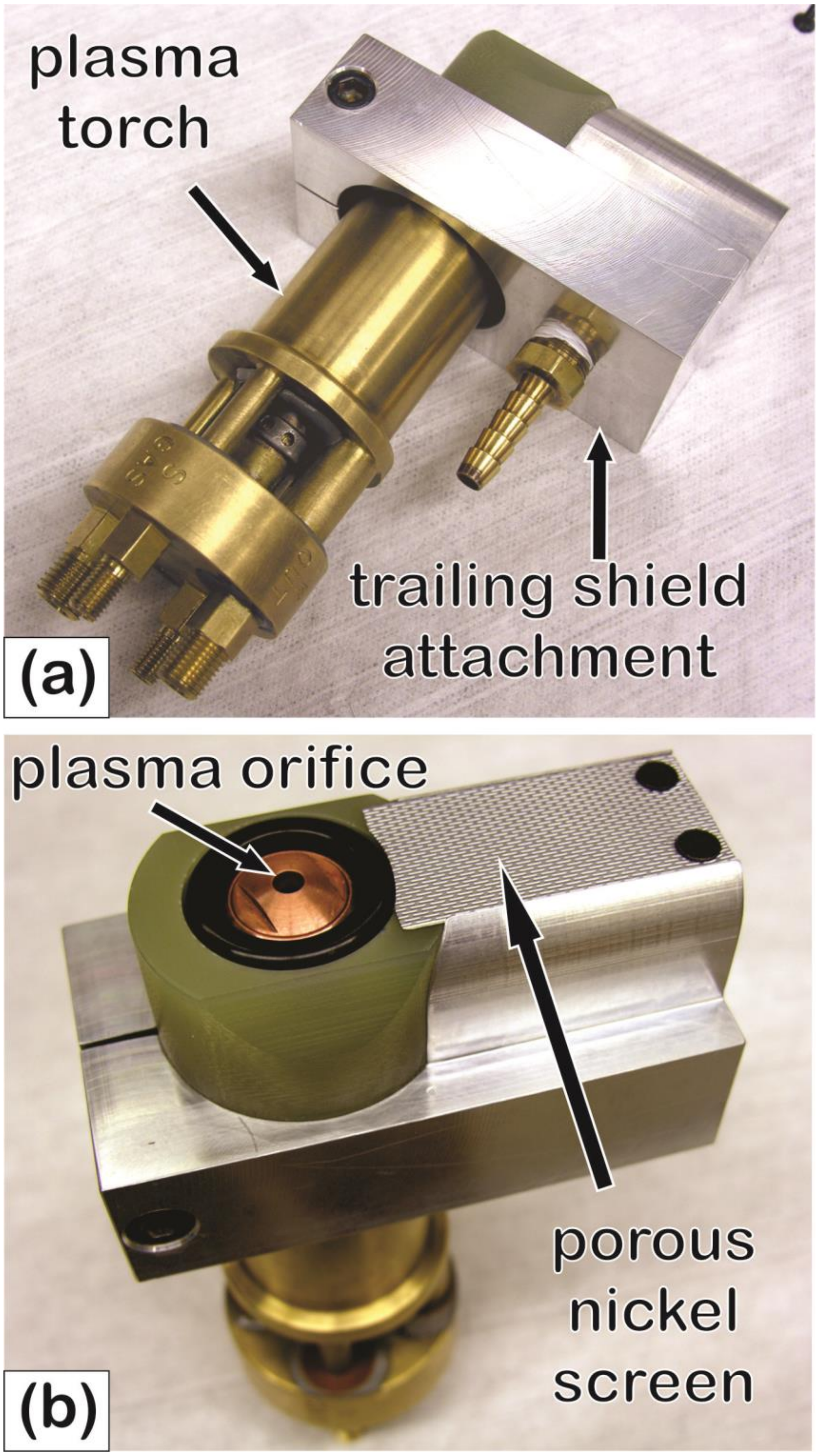

Figure 3.2: Photographs of one of the plasma arc torches fitted with the trailing shield device, showing: a) the torch body and trailing shield attachment and b) the plasma orifice of the PAW torch and the porous nickel screen of the trailing shielding gas distributer.

3.1.3 Plasma Consoles

Two identical Thermal Dynamics®™ model WC100B plasma consoles were used in the DSAW system. They control plasma and shielding gas flow, initiate and maintain the pilot arcs in the torches and monitor coolant and plasma gas pressures to each torch. The plasma consoles have relays that allow torch operation only if both coolant and plasma gas pressure is detected.

Ultra-high purity argon (99.998%) was selected as a plasma gas. It was fed from a cylinder via a regulator to both consoles at 275 kPa (40 psi), where flow to the torches could be controlled and monitored via separate flow meters. It is represented by blue lines in Figure 3.1. Industrial purity argon (99.8%) was chosen for the less critical shielding gas. It was fed from a cylinder to both plasma consoles at 275 kPa (40 psi) and supplied the primary torch shielding gas and the separate trailing shield attachment for top and bottom torches. Shielding gas was controlled and monitored via four separate flow meters, mounted on the front panels of the plasma consoles. Shielding gas is represented in Figure 3.1 by red lines.

The other function of the plasma consoles is to control arc starting by means of a pilot arc. A high voltage, high frequency AC circuit initiates an arc inside the torch, between the central electrode and the torch body. Once the pilot arc is established, it can be transferred to the workpiece by activating the main power supply circuit. The flow of ionized argon gas through the torch orifice provides a conducting path to the workpiece on both sides of the sheet. The pilot arc circuitry can operate in 2 modes, “normal”, and “continuous”. In the normal mode, the pilot arc shuts down once the main arc is established. In the continuous mode, a pilot arc current of 12 Amps is maintained between the central electrode and the torch body throughout the welding process. Normal mode is suitable for use with DC but results in a less stable arc when using square wave AC. In all of these experiments, the pilot arc was used in continuous mode.

3.1.4 Cooling System

Cooling of the plasma-arc torches was achieved with a Thermal Dynamics®™ model HE 100A, recirculating water cooler. The cooling circuit, shown schematically in Figure 3.1, passes cool, de-ionized water through both torches sequentially, before returning it to the reservoir. Care must be taken to maintain the de-ionized water to a high purity, with an electrical resistivity exceeding 1 MΩ/mm, by frequent flushing of the circuit with fresh de-ionized water. This prevents electrical short-circuiting, through the cooling water, of the arc circuits. The electrical power cables connecting the torches to the plasma consoles consist of bare copper conductors, loosely fitting within the coolant hoses. This design has the advantage of directly cooling the power cables as well as the torches. Of course, there is the requirement to maintain the cooling water sufficiently pure that it does not conduct significant electric current.

3.1.5 Double-Sided Arc Welding Traversing Fixture

A sturdy frame, with clamps, mounted on linear bearings and moved with a ball-screw mechanism, was used to traverse the work-pieces between the welding torches. Figure 3.3 shows the traversing fixture with the plasma arc torches in position, top and bottom.

3.1.6 Welding Speed Control System

The traversing fixture was driven by an electric servo-motor, through a speed reduction gearbox and the ball-screw mechanism. The servo controller is fed a set-point voltage signal between -10 V and +10 V from a National Instruments®™ LabView®™ version 6.0 based control system, installed on the control computer. The software calls for a fixture speed of between 0 and 200 mm/s by outputting a corresponding set point voltage between -10 V and +10 V. The accuracy of the speed controller was measured to be within ±5%, in the speed range used in this study.

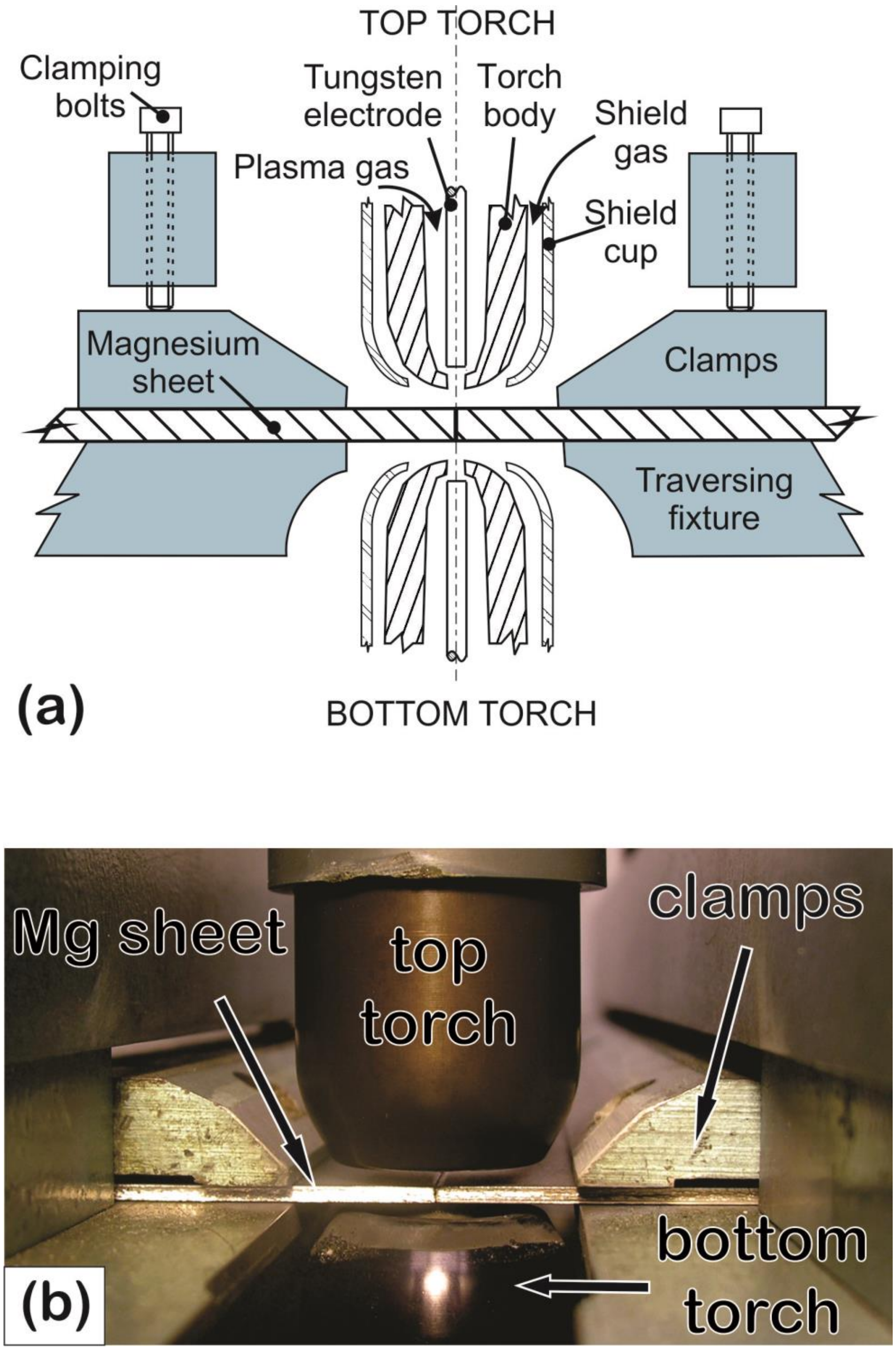

Figure 3.3: The traversing welding fixture with magnesium specimens clamped in place and plasma torches in position; (a) shown schematically with cross-section through torches and (b) photographed from one end of the fixture (trailing shield attachments have been removed for clarity).

3.1.7 Data Acquisition System

The data acquisition system provided accurate recording of welding current and voltages, as well as any stray current that may have passed through the grounded workpiece during welding. Welding current was measured by passing the main power cable through an LEM®™ model LT505-S Hall-effect current transducer. It is capable of measuring current over a range from zero to 500A to an accuracy of ±0.1A, up to a frequency of 150 kHz. Both torch-to-torch and top-torch-to-workpiece voltages were measured using 2 LEM®™ model LV100 Hall-effect voltage transducers. Stray ground current (which should be close to zero) was measured using another LEM model LT505-S Hall-effect current transducer, by passing the ground lead from the welding fixture through it. All 5 transducer signals were fed to the LabView®™ software, via a National Instruments®™ model PCI 6024E interface card. The data was recorded to a spreadsheet file, for subsequent analysis.

The software allowed control of the data sampling rate and of the time period over which the data was sampled. These settings were adjusted to accommodate the different speeds and weld lengths involved in the tests. Care was taken to sample data only from steady-state welding conditions, well away from the beginning and ends of the welds.

3.2 Materials

In these experiments, commercial purity AZ31B-H24 (warm rolled and partially annealed) magnesium alloy sheet of 2 mm thickness was used. The material was manufactured by Magnesium Elektron®™ and is identified as coming from heat number 10440, coil number 9577. Its composition was compared to the nominal composition using a Thermon Scientific brand XRF analyzer. The results are shown below in Table 3.1. They confirm that the composition of the material is well within the specified nominal range. Aluminum, zinc and manganese are the alloying elements, while the remainder are impurity elements whose presence must be tightly controlled in order to avoid undesirable effects, especially in corrosive environments.

Table 3.1: Nominal ASM **[2]** and measured compositions of the AZ31B-H24 magnesium alloy.

Composition (wt%)	Al	Zn	Mn	Si	Cu	Ni	Fe	Mg
Nominal	2.5 - 3.5	0.7 - 1.3	0.2 - 0.5	<0.30	<0.05	<0.005	<0.005	Balance
Measured	3.02	0.80	0.30	0.01	undetected	undetected	undetected	Balance

3.2.1 Welding Specimens

Each weld consisted of a butt-joint, made between the longer edges of two identical rectangular specimens, properly located and clamped in the traversing fixture. Three sizes of welding specimen were used in these experiments, depending on the required post-weld analysis. *Batch 1 welds*, intended for general metallurgical analysis and an exploration of the window of primary process parameters, were made with 170 mm x 50 mm sized specimens. *Batch 2 welds*, intended for transverse tensile testing, using the standard sized ASTM 12.5 mm (½ inch) flat tensile specimen, were made from 250 mm x 75 mm specimens. *Batch 3 welds,* intended for sub-sized specimens for longitudinal tensile testing of the weld metal, were made from 250 mm x 50 mm rectangles.

3.2.2 Pre-Weld Material Preparation

The specimens were first sheared to size, such that the weld would be made perpendicular to the rolling direction. One long edge was machined flat and square in a milling machine. Each specimen was then degreased and cleaned with acetone to remove surface contaminants, such as residue from: marking inks, rolling lubricants, oils and metalworking fluids.

A stainless steel wire wheel was then used to brush the material surfaces to a clean and bright finish in the area of the weld. Brushing was done perpendicular to the welding direction. Further cleaning was done using heptane, an oxygen free industrial solvent, to remove any dirt or oil left by the stainless steel wire wheel. The specimens were subsequently handled only with clean gloves and the weld made within an hour of wire brushing.

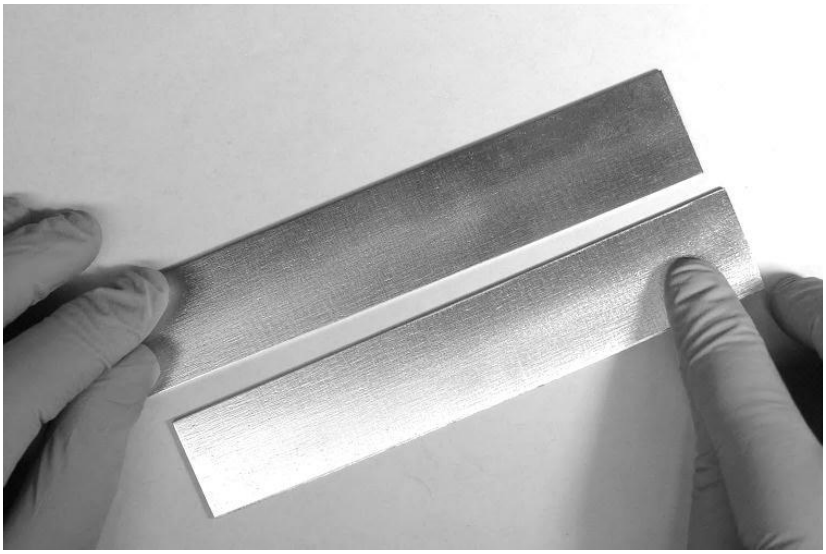

Figure 3.4: A Batch 1 specimen prior to welding.

3.3 Welding Procedures

The following procedure was followed for all welds made in these experiments.

1. Specimens were located in the traversing welding fixture, using a gage to align the faying edges along the centerline, with no gap between the specimens.
2. Specimens were clamped by evenly and progressively tightening the eight clamping screws to 40 N·m torque.
3. The traversing welding fixture was manually positioned to the correct starting position for the test.
4. Torch stand-off distances were set or confirmed, using a feeler gage.
5. The torch coolant recirculating system was turned on.
6. Plasma and shielding gases were turned on at the cylinders and pressure regulated to 275 kPa (40 psi) at the consoles.

7. The 2 plasma consoles, the main welding power supply, the control computer and the fixture speed controller were turned on.
8. Plasma gas, main shielding gas and trailing shield gas flow rates were confirmed for both top and bottom torches. The gases were allowed to flow for 1 minute to purge the hoses.
9. The welding fixture travel speed was set and welding parameters entered into the data logging software.
10. Welding current was set on the main power supply.
11. Top and bottom pilot arcs were initiated in sequence.
12. The main arc was turned on and allowed to stabilize for a few seconds to achieve steady state.
13. The test was started within the control software, which activated the traversing fixture and the data logging process.
14. When the test was complete and the fixture had stopped, the system was switched off in reverse order to the above.
15. The welded specimen was removed for analysis.

3.3.1 Establishing Secondary (Fixed) Welding Parameters

Test welds were made at presumably reasonable settings of 50 amps current and 25 mm/s speed, based on past experience with welding aluminum alloys. After confirming that these primary parameters would produce acceptable results, they were held fixed, while certain secondary welding parameters were varied to establish a reasonable combination of values. The secondary parameters considered included: plasma torch orifice size, plasma gas flow rate, torch stand-off distance and square wave AC frequency. Welds were made at several settings for each of these secondary parameters and the results assessed visually. Reasonably effective settings were established for the secondary parameters, and held fixed for all future welds.

Plasma torch orifice size:

Three (3) standard diameter sizes of orifice are supplied by the manufacturer for the torches: 2.4 mm (3/32”), 3.2 mm (1/8”) and 4.0 mm (5/32”). They correspond to the commercially available electrode diameters and common industrial practice would be to use the same diameter orifice and electrode. The orifice constrains the arc column and it was found that the smaller orifice gave the narrowest weld, with the least spatter. Therefore, the 2.4 mm diameter orifice was selected for the remainder of the experiments.

Plasma gas flow rate:

Plasma gas flow rate determines the velocity of the plasma jet exiting a given diameter orifice. The force of the impinging plasma jet onto the molten magnesium surface resulted in considerable surface irregularity at high flow rates. On the other hand, insufficient flow did not allow for a continuously maintained main arc. The pilot arc would constantly restart the main arc, resulting in an unsatisfactory weld surface. An effective flow rate was approximately 0.2 liters per minute, towards the low end of the adjustable range of 0 – 1.0 liters per minute. This finding is consistent with the use of a relatively small sized orifice.

Torch stand-off distance:

Previous work by Kwon and Weckman [36] [40] had shown how the plasma arc spreads out, with increasing distance from the orifice. Accordingly, and with the goal of achieving a narrow weld, attempts were made to reduce the torch stand-off distance to as short as possible. At very short stand-off distances, there was deterioration in weld surface quality, probably due to the effect of the pressure of the plasma jet on the weld pool. There were also instances of the torch body short circuiting to the work, at stand-off distances less than 1 mm. It was found that a stand-off distance of 1.0 mm gave best overall results and this setting was used for the remainder of the experiments. Figure 3.5 shows the difference between the surface quality of welds made at 1.0 mm stand-off in (a), and 2.5 mm stand-off in (b). The surface quality is much worse in (b), compared to (a).

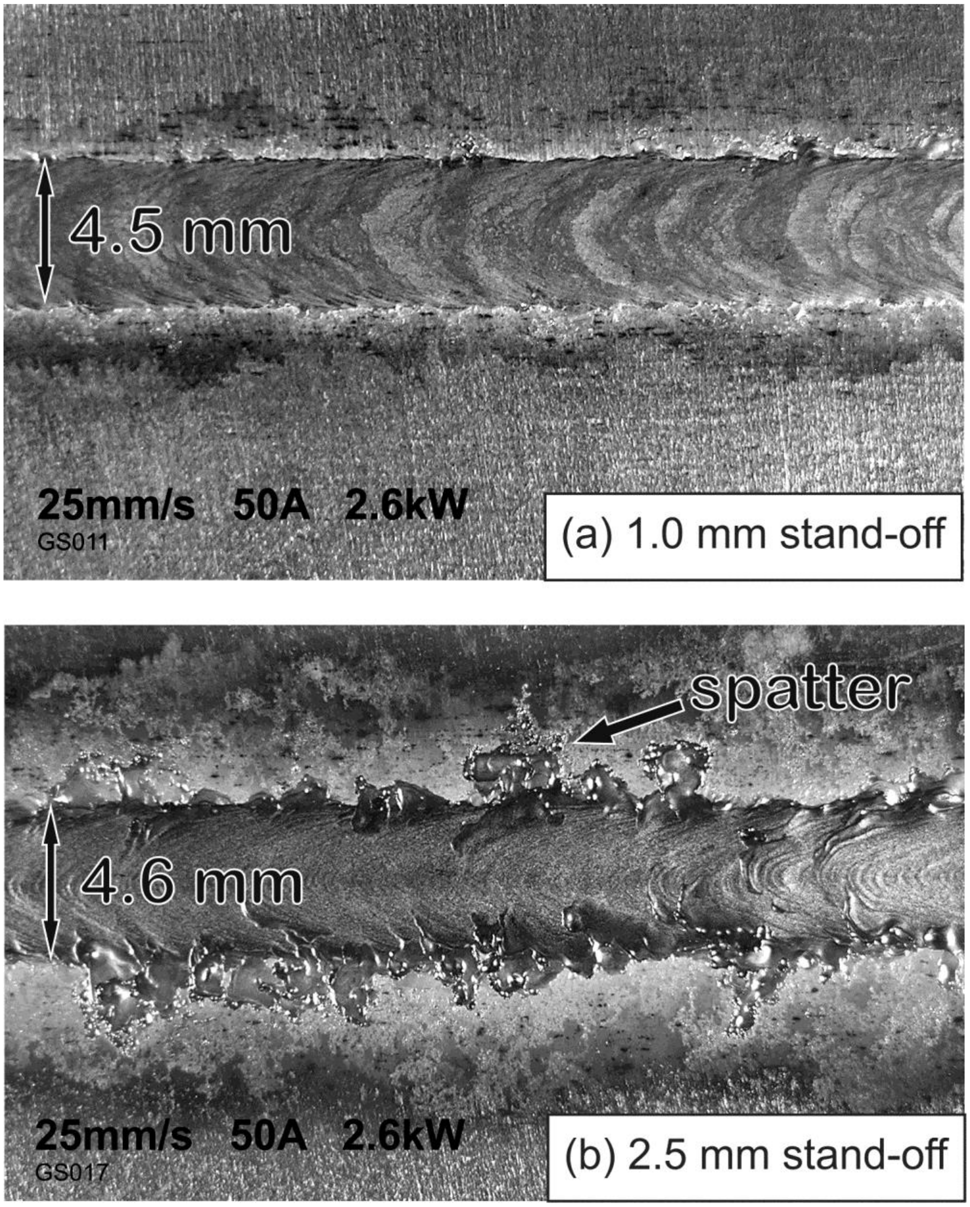

Figure 3.5: Test welds made at stand-off distances of (a) 1.0 mm and (b) 2.5 mm, showing increased spatter at greater stand-off distance.

Square wave AC frequency:

Square wave AC current is typically used for welding reactive metals, such as aluminum, titanium and magnesium, because of its characteristic cathodic cleaning effect [43] [51]. Every half cycle produces a burst of electrons leaving the cathode surface, taking with them part of the oxidized surface layer [48]. In the double-sided arc welding process, this cleaning effect occurs on one side of the work-piece during one half-cycle and the opposite side during the other half-cycle. The power supply had an adjustable frequency range, from 40 Hz to 400 Hz. After some experimentation, a frequency of 200 Hz was chosen for the rest of the experiments. This choice was based only on the perception that the sound of the arc was more regular when the frequency was set close to the middle of the adjustable range, suggesting that a more stable arc existed at this intermediate frequency. Frequency appeared to be the least sensitive of the secondary parameters that were explored in these initial tests.

Other secondary parameters were chosen based on either: (1) welding industry practice, (2) equipment manufacturers' recommendations, or (3) published results from other research [36]. Secondary parameters used for the remainder of these experiments are summarized in Table 3.2, below.

Table 3.2: Secondary welding parameters used in these experiments.

Plasma orifice diameter	2.4 mm (3/32 inch)
Plasma gas flow rate	0.2 liters / min.
Torch stand-off distance, both torches.	1.0 mm
AC square wave frequency	200 Hz
Square wave current balance (θ)	0.50
Square wave EP/EN time balance (β)	0.50
Plasma gas	Ultra high purity argon (99.998 %)
Shielding gas	Industrial purity argon (99.8 %)
Electrode material	Tungsten, 1% zirconiated
Electrode diameter and geometry	3.97 mm (5/32 inch) dia, plain flat end
Electrode set-back distance	4.15 mm (0.163 inch) (torch manufacturer recommended)

3.3.2 Establishing the Window of Primary Parameters - Batch 1 Welds

From an initial welding current of 50 amps and welding speed of 25 mm/s, the primary welding parameters were progressively increased for each subsequent weld, over a range of values to establish a window of speed and power combinations that would produce visually acceptable welds. A total of 33 welds were made using different combinations of welding speed and welding power. These were then used to define the domain of weld process parameters that could be used to produce visually acceptable welds.

3.3.3 Welds made for Tensile Testing – Batch 2 and Batch 3 Welds

Batch 2 welds were made using welding speeds and powers at 8 selected points within the parameter domain established by the Batch 1 weld experiments, above. Welding powers ranging from 1.9 kW to 4.0 kW and welding speeds ranging from 25 mm/s to 87 mm/s were used. The purpose of these welds was to examine the transverse tensile properties of the welds and to establish joint efficiencies.

Batch 3 welds were made using 20 different combinations of speed and power, within a similar range of conditions used to make the Batch 2 welds. The purpose of Batch 3 welds was to more closely examine the tensile properties of the weld metal in the fusion zone.

3.4 Post Weld Analysis of the Double-Sided Arc Welds

All welds were visually examined and measured for weld width using a low power stereo-microscope fitted with a digital read-out of stage position. The average of 7 measurements, made across the weld on both top and bottom surfaces, was taken as the weld width. Representative photographs were taken of the resulting weld surfaces.

3.4.1 Metallographic Examination

Welds were sectioned in 3 places along the weld bead, using a Struers®™ brand cold-cut abrasive cut-off saw. The first 20 mm of the weld bead was discarded, in case unsteady-state conditions may have influenced the resulting weld. A typical Batch 1 weld, after sectioning, is shown in Figure 3.6, below.

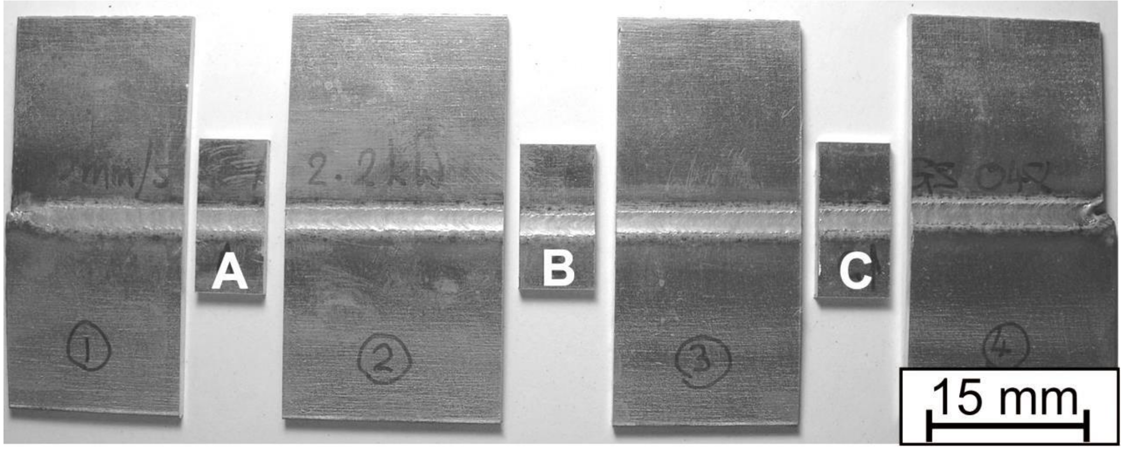

Figure 3.6: Sections removed from welds in 3 places.

The sections were cold mounted in epoxy resin and ground smooth using progressively finer grades of silicon carbide paper, up to 2400 grit. Grinding was done on a Streurs®™ brand 12 inch polishing wheel equipped with a 6-specimen automatic sample holder. Water was used as a lubricant during the grinding stage of sample preparation.

Polishing was done using Streurs®™ brand short nap polishing pads and diamond abrasive spray of 3 μm, 1 μm and 0.25 μm sizes, in sequence. Streurs®™ DP Blue lubricant was used, as water reacts with and spoils polished magnesium surfaces. Ethanol and dried compressed air were used to clean the specimens in between polishing steps. The specimens were etched with acetic-picral solution (10 ml glacial acetic acid, 4.2 g picric acid, 10 ml H_2O, 70 ml ethanol) [84] for approximately 20 s and then rinsed with ethanol and dried with an air jet.

The specimens were examined under an optical microscope to determine the extent of the fusion zone, confirm complete joint penetration, and to look for evidence of porosity or inclusions. The microstructures of the various areas of the welds were examined and representative micrographs produced using the attached camera and ImagePro®™ MC image analysis software.

3.4.2 Hardness Testing

Micro-hardness testing was performed on representative Batch 1 welds. A Leco®™ MHT brand Vickers micro-hardness tester was used for the tests, with a 500 gram load and 15 second dwell time, according to ASTM E92 *Standard Test Method for Vickers Hardness of Metallic Materials* procedure [85]. Indentations were made across the weld profile in 3 lines, adequately separated to avoid interference with each other. The diagonals of the diamond shaped indentations were measured directly on the machine using the eye-piece filar micrometer.

3.4.3 Tensile Testing

Transverse tensile testing was conducted on Batch 2 welds to determine joint efficiency under different welding conditions. The welds were large enough to allow 5 standard sized ASTM 12.5 mm (½ inch) wide, flat tensile specimens [86] to be machined from each weld. Figure 3.7a shows the geometry of the tensile specimen. The orientation of the specimens within the weld is shown in Figure 3.7b. The weld bead runs transversely across the center of the gage lengths.

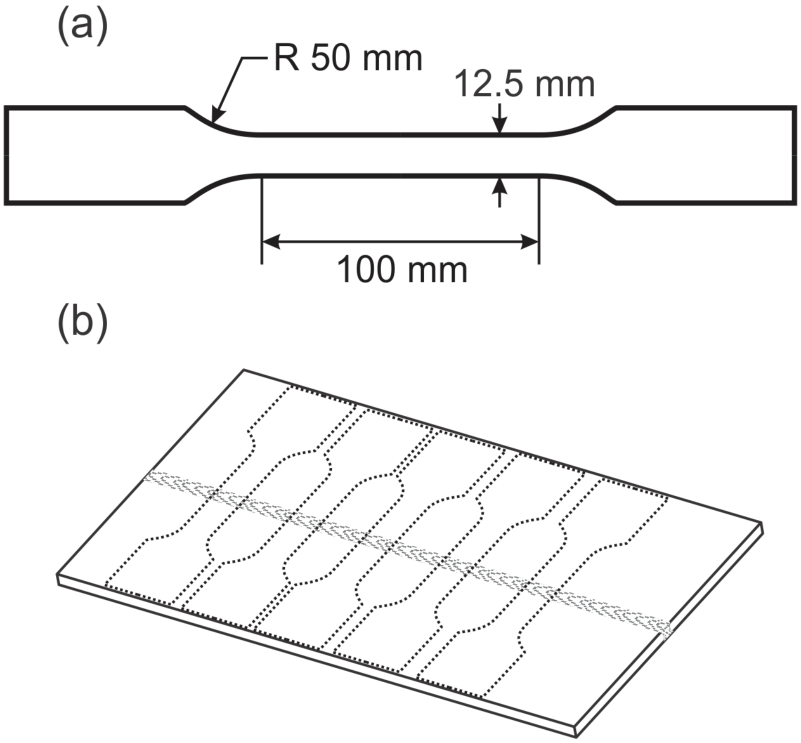

Figure 3.7: Standard sized ASTM tensile specimen: (a) specimen geometry and (b) orientation of specimens within the weld.

Transverse tensile testing was done using an Instron model 4026 universal testing machine according to ASTM E8-11 *Standard Test Method for Tension Testing of Metallic Materials* [86] procedure. The transverse tensile tests were performed at a crosshead speed of 1 mm/min, which corresponds to a strain rate of approximately 4 x 10^{-3} s^{-1} across the fusion zone, where nearly all of the strain occurs. The raw data, from cross-head displacement and load, were saved to a spreadsheet file for later analysis. Base metal specimens were also tested, oriented both along and across the rolling direction, for comparison with the welded specimens.

Longitudinal tensile testing was conducted on Batch 3 welds to determine the mechanical properties of the metal in the fusion zone, exclusively. Sub-sized flat tensile specimens, as shown in Figure 3.8a, were machined from each weld, such that the gage length consisted of only fusion zone weld metal. The welds were long enough to allow 3 tensile specimens to be removed from each, as shown in Figure 3.8b.

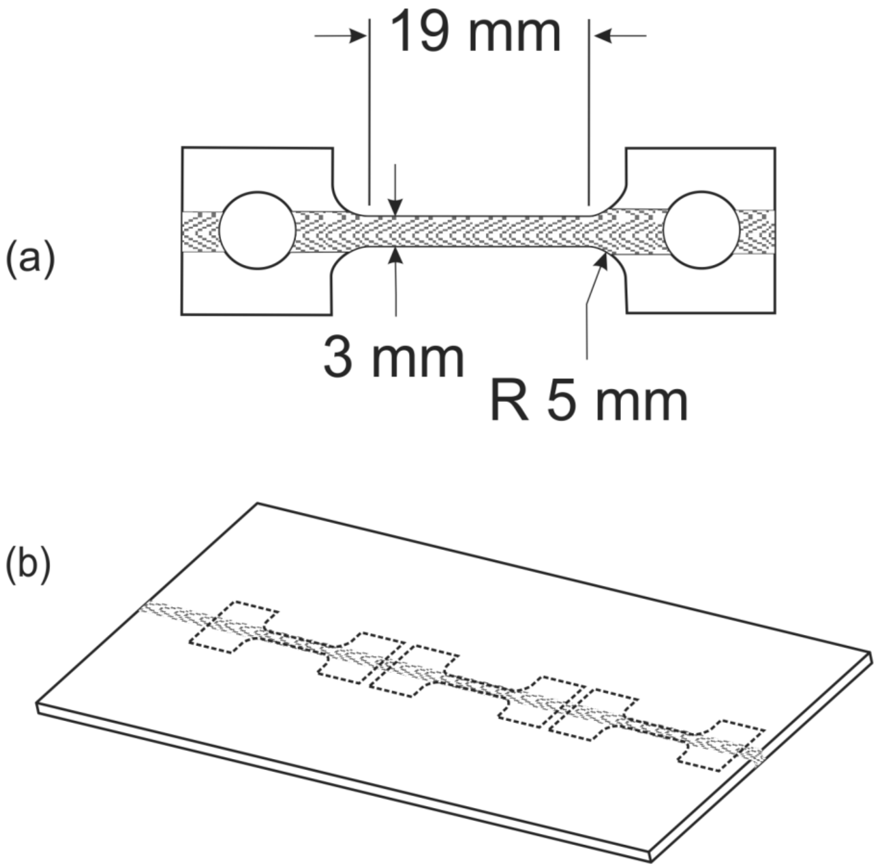

Figure 3.8: Sub-sized tensile specimen dimensions in (a) and orientation within the weld specimen in (b).

Tensile testing was carried out using an Instron model 4565 universal testing machine equipped with an extensometer of 12.5 mm gage length. A crosshead speed of 1 mm/min was used, which corresponds to a strain rate of approximately 9×10^{-4} s^{-1} within the gage length of the sub-sized specimen. The data from the extensometer and the machine’s load cell were saved to a spreadsheet file for later analysis. Base metal specimens were again tested, for comparison with both the weld metal specimens and the standard sized ASTM base metal specimens.

3.4.4 SEM-EDS Analysis

A Jeol model JSM 6460 scanning electron microscope, equipped with an Oxford Instruments model 7573 EDS chemical micro-analysis system was used to produce high magnification images and perform chemical analysis of the microstructure. Fracture surfaces and the surfaces of the weld bead were also examined and imaged.

Chapter 4

Experimental Results and Discussion

4.1 Preliminary Characterization (Batch 1 Welds)

Batch 1 welds consisted of 33 experimental welds; each made using different combinations of welding speed and welding power, for the purpose of defining the window of primary DSAW welding parameters that would lead to visually acceptable welds. Each of the 33 welds was categorized as having either, (1) blow-holes, (2) incomplete fusion or (3) visually acceptable characteristics. Blow-hole defects resulted from too much power for a given speed or conversely, insufficient speed for a given power. Incomplete fusion defects resulted from the opposite condition of insufficient power for a given speed or conversely, too much speed for a given power. If neither the blow-hole nor the incomplete fusion defects occurred, the weld was considered to be acceptable, from the standpoint of heat input.

Heat energy per unit length of weld, H_J (J/mm), can be defined in terms of welding power, Q_{weld} (J/s), divided by welding speed, v (mm/s), and has units of energy per unit length (J/mm). This is a very useful measure for discussing the results of these experiments, because it incorporates the 2 primary parameters of the welding process, Q_{weld} and v, into 1 variable, H_J, thus:

$$H_J = \frac{Q_{weld}}{v} \qquad (4.1)$$

It allows the comparison of welds made at different speeds and powers, as long as the heat energy per unit length, H_J, is the same, or at least similar.

4.1.1 Blow Hole Defects

Figure 4.1a shows an example of a series of blow holes formed in the DSAW welds made in the 2 mm thick magnesium sheet under the following conditions: Power, 1.8 kW; speed, 10 mm/s, H_J = 180 J/mm.

The blowhole defect consists of a regularly repeating pattern of holes along the center-line of the weld, with an otherwise acceptable length of weld bead between the holes.

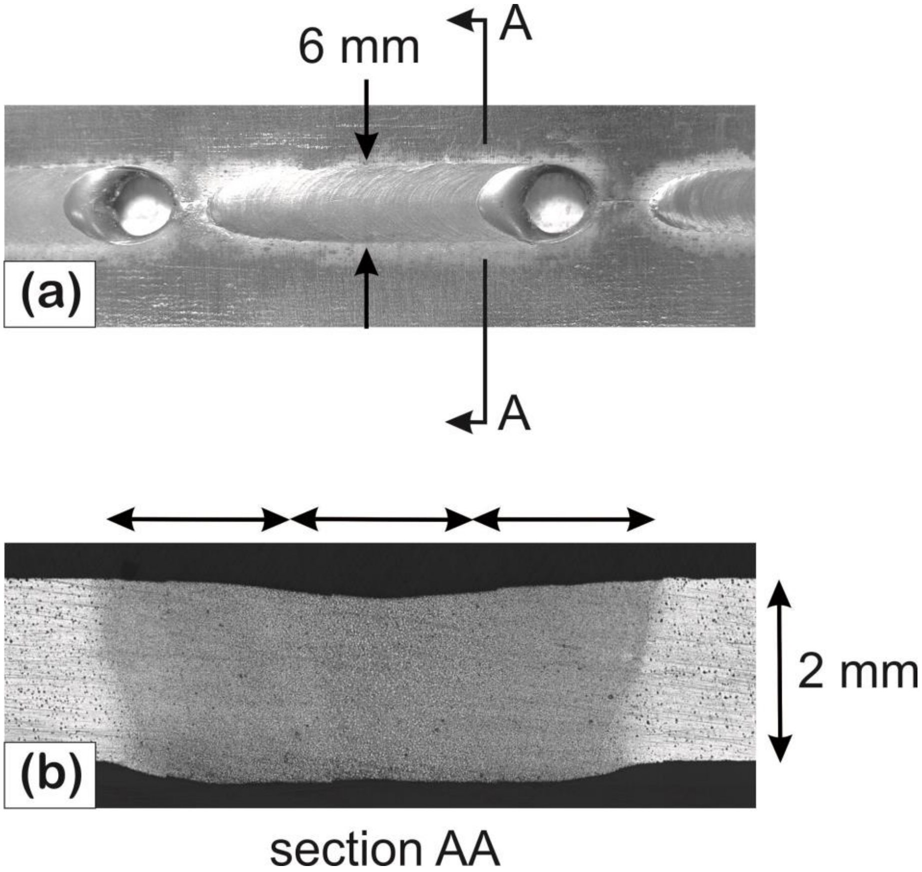

Figure 4.1: (a) Blowholes form at regular intervals along the weld when too much heat energy per unit length, H_J is used. (b) A critical weld width of 3 x sheet thickness resulted in blowholes.

Blowholes occur under conditions of excessive heat energy per unit length, H_J, and excessive weld width. Under these conditions, a wide weld pool is formed, which at some point exceeds a critical width, and holes form in the weld bead. This defect has been observed previously in DSAW welds produced in AA5182 aluminum alloy sheet, and is more fully reported in [36] and [37].

Figure 4.1b shows a section through the weld at AA. At this location, the weld is about 3 times as wide as the sheet thickness and shows signs of drop-through, due to gravity. A blow-hole forms when the weld width increases any further. At a critical weld width, the surface tension of the liquid metal can no longer support the weight, and the weld pool separates to form a hole. Once a hole has formed, the heat transfer to the metal falls to nearly zero, as the 2 arcs combine into 1 and are no longer in contact with the workpiece. The surrounding metal freezes, and heat input only rises again after the torches have re-established their arcs through the solid metal, at some small distance downstream of the hole [36].

In the present experiments, it was found that blow holes were likely when H_J was greater than around 100 J/mm. Alternatively, this limit can be expressed in terms of weld width. No weld could be made wider than 3 times the material thickness without causing blowholes.

4.1.2 Incomplete Fusion Defects

Sectioning of the welds revealed the extent of the fusion zone. If H_J was insufficient to thoroughly melt the metal throughout the entire sheet thickness, a portion of the un-melted edges remained in the center of the sheet. The resulting discontinuity represented a reduction in area of the weld throat and also a significant stress concentration feature within the weld. Such defects are highly un-desirable and are known to greatly reduce the strength of the weld [87]. If any of the 3 weld sections showed any sign of an un-melted center zone, the weld was considered an incomplete fusion defect.

Figure 4.2 shows an incomplete-fusion defect, typically observed in high speed welds. There is an area of metal in the center of the sheet that is not completely melted. A short length of the un-melted edges of the butt-joint is visible at A. Additionally, a series of small hydrogen porosity bubbles, below and above the un-melted section are visible at B. The bubbles are connected with a string-like feature, very similar to the oxide stringers reported by Joshi [38] in his work on lap-joint configuration DSAW welds in aluminum alloy 5182. Stringers occur at the faying surfaces when the metal melts but does not flow to the extent necessary to break-up the hydroxide film on the surfaces. Such a film is the source of hydrogen for the gas bubbles which form along the stringer and is a known defect in aluminum castings [88]. Figure 4.2 illustrates how stringers may exist in weld metal that has melted but not been thoroughly mixed. It is another example of the importance of surface preparation and cleanliness to successful welding of magnesium alloys. In addition to incomplete fusion defects, these welds often exhibited undercut at the fusion boundaries and hydrogen porosity, also shown in Figure 4.2.

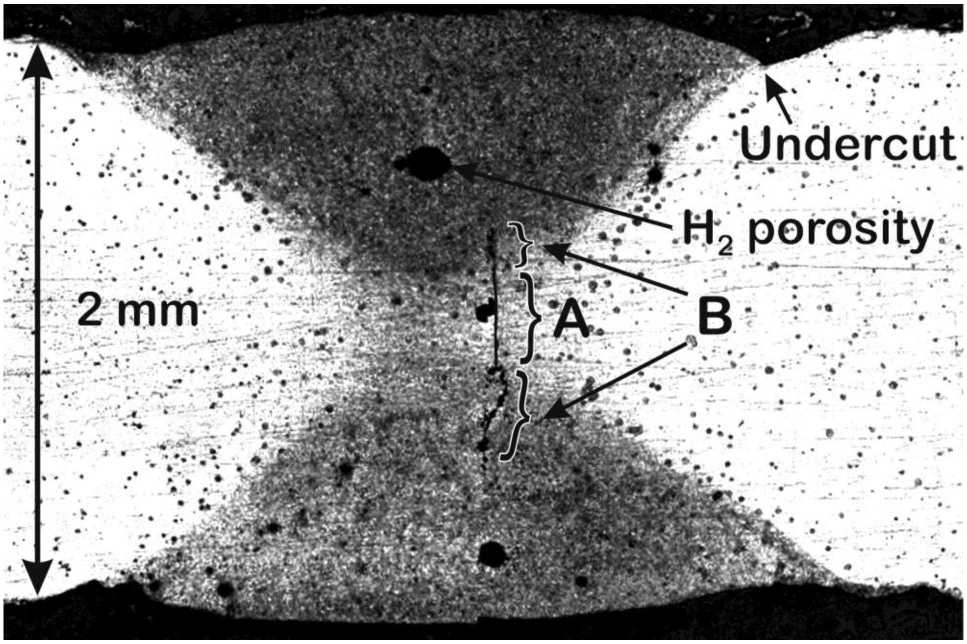

Figure 4.2: Incomplete fusion defect, undercut and hydrogen porosity typically observed in welds made at excessively high welding speeds in a DSAW weld made in AZ31 Mg sheet. The line at A is the un-melted interface of the weld specimens. The lines at B are un-disrupted oxide stringers.

4.1.3 Acceptable Welds

Batch 1 welds were considered acceptable if they exhibited neither the blowhole defect nor the incomplete fusion defect and were otherwise visually acceptable. Welds may have exhibited some less desirable characteristics, such as the presence of a few gas pores or a poor surface profile, and still be considered acceptable, if not ideal.

4.1.4 The Power/Speed Process Window

Results from examining the 33 welds made in Batch 1 are plotted on the graph shown in Figure 4.3. The data used to produce Figure 4.3 is provided in Appendix A. The graph indicates which combinations of primary welding parameters resulted in visually acceptable welds. A window is drawn around the region that gave acceptable welds. That region is bounded by a transition to blow holes on the left, a transition to incomplete fusion on the right and top and bottom limits, governed by the capabilities of the power supply or the torches.

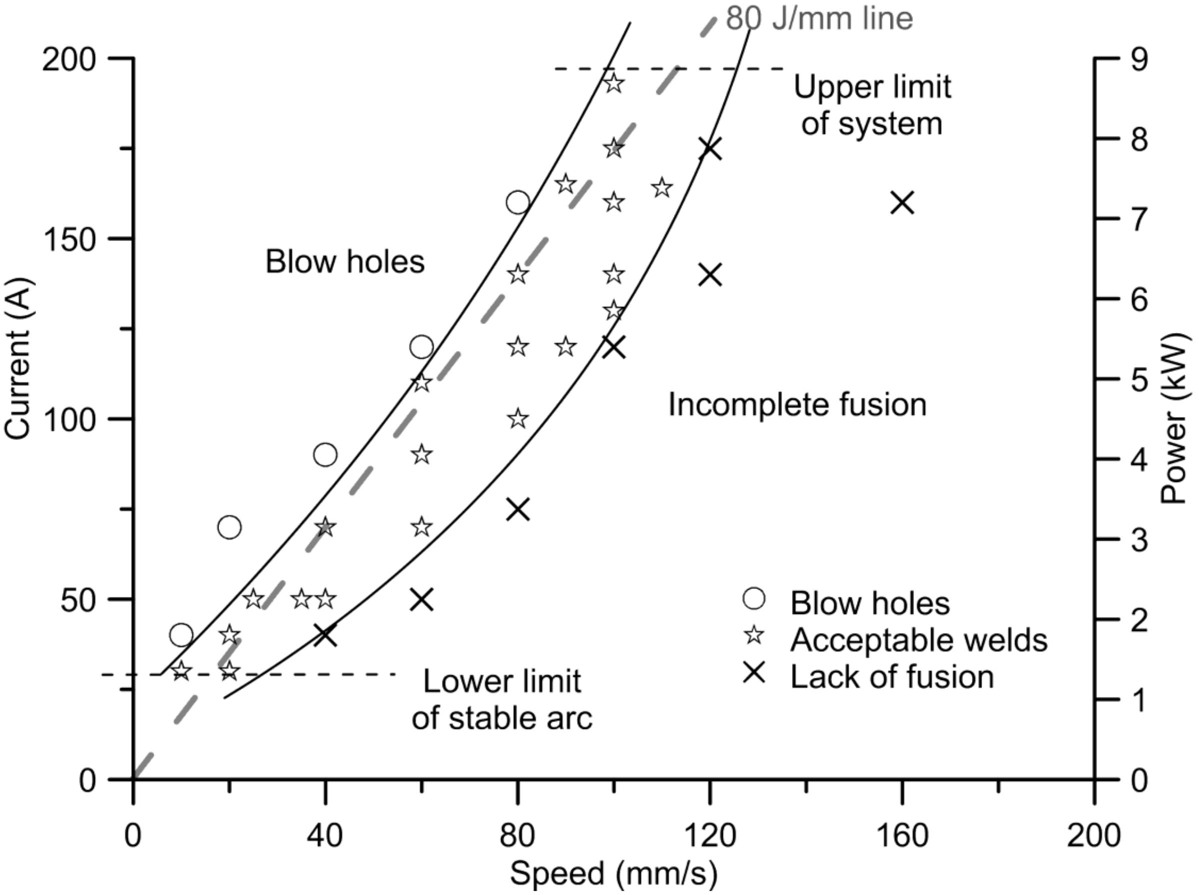

Figure 4.3: Window of primary welding parameters resulting in welds of acceptable appearance.

The welding equipment used in this study was not capable of maintaining a stable arc at current settings below 30 Amps. This lower limit is shown with a dashed line in the lower left corner of Figure 4.3. Alternatively, welds made at high power settings were found to result in rapid and excessive erosion of the plasma torch orifice. The highest current setting used in these experiments was 190 Amps. The resulting weld appeared acceptable, but the plasma torch orifice became pitted and worn after only a few seconds of welding. Therefore, 190 Amps is shown with a dashed line in the figure, as the upper limit of welding current.

Figure 4.3 shows y-axis scales of both welding current (Amps) and welding power (kW). Either scale can be used as an expression of the rate of heat input into the weld, since they are simply related by Watt's law. Power varies proportionally with current, if all other parameters are held constant. Current and power are sometimes used synonymously to describe the rate of welding heat input. Power is a more correct measure, but is not generally known in advance and is not independently controlled by a welding power supply. A constant current welding power supply will continually adjust the applied arc voltage in order to maintain a given pre-set current. A suitably instrumented system can provide data on welding power by recording the torch-to-torch voltages, but this is known only after the fact. In these experiments, where arc lengths were kept constant, a fixed relationship was found to exist between current and power. Both current and power scales are shown in Figure 4.3 for convenience.

The data from the 33 welds made as Batch 1 can also be presented in terms of weld widths and heat energy per unit length, H_J. Figure 4.4 shows such a plot with the data points categorized as before. All of the blow-hole defects are to the upper right of the plot and all of the incomplete-fusion defects are to the lower left. The acceptable welds are approximately centered on a point at $H_J = 80$ J/mm, and 4 mm weld width. This is to be expected, as the line of 80 J/mm follows the general direction of the process window, in Figure 4.3.

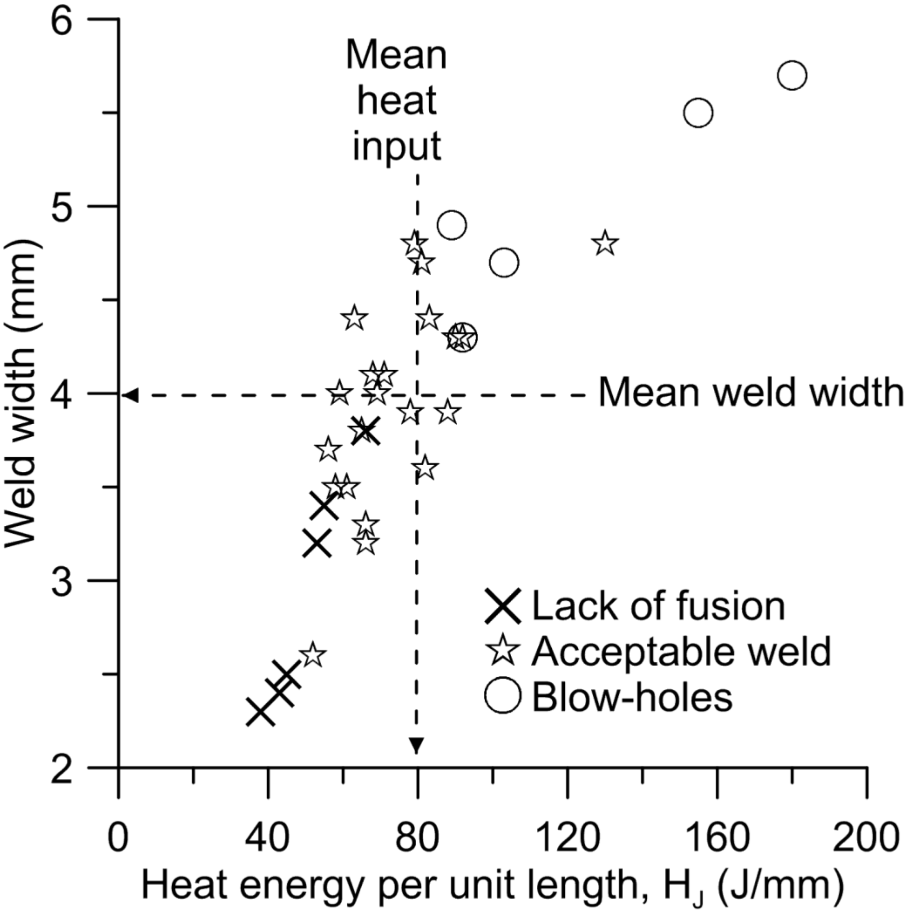

Figure 4.4: Batch 1 weld widths plotted against heat energy per unit length, H_J.

4.1.5 Effect of Welding Speed

Within the process window associated with acceptable welds, there was considerable variation in quality of the weld surface appearance. In general, welds made at low to moderate speeds resulted in a better surface appearance than welds made at high speed. Welding spatter and undercutting at the weld toe were both worse in cases of high welding speed.

Figure 4.5 shows 2 welds, one made at moderate speed, the other at a high speed. They have very comparable heat energy per unit length values of $H_J = 88$ J/mm and $H_J = 77$ J/mm respectively, and are representative of other welds made using similar parameters. The weld shown in Figure 4.5a was made at 40 mm/s, 3.5 kW ($H_J = 88$ J/mm) and that shown in Figure 4.5b was made at 100 mm/s, 7.7 kW

(H_J = 77 J/mm). Cross-sections of the weld profiles are shown to the right of each image. The surface appearance in (a) is clearly superior to that in (b).

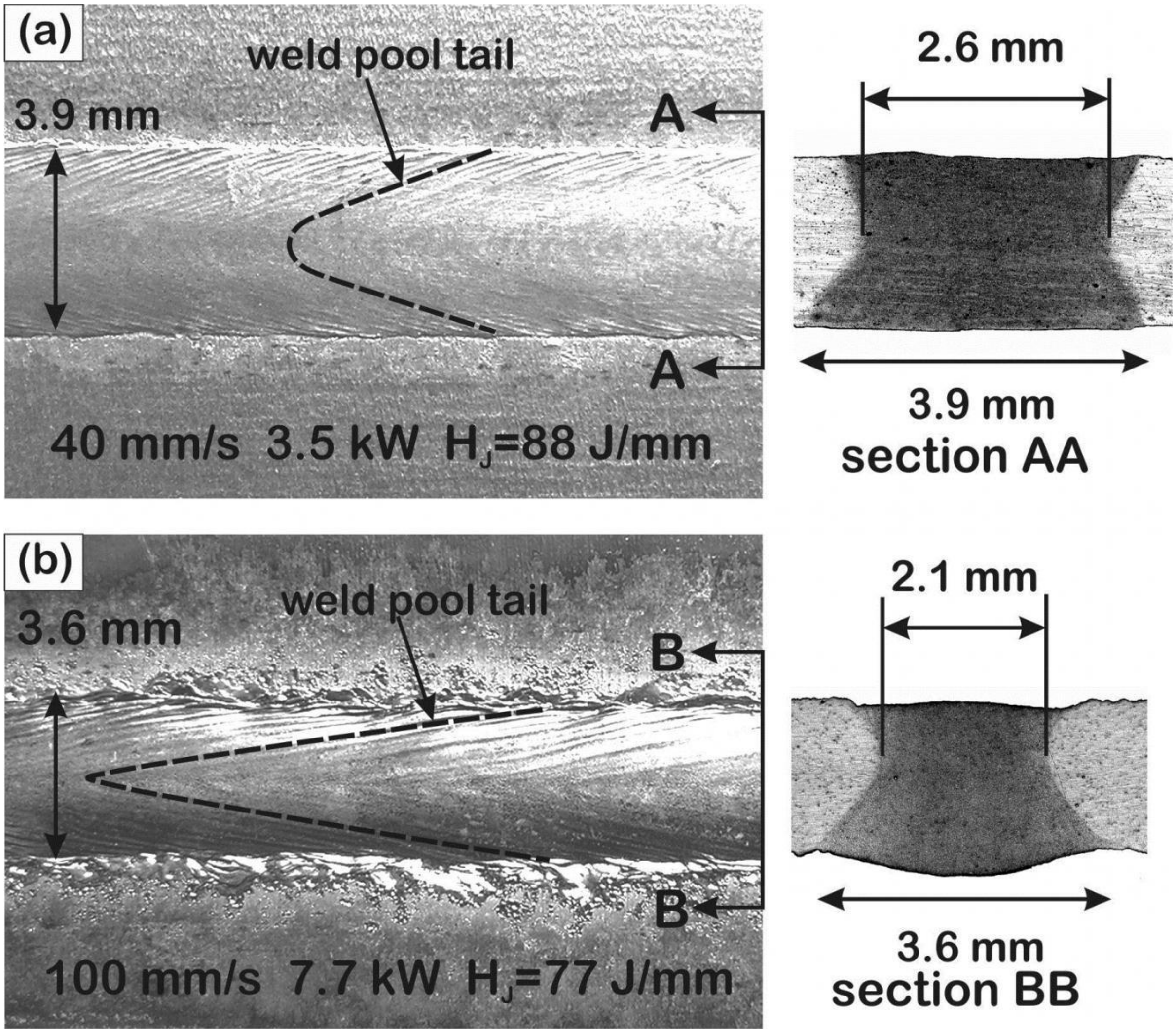

Figure 4.5: Effect of welding speed on weld profile. (a) Optimal parameters. (b) High speed weld.

The low speed weld shown in Figure 4.5a is essentially smooth and flat. There is no spatter on the surface and the weld toe is a clean line separating the weld bead from the base metal. The cross-sectional profile shows a symmetrical hour-glass shape, with the fusion zone narrowing in width from 3.9 mm at the surface, to 2.8 mm at the center of the sheet (30% reduction). The V-shaped ripples on the weld surface are a consequence of the square-wave AC power. The waveform produces a slight dip in power as the polarity crosses zero, over a short but finite time period. The ripples follow the shape of the tail end of the solidifying weld pool and give an idea of the geometry of the weld pool tail, under the given conditions.

The high speed weld shown in Figure 4.5b has pronounced spattering on the sheet metal surface and a distinct undercut at the weld toe. The cross-sectional profile shows the undercut and the series of ridges that spill out onto the surface of the base metal. The fusion zone profile is a more pronounced hour-glass shape, which narrows in width from 3.6 mm at the surface, to 2.1 mm at the mid-plane of the sheet (42% reduction). The V-shaped surface ripples have a much more acute angle and indicate a longer weld pool tail in the high speed welds.

The smooth profile shown in Figure 4.5a progressively changes to the undercut profile shown in Figure 4.5b, with increasing welding speed. The undercut profile is typical of welds made at high speeds. This result is in agreement with the existing knowledge of weld bead profile defects. Undercutting is a common defect in high speed welds and considerable research [69] [89] [90] aims to better understand the mechanism and to suppress or delay the onset of undercutting. The associated defect of humping is closely related to undercutting, but in these experiments, only undercutting was observed.

Models for the undercut mechanism can be extremely complicated, involving the interaction of several forces that induce fluid flow in the molten weld pool. The forces involved include: thermo-capillary (Marangoni) forces; electro-magnetic (Lorenz) forces; buoyancy forces; drag forces caused by the movement of the plasma over the liquid surface; and hydrodynamic forces within the weld pool [90]. The thermo-capillary (Marangoni) forces are the result of differences in surface tension between the hot melt in the center of the weld pool and the cooler melt at the edges of the pool. These forces produce a radial flow pattern on the surface of the weld pool. The radial flow may be either outwards or inwards, large or small, depending on the sign and magnitude of the coefficient of surface tension gradient, $\left(\frac{\partial\gamma}{\partial T}\right)$, where γ is the surface tension and T is the temperature. Interestingly, this coefficient is sensitive to the presence of certain impurity elements in the weld pool and this mechanism is likely to be behind the varying weldability found between different heats (batches, casts) of the same alloy [69].

Most theories suggest that the Marangoni forces are the dominant and decisive force in determining the flow pattern in the weld pool but process specific factors are also important. Research has shown that the angle at which the heat source is held to the surface of the weld has a strong influence on undercut formation [90]. This suggests that some directional force associated with the heat source is at work. In the case of plasma arc welding, the impinging jet of plasma gas is certainly a factor in determining the fluid flow within the weld pool.

The exact mechanism that causes the fluid flow in the weld pool may be uncertain but it is reasonable to say that some form of wake is left in the weld pool tail, behind a fast moving heat source and that this wake is frozen in place by the solidification front, to form the characteristic undercut profile. In the case of a slow moving heat source, the liquid has time to re-establish a smooth profile before freezing. Since magnesium is a notch sensitive material [91], any tendency towards undercutting or other flaws in the fusion zone profile, must be avoided. Therefore, optimum welds in AZ31B magnesium alloy can be achieved by using a low welding speed and low welding power.

The surface spattering flaw that mars the surface appearance of the base metal adjacent to the fusion boundary of the high speed welds was examined more closely, because of the negative effect on weld appearance. Figure 4.6 shows 2 SEM images of the weld toe. In Figure 4.6a, the edge of the weld is visible as a series of waves of frozen weld metal spilling over the base metal surface. Beyond the edge of the weld, there are many craters of varying size, formed in the base metal surface. The wire brush marks have been locally eroded away to leave a scarred, cratered surface. Figure 4.6b shows a closer view of this surface. These craters may have been formed as a result of localized boiling of the magnesium surface, after momentary contact with very hot plasma. It is known that welding arcs do not stay in one place, but wander around a local area [43]. If the arc can wander briefly onto the surface of the sheet metal, adjacent to the weld, it could cause these effects.

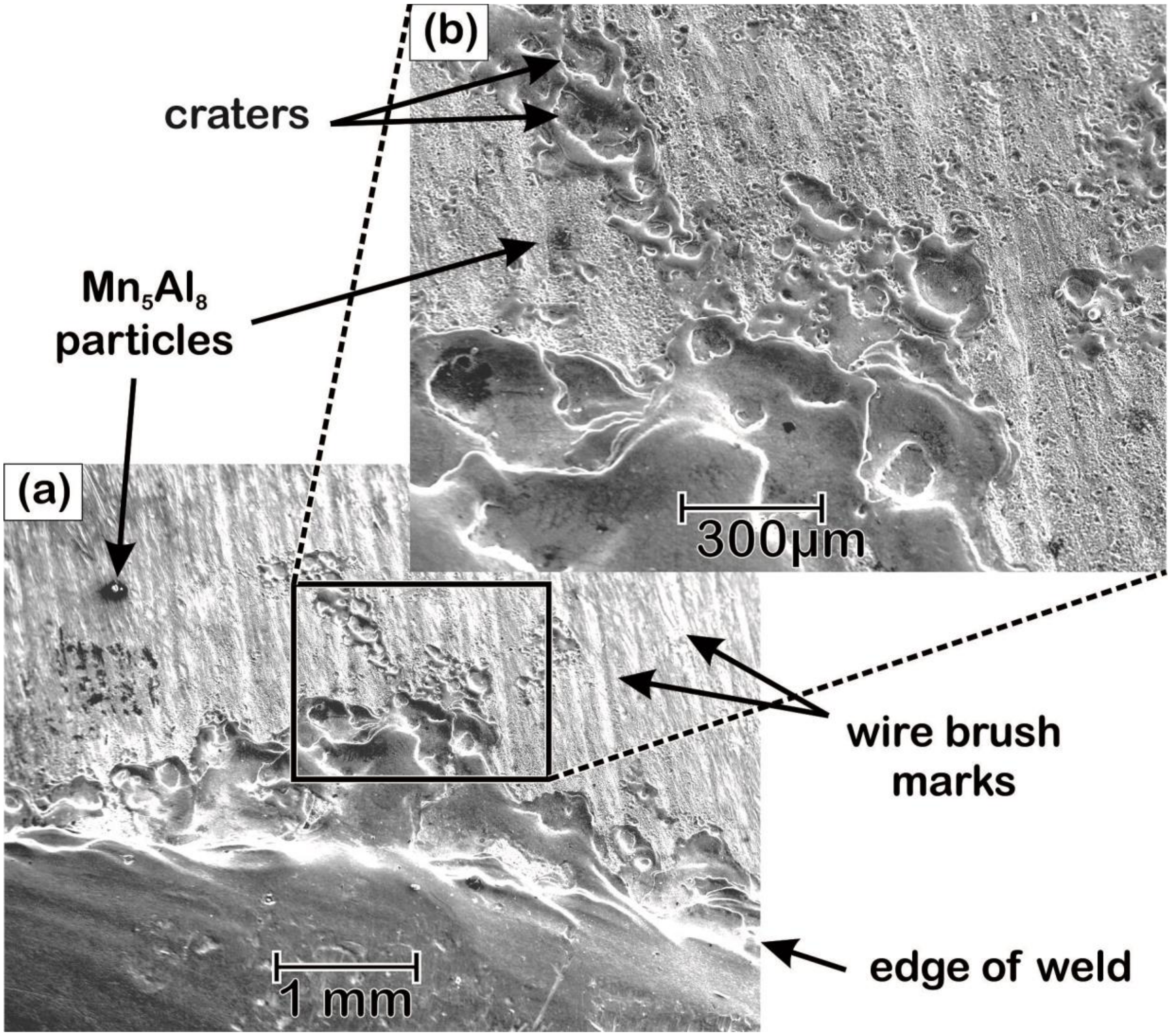

Figure 4.6: SEM image of the spatter and crater marks at the weld toe.

A more fundamental process of welding heat conduction also needs to be examined, in order to explain boiling in and around the weld pool of magnesium alloys. Figure 4.7 shows a schematic representation of the heat flux in the high and low speed welds shown in Figure 4.5. The incident surface heat flux, Q, for both the high and low power arcs is shown as two Gaussian distributions about the center of the arc column. For simplicity, only the top heat source is shown. The high power arc has slightly more than twice the heat flux of the low power arc, at their centers.

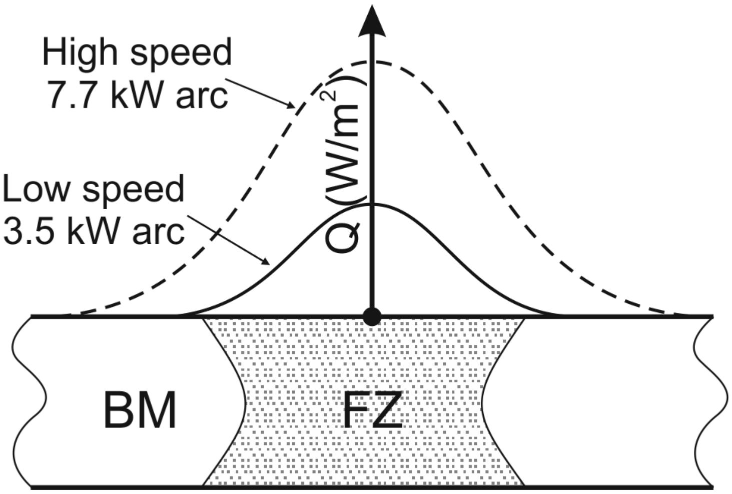

Figure 4.7: Schematic representation of the heat flux in the 2 welds shown in Figure 4.5

The difference in surface quality between the low and high speed welds shown in Figure 4.5 is likely to be related to the difference in intensity of the two arcs used. In the low speed weld, a 3.5 kW arc was used and its heat flux is represented by the solid line Gaussian curve in Figure 4.7. The intensity of the arc near the fusion boundary was likely high enough to effectively strip the oxide layer from the surface of the liquid metal, but not sufficient for cathodic cleaning of the cooler solid surface of the adjacent base metal. However, in the case of the high speed weld, the heat flux of 7.7 kW arc is more than double that of the 3.5 kW low speed weld, as shown by the dashed Gaussian curve in Figure 4.7. The intensity of the higher power arc near the fusion boundary would be proportionately higher than the lower power arc, such that there was effective cathodic cleaning of the liquid, but now also localized arc strikes or cathode spots at points of weakness in the oxide film on the surface of the solid base metal [43]. These localized strikes would act to focus the arc current onto a small surface area, thereby causing very rapid heating, melting and explosive vaporization of the underlying magnesium, thus creating the spattering and molten craters in the base metal surface at random locations adjacent to the fusion boundary, as seen in Figures 4.5b and 4.6.

When welding aluminum alloys, using square-wave AC current to promote cathodic cleaning of the oxide, it is normal to see a uniform band of cathodically cleaned oxide on the surface of the solid aluminum sheet immediately adjacent to the fusion boundary with some evidence of arc surface marking along the surface asperities aligned in the rolling direction at the very outside edge of the cathodically cleaned zone [36] [37] [38] [40] [41] [46] [48]. The pitting and spatter features observed on the surface of the AZ31B magnesium base metal immediately adjacent to the fusion boundary of the higher speed DSAW welds such as shown in Figures 4.4b and 4.6 are notably different from what is normally seen in aluminum alloy welds. These differences are likely related to differences in the physical characteristics and adhesion of the magnesium oxide layer on the solid surface, as well as the low boiling point of magnesium, which allows penetration by the arc at discrete locations, followed by rapid heating and explosive vaporization of the underlying magnesium.

Spattering and cratering problems on magnesium welds have been attributed to the low boiling point of magnesium by other investigators, including Liu, Song, and others [21] [62]. They also note that cathode spots are in continuous movement over the weld pool and occasionally wander onto the surface of the base metal, adjacent to the weld pool. Researchers continue to look for welding techniques that will constrain the heat source to a smaller area. The use of laser-arc hybrid welding power sources is one promising line of investigation, as there is evidence of a synergistic improvement in performance by having both power sources simultaneously interacting with the metal. It appears that the focused laser spot is capable of anchoring the arc to the same spot on the metal surface, thus avoiding any arc wandering and raising the overall energy density of the process [32].

The specific conclusion to be drawn from the above is that the appearance and profile of DSAW welds in AZ31B magnesium alloy sheet can be optimized by selecting the lowest welding power and welding speed that is practical. If weld appearance and profile are of high importance, then lower welding speeds can be justified. If welding speeds and powers are increased, then spattering and cratering of the surface of the base metal, adjacent to the fusion line can be expected. The surface of the magnesium alloy boils before the heat can conduct into the metal below.

4.1.6 Porosity Defects

Welds made in magnesium alloys are prone to hydrogen porosity in a similar way to welds made in aluminum alloys [92]. The defect is a consequence of hydrogen being much more soluble in liquid magnesium than in the solid metal [93]. Any hydrogen available in the weld area is rapidly drawn into solution in the molten weld pool. The hydrogen is then rejected out of solution, just ahead of the solidification front, as the weld metal freezes [94].

Hydrogen is available in the form of oils and other hydrocarbons that may be present on the metal surface. It is also available from the high temperature dissociation of water molecules that may be present, either in the shielding gas, or as water vapor in the atmosphere. There is also an abundant source of hydrogen in the form of the hydrated oxide layer which forms, to varying degrees, on the surface of all bare magnesium [12].

Gross gas porosity refers to cases where the fusion zone is so filled with spheroid shaped gas pores that it resembles a sponge. The weld shown in Figure 4.8 was made using magnesium sheet that was cleaned, but not wire brushed. It shows the resulting gross porosity in the fusion zone. The condition was caused by severe contamination of the weld by the hydrated oxide layer on the surface of the sheet.

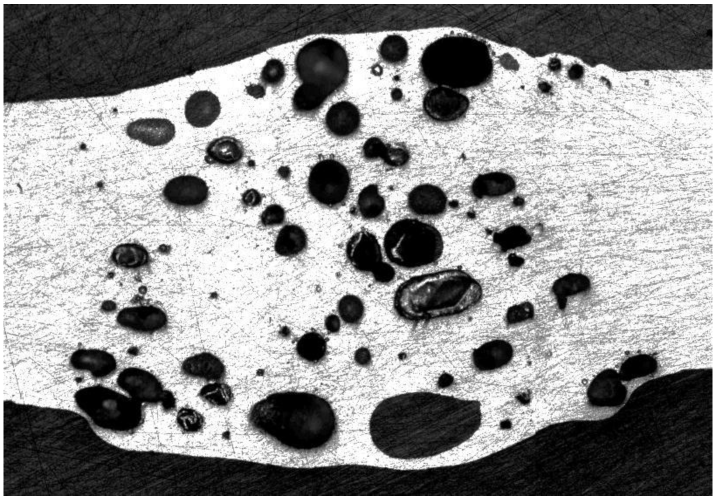

Figure 4.8: Gross porosity in the fusion zone caused by hydrogen bubbles.

All other welds in this study were made with careful attention to the cleaning procedure described in Section 3.2.2, *Pre-Weld Material Preparation*. For this reason, there was little evidence of hydrogen porosity in most of the remaining weld cross-sections. Where hydrogen porosity was observed, it was invariably in welds made at high welding speeds.

Welds made at speeds up to 40 mm/s showed no evidence of hydrogen porosity. This was probably because any hydrogen bubbles had time to escape the weld pool before it froze. Kwon and Weckman [36] [40] captured images of hydrogen bubbles escaping from the molten weld pool of their double-sided arc welds, made with AA5182 aluminum alloy. It is reasonable to suppose that hydrogen bubbles would leave the liquid magnesium in a similar way.

Referring back again to Figure 4.2, several gas bubbles can be seen in the fusion zone. They range in size from very small to 100 μm across. Being spheroidal, they do not act as stress risers and result in degraded mechanical properties, only in proportion to their area fraction, which is very small. As long as the pores do not connect together with cracks or oxide stringers, slight porosity is not considered a critical defect [95]. Unfortunately, many of the porosity bubbles seen in these high speed welds do link up with discontinuities of some kind. Therefore, any gas bubbles in high speed welds should be taken as a sign of possible cracking problems.

Figure 4.9 shows another example of gas porosity in a high speed weld. This example looks very similar to the oxide tail defects observed by Joshi [38] in his DSAW welds of AA5182 aluminum alloy. Such defects occur in high speed welding when there is insufficient time for the surface oxide layer on the faying surfaces to be disrupted by fluid flow within the weld pool. This string-like discontinuity in the fusion zone causes reduced ductility in the weld metal. In order to avoid these defects, welds should be made at a lower welding speed and power, to allow more time for the fluid flow within the molten fusion zone to disrupt and break up any oxide stringers left from the melting of faying surface metal.

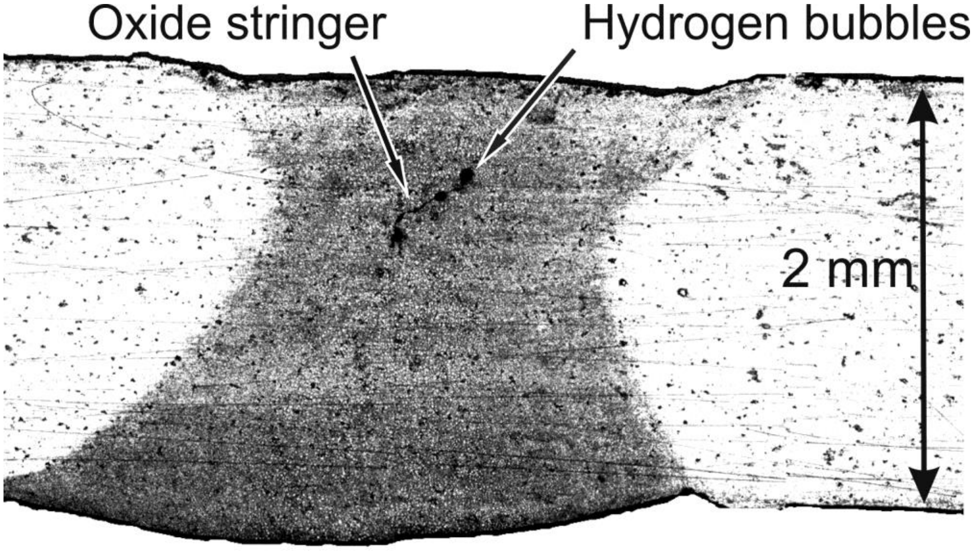

Figure 4.9: Another example of gas porosity pores connected with an oxide stringer.

4.2 Microstructure

The weld microstructure was examined using both an optical microscope and a scanning electron microscope (SEM) in order to characterize the changes that occurred in the metal as a result of the welding process.

4.2.1 Base Metal

The microstructure of rolled AZ31B-H24 base metal is shown in Figure 4.10. It consists of angular grains, most of which are in the 2-3 micron size range. Many of these grains are elongated and appear to have been sheared by the rolling process. There are also some much larger grains, up to about 20 microns across. Close parallel lines, indicating twinning, are to be seen in many of the larger grains.

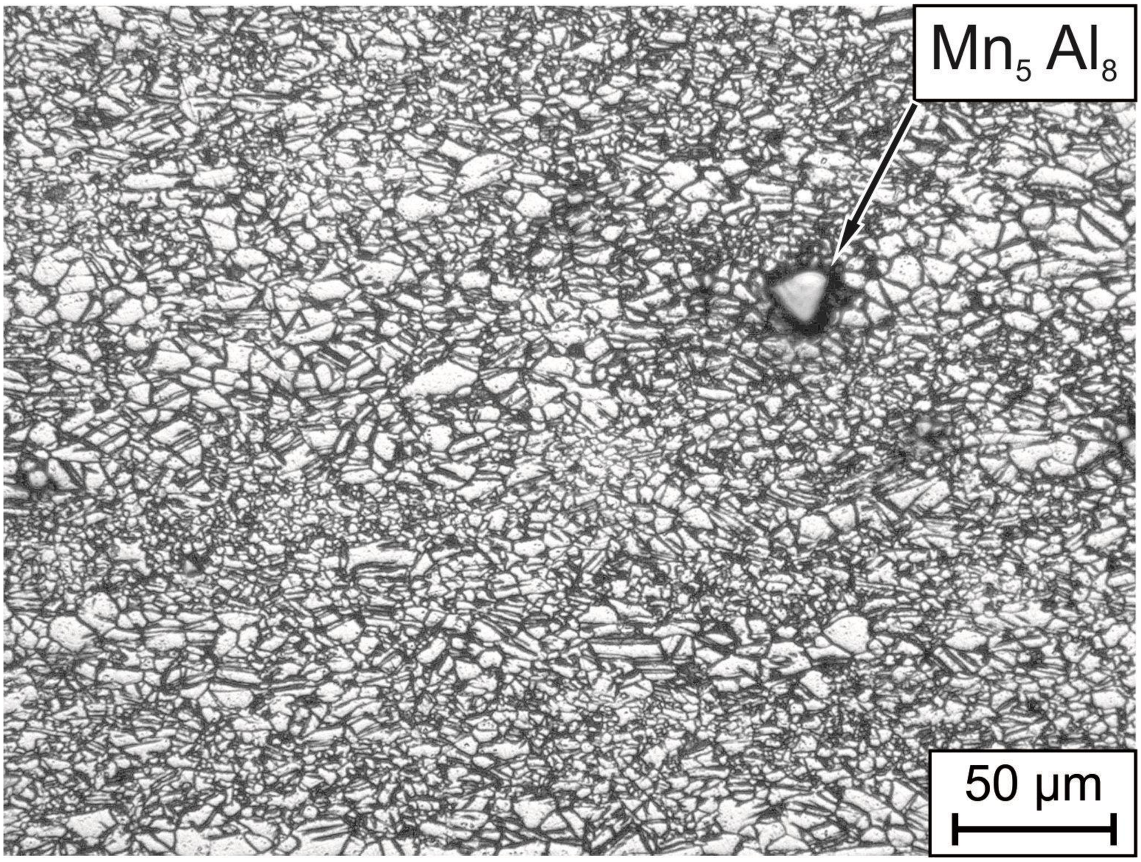

Figure 4.10: Optical micrograph of the AZ31B-H24 base metal.

Clusters of large grains and clusters of small recrystallized, equiaxed grains are arranged in layers along the rolling direction. This bimodal distribution of grain sizes is due to the H24 temper, signifying partially annealed and recrystallized. The smaller grains have been recrystallized and show no signs of twinning, whereas the larger grains have not yet undergone this process.

Second-phase particles of Mn_5Al_8 intermetallic compound are seen throughout the material. They are angular, faceted particles that exist in all sizes up to about 20 microns across. The larger ones are easily seen as distinct from the primary phase. Being much harder, they remain raised above the surrounding polished surface. The microstructural features seen in the base metal are consistent with those reported by other researchers working with this particular alloy. Liu *et al.* [21], Song *et al.* [62], Dong *et al.* [92] and others report similar descriptions of base metal microstructure in their publications. This is additional confirmation that the material used in this study was representative of commercially produced AZ31B-H24 magnesium alloy.

4.2.2 Heat Affected Zone (HAZ)

After welding, the base metal adjacent to the weld was locally affected by the heat of welding to form a heat affected zone (HAZ). The HAZ extends outward from the weld to a varying distance, depending on welding speed and heat input. Low speed welds had wider heat affected zones, extending to over 8 mm from the weld center-line. Higher speed welds had narrower heat affected zones, extending only 3 or 4 mm from the weld centerline. The difference in the width of the heat affected zones is due to the different lengths of time in which the heat source is in contact with any given section of the metal surface at different speeds.

Figure 4.11 shows an optical micrograph of the microstructure in the HAZ, adjacent to a typical weld. The small grains seen previously in Figure 4.10 have grown and combined to become larger but fewer in numbers. Grain sizes in the heat affected zone range between 5 and 30 microns across. Some clustering of smaller and larger grains is still evident but the banded pattern is not so clear. The sheared, elongated shape of the deformed grains in the base metal has given way to an equiaxed structure and all sign of twinning is absent.

The second phase Mn_5Al_8 particles in the HAZ are still visible as small black particles in Figure 4.11. Some have grown in size and appear more reflective under an optical microscope. A large Mn_5Al_8 particle is indicated in the figure. It has a polished top surface surrounded by a darker ring, suggesting that the surrounding material has been lowered by the polishing and etching processes, leaving the hard Mn_5Al_8 particle protruding above the surface.

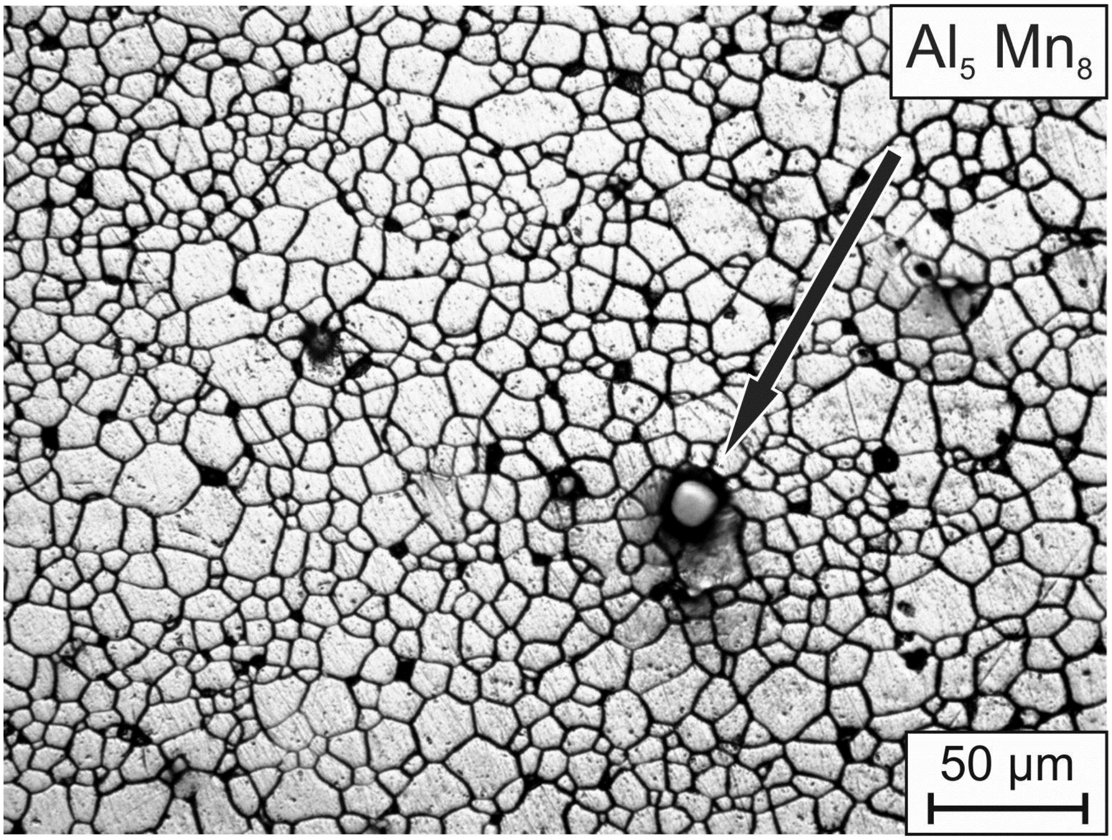

Figure 4.11: Optical micrograph of the microstructure in the heat affected zone, adjacent to the weld.

4.2.3 Partially Melted Zone (PMZ)

Figure 4.12 shows a photomicrograph of the transition from the heat affected zone, through the partially melted zone, to the fusion zone. Average grain sizes are around 20 microns across the transition. At the far left of the image, the structure is identical to the HAZ, shown in Figure 4.11. The structure changes to that of the partially melted zone towards the center of the image. The thickened grain boundaries suggest liquation of the metal in these regions.

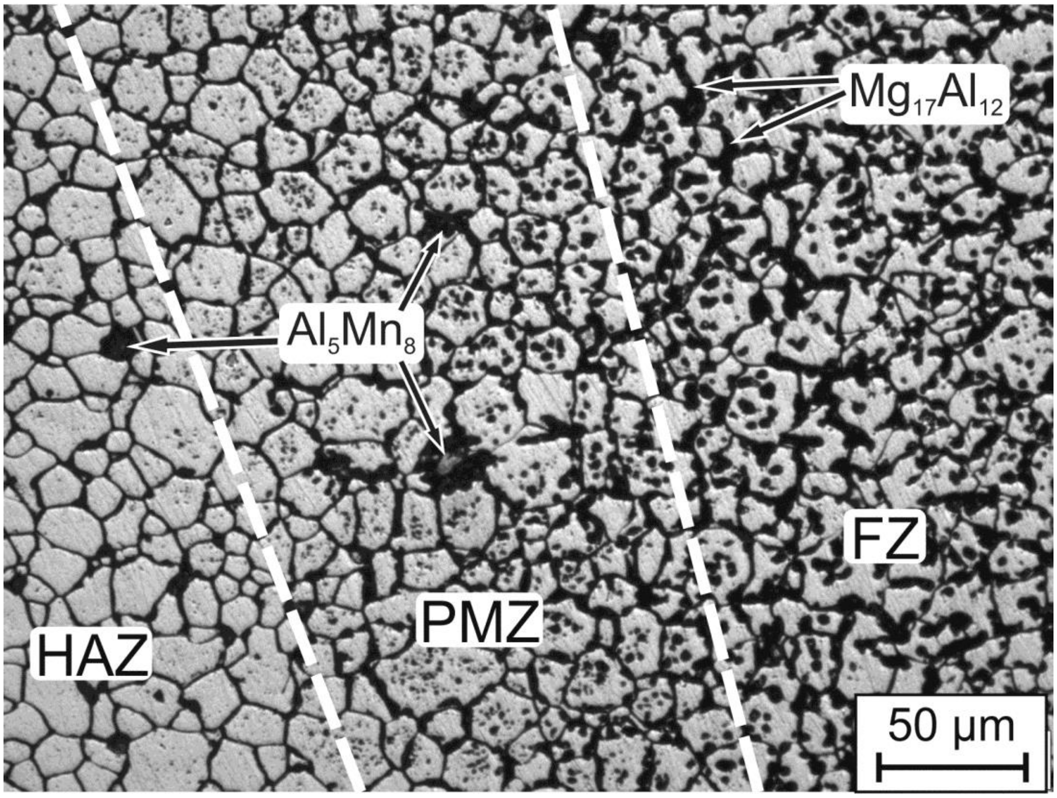

Figure 4.12: Photomicrograph showing the transition from the heat affected zone to the fusion zone.

Further to the right, the grains have wider, black interconnected areas between them. These blackened areas result from the action of the etchant on magnesium with a higher concentration of the solute atoms Aluminum and Zinc. At the center of these black areas, the solute concentration is the highest, exceeding the 13 wt% (11.5 at%) level required to form the eutectic β-phase, $Mg_{17}(Al/Zn)_{12}$. Aluminum and zinc are interchangeable atoms in the β-phase so there is a total of 4 wt% solute atoms available in the AZ31 alloy. The light areas are the relatively solute-lean, equiaxed dendrites of α-magnesium. No examples of columnar dendrites were evident in these welds.

4.2.4 Fusion Zone (FZ)

The fusion zone microstructure is shown in Figure 4.13 and is slightly courser grained in the center of the weld than at the edges, near the PMZ. The lower temperature gradient and slower cooling rate at the weld center would account for this. Figure 4.13 contains 2 optical micrographs of the fusion zone of a typical weld.

The general equiaxed dendritic structure is shown in Figure 4.13a, with grain size averaging around 25 microns. The etchant reacts with the solute rich material at the grain boundaries, staining it black. The white areas are lean in solute atoms, are thermodynamically more stable and remain unstained by the etchant. Particles of Mn_5Al_8 can be seen in the center of some dendrites as light gray shapes. They have a melting point of over 1500 °C and do not melt in the liquid weld pool [23]. On cooling, they act as inoculants for heterogeneous nucleation, hence their presence in the center of the dendrites.

The image in Figure 4.13b is at a higher magnification and was carefully etched to stain the dendrites a tan shade, to varying degrees, depending on the orientation of the basal plane. Grains with basal planes coplanar with the image are left white, while others are stained to darker shades of tan, depending on their crystallographic orientation. The 6-fold symmetry of one favorably oriented dendrite is shown in the image. Solute rich areas are stained dark gray to black, depending on the aluminum content. The deeply etched large areas of black are the sites of $Mg_{17}(Al/Zn)_{12}$ β-phase particles.

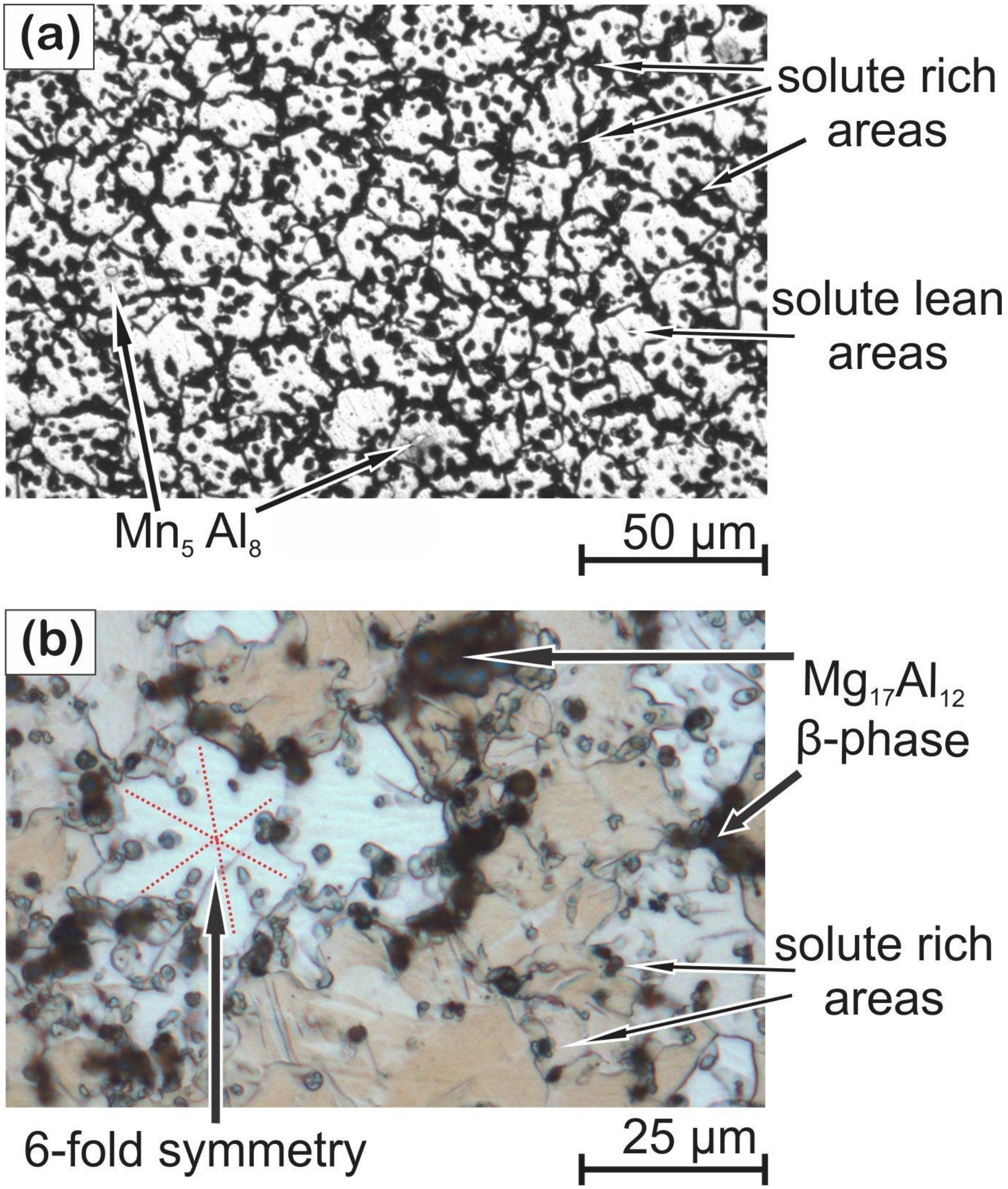

Figure 4.13: Optical micrographs of the fusion zone of a typical weld. (a) White, equiaxed dendritic grains with black, solute-rich material in between. (b) Favourably oriented grain exhibits 6-fold symmetry.

An SEM image of the fusion zone microstructure is shown in Figure 4.14. The lighter areas correspond to high solute concentration and the darker areas to reduced solute concentration.

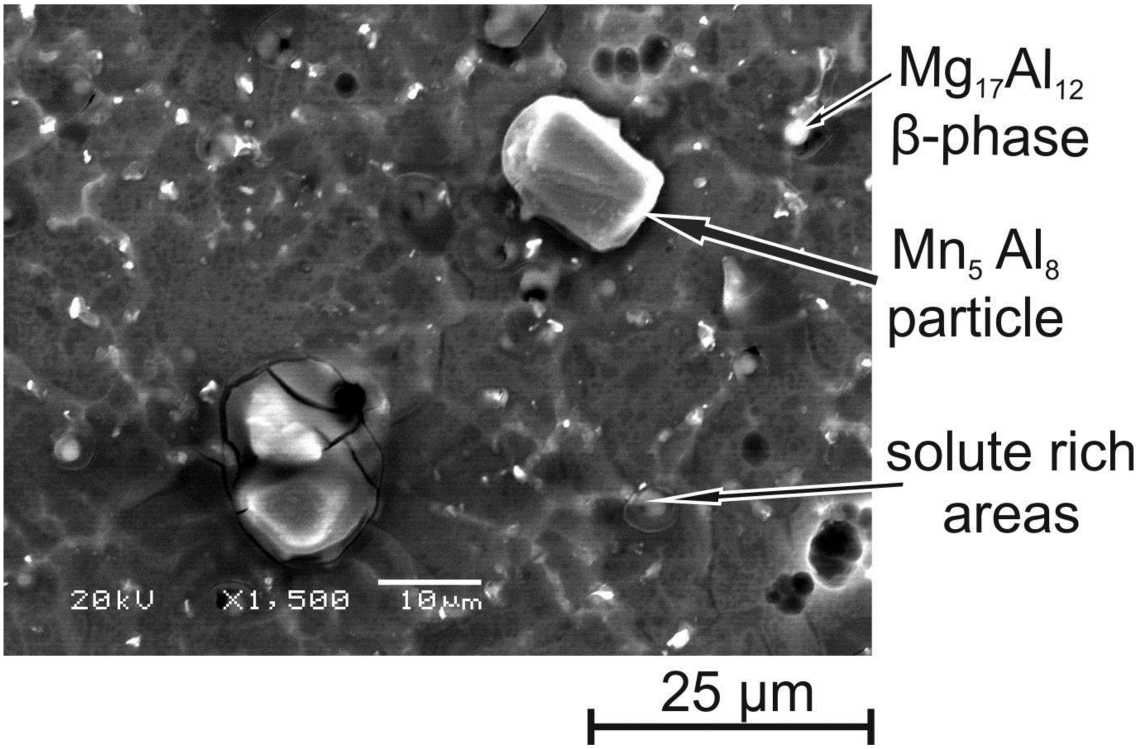

Figure 4.14: SEM image of the microstructure of a typical fusion zone.

The patterns of light gray trace out the grain boundaries. The white areas at some of the grain boundaries are the $Mg_{17}(Al/Zn)_{12}$ β-phase particles. Analysis using EDS detected levels of aluminum and zinc in these areas, approximately in proportion to the stoichiometric ratio of the β-phase. The image also contains a large Mn_5Al_8 particle and another light area with micro-cracks. The composition of the latter could not be accurately determined by EDS analysis, but the cracks suggest the likelihood of either the β-phase material, another Mn_5Al_8 particle or a combination of the two.

4.3 Mechanical Properties

The mechanical properties of the welds were examined using hardness testing, transverse tensile testing and longitudinal tensile testing.

4.3.1 Hardness Profile

Figure 4.15 shows a hardness profile through a weld made under optimal conditions. The slightly hour-glass shaped fusion zone is visible in the center of the image, as well as the 3 rows of indentations made in the weld cross section. The hardness is lowest at the center of the weld (57 VHN) and rises back to the original base metal hardness of over 70 VHN outside of the heat affected zone. This softening is to be expected as the base metal is in the half-hard H24 temper, the weld metal is in the as-fabricated F temper and the HAZ is in the fully-annealed O temper, transitioning progressively to the half-hard H24 temper of the base metal. These measured hardness values are within the range of nominal hardness values published by ASM International and other sources [2] [15]. There was no observable difference in hardness through the sheet thickness direction.

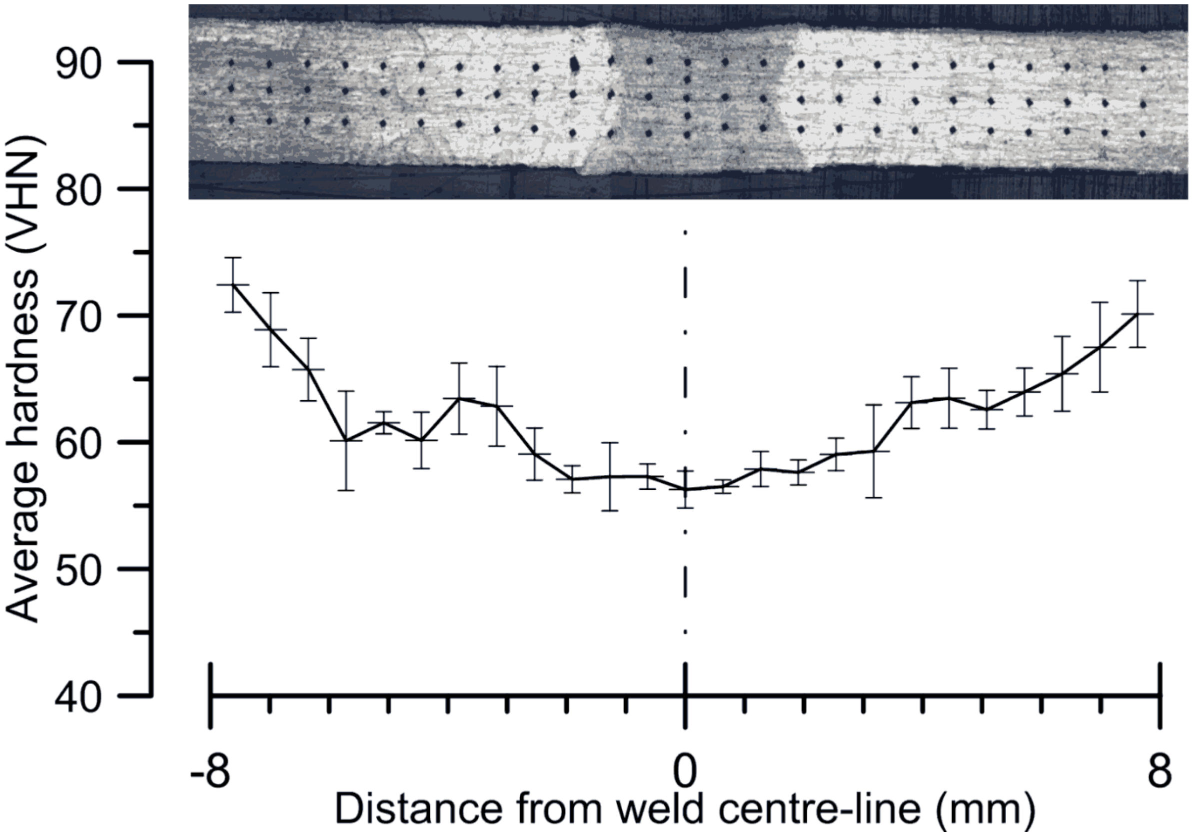

Figure 4.15: Hardness profile across a weld.

4.3.2 Transverse Tensile Testing (Batch 2 Welds)

Weld transverse tensile test results are meaningful when compared to results from identical, homogeneous base metal specimens. The ratio of the UTS of the welded specimen to the UTS of the base metal specimen is known as the joint efficiency. Joint efficiency is seldom close to 100%, even under ideal conditions. That is because joint efficiency reflects the loss of mechanical properties due to several factors, including: softening in the HAZ, metallurgical changes in the FZ and stress concentration effects of the irregular weld bead surface [61].

Figure 4.16 shows the measured tensile curves of the base metal. The samples tested had yield stresses greater than 250 MPa, UTS values of around 330 MPa and maximum elongations of 12 to 14 %. These results are very close to the values published in the ASM Handbook [2]. As expected, the sheet metal has slightly higher tensile strength along the rolling direction than perpendicular to the direction of rolling.

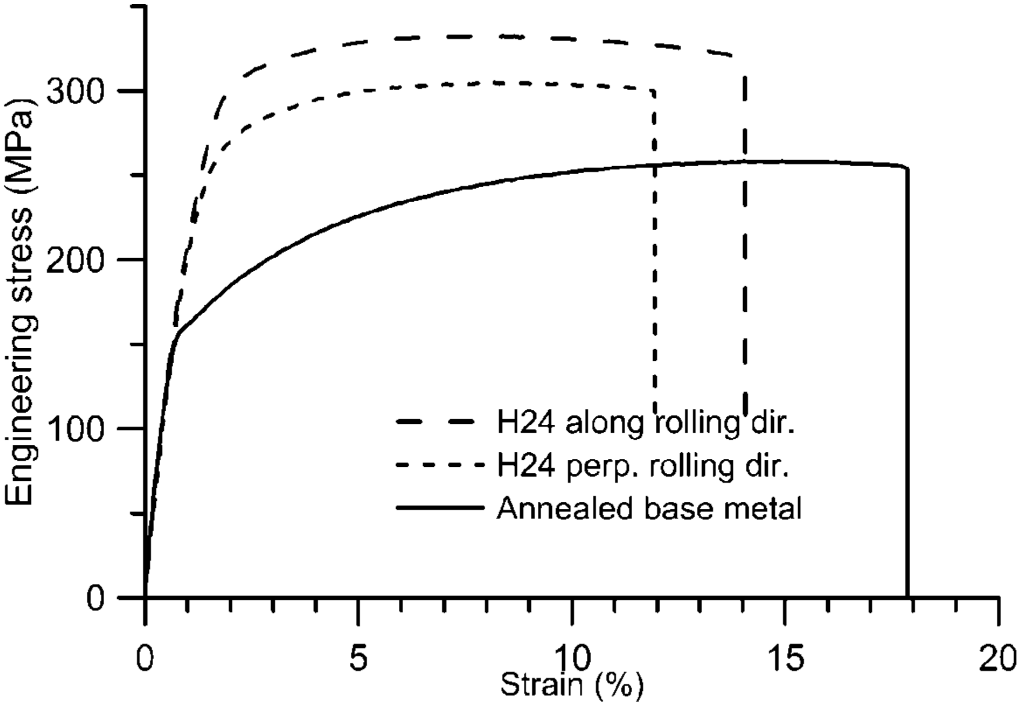

Figure 4.16: Measured base metal tensile properties.

The solid line shows the measured properties of the fully annealed base metal. This is the expected condition in which the welded specimens would be. The fully annealed base metal had a yield stress of 150 MPa, a UTS of 250 MPa and maximum elongation of 18%. These results are summarized in Table 4.1. Note that the UTS in the annealed state is about 80% of the UTS in the H24 temper.

Table 4.1: Measured base metal tensile properties and ASM Handbook **[2]** published values.

	YS (MPa)		UTS (MPa)		Max. elongation (%)	
Temper condition	H24	annealed	H24	annealed	H24	annealed
Measured value	250	150	332	250	14	18
Published values from ASM Handbook [2]	220	150	290	255	15	21

Results from the transverse tensile testing of Batch 2 welds are summarized in Table 4.2, and presented graphically in Figure 4.17. Average UTS values with standard deviations are shown. When compared to the 332 MPa UTS of the base metal along the rolling direction, joint efficiencies of around 80 % can be claimed. This was expected, since the weld metal was in the fully annealed state and this condition had been found to have tensile properties of around 80% of the H24 (half hard) condition material. Joint efficiencies in this range have also been found in other studies of AZ31B-H24 welds. Padmanaban *et al.* [61] reported joint efficiencies of 85% for GTAW welds in this alloy. Chowdhury *et al.* [75] reported 83% joint efficiency in their work on laser welded AZ31B-H24.

Table 4.2: Summary of results from transverse tensile testing of Batch 2 welds.

Speed (mm/s)	Power (kW)	Heat input, Q (J/mm)	UTS (MPa)		Joint efficiency
			Average	Std dev	
Base metal (measured)			332.0	1.7	
25	2.3	92	243.0	2.1	73%
35	2.3	66	271.8	4.2	82%
45	3.6	80	265.2	1.9	80%
57	3.6	63	265.9	3.7	80%
60	5.0	83	286.4	1.0	86%
73	5.0	68	265.3	3.5	80%
87	5.0	57	256.3	5.7	77%
73	6.4	88	254.5	8.3	77%

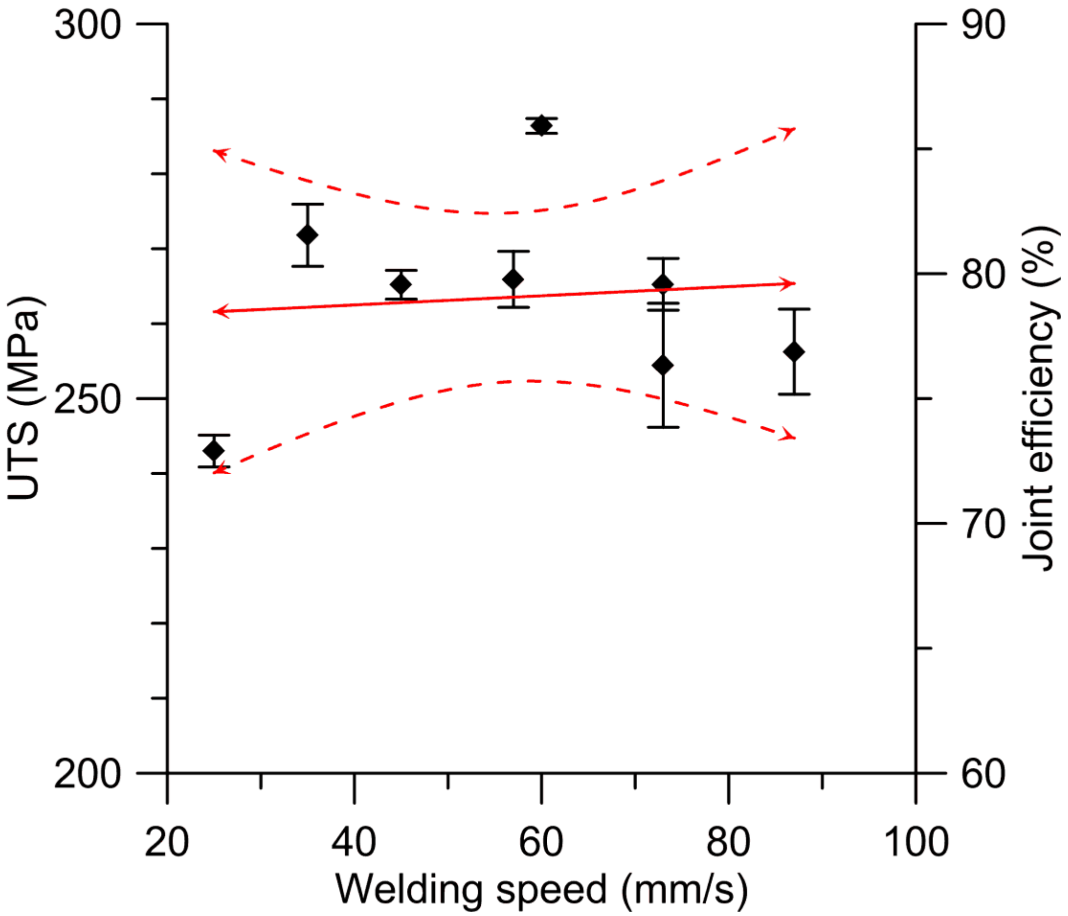

Figure 4.17: Transverse UTS results at different welding speeds.

A line of best fit is shown in red on the plot. The line is essentially flat, suggesting that there is no correlation between welding speed and transverse UTS, for these specimens. The dashed red lines represent the limits of the 95% confidence interval. This is another way of saying that if many more welds were made, there is a 95% chance that the measured transverse UTS and joint efficiency would fall between these 2 dashed lines. The 95% confidence interval widens considerably towards the ends, indicating that there is little certainty as to the slope of the line. Therefore, the only conclusion to be drawn from this result is that there is no correlation between welding speed and UTS or joint efficiency.

All of the transverse tensile test specimens fractured across the middle of the fusion zone. Figure 4.18 shows a typical fracture surface, after the transverse tensile testing of the standard size ASTM specimens. There is a clean fracture line across the middle of the fusion zone. Some welds had a more jagged fracture, with surfaces at 45 degrees to the testing axis.

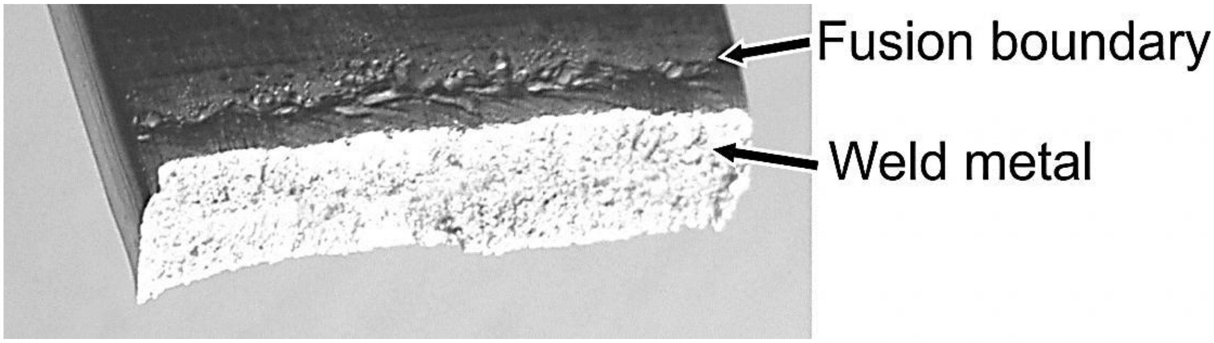

Figure 4.18: Fracture surface of a typical 12.5 mm wide transverse tensile test specimen.

The SEM images in Figure 4.19 show the scalloped surfaces typical of a ductile fracture. Figure 4.17a shows several steep valleys where separation between adjacent grains has started. This suggests that the inter-granular regions contain brittle material and is consistent with the observed microstructure. The image in Figure4.19b contains a large (40-50 microns across) particle of Mn_5Al_8. It suggests that these particles grow as a consequence of the welding process, as they are much smaller and more widely dispersed in the base metal. Large Mn_5Al_8 particles provide fracture paths, as their facetted surfaces adhere poorly to the adjacent material.

The results of the transverse tensile testing of the Batch 2 welds suggest that all of the welds were mechanically sound, with no obvious defects. The joint efficiencies were comparable to those reported by other researchers working with this alloy. There was no observable variation in UTS over the range of welding speeds and powers used.

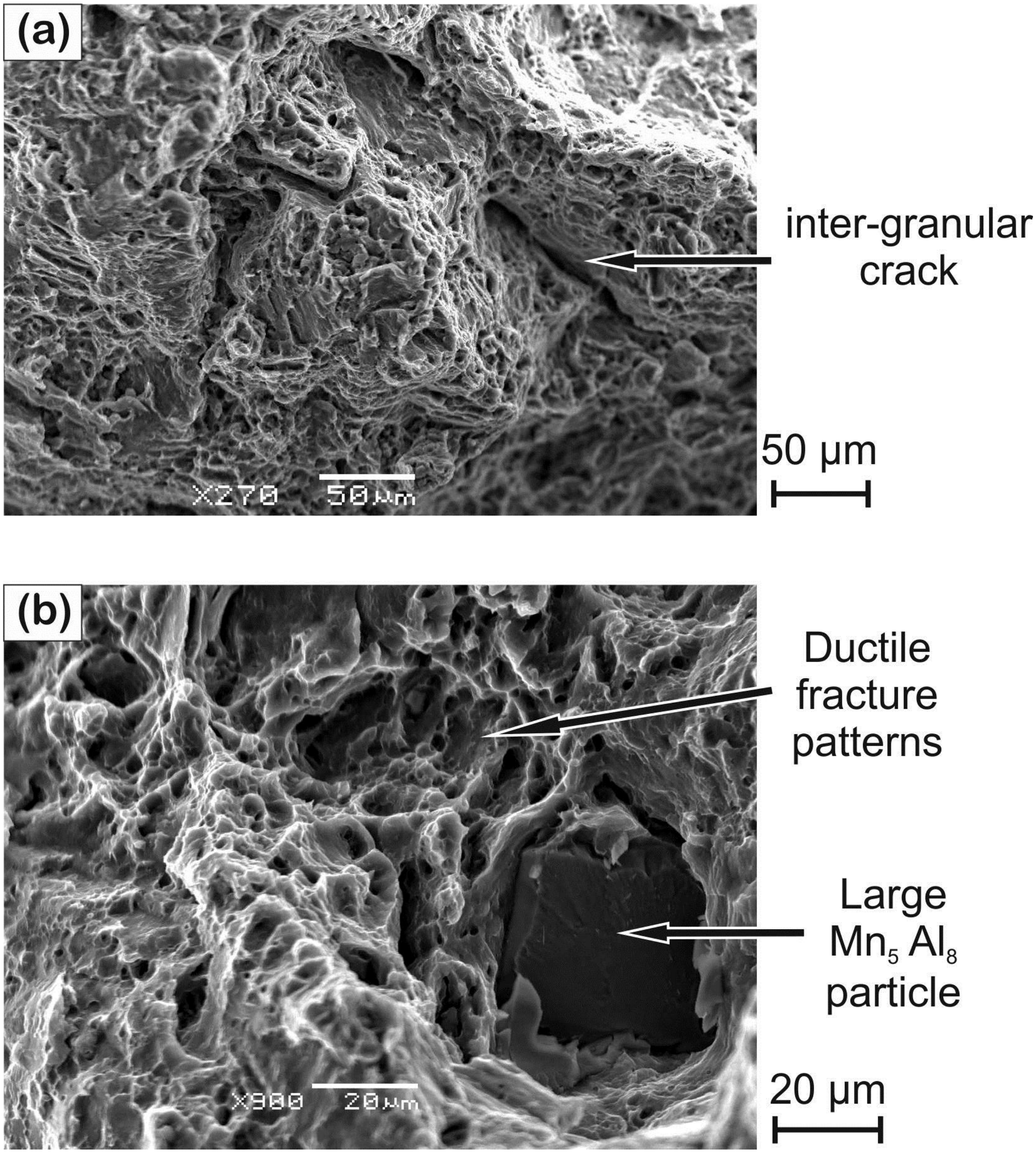

Figure 4.19: SEM images of the fracture surfaces of a typical 12.5 mm wide transverse tensile test specimen. (a) Ductile fracture scallops and inter-granular separation. (b) Fracture path crosses a large Mn_5Al_8 particle.

4.3.3 Longitudinal Tensile Testing (Batch 3 Welds)

No meaningful information regarding strain to failure can be obtained from transverse testing of the welds, as described in the previous Sub-Section. Strain is not uniform along the gage length of the specimen due to the differences in microstructure and material properties. The majority of the strain occurs in the narrow, softer area, in and around the weld.

Measuring the strain to failure of the weld metal requires tensile testing of exclusively the fusion zone weld metal. Such testing of welds is referred to as *longitudinal* tensile testing and involves the careful removal of all of the base metal around a weld bead in order to test a specimen composed of exclusively the fusion zone weld metal, along the welding direction. Only in the case of large weld beads is it possible to use the standard sized ASTM tensile specimen geometries. The narrow weld widths involved in these experiments required the use of smaller sized longitudinal tensile specimens, as described in Sub-Section 3.4.3 and Figure 3.8. Random point defects may therefore have had greater influence on the results than would have been the case with the standard sized ASTM tensile specimens. Tensile results along the longitudinal direction also differ from the transverse results because the fusion zone is unlikely to be isotropic. Nonetheless, the sub-sized specimen's tensile behaviour should be essentially identical to the standard ASTM specimen, according to past research at the University of Waterloo by Smerd *et al.* [96].

Batch 3 welds were made for the purpose of longitudinal tensile testing and provided results for welds made at 19 different combinations of speed and power. The parameters were selected from within the lower portion of the “Acceptable” window, established previously. Figure 4.18 shows the welding parameters chosen for these welds as blue diamonds on the plot.

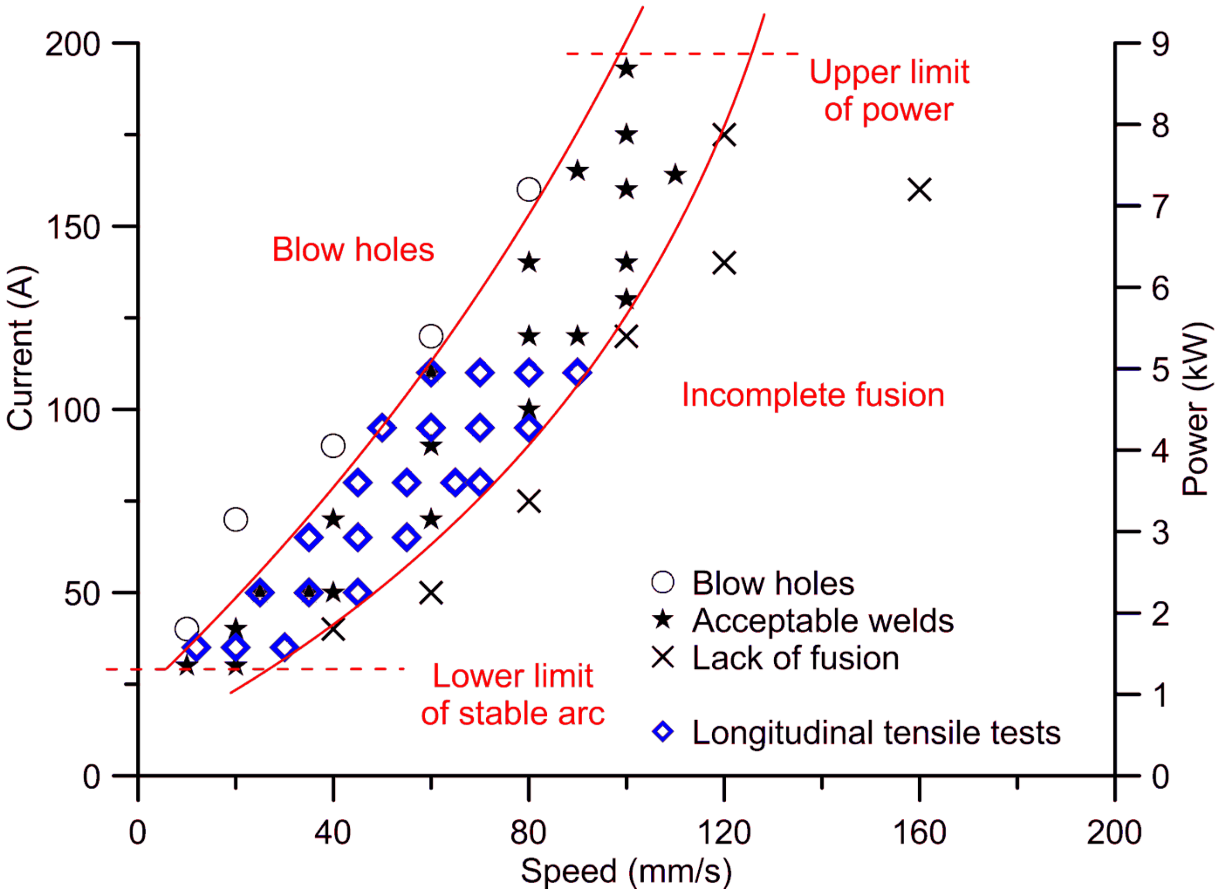

Figure 4.20: Longitudinal tensile test weld parameters, shown as blue diamonds on the process map.

Table 4.3 summarizes the results obtained from the longitudinal tensile testing of Batch 3 welds. It includes measured yield stress, UTS and maximum strain values for the average of 3 replicates, with standard deviations. Measured values are also given for an identically sized base metal sample, along the rolling direction.

Table 4.3: Summary of results from longitudinal tensile tests of Batch 3 welds.

Speed (mm/s)	Power (kW)	Heat input, H_J (J/mm)	Yield stress (MPa)		UTS (MPa)		Max strain (%)	
			Average	Std dev	Average	Std dev	Average	Std dev
Base metal, along rolling direction			263	11	306	8	12	2
12	1.6	133	70.3	9.0	190.0	20.3	16.3	1.0
20	1.6	80	31.7	9.8	147.1	15.2	18.7	1.9
30	1.6	53	27.6	5.0	113.7	7.4	12.8	1.0
25	2.3	91	56.1	7.4	180.3	13.1	16.8	0.6
35	2.3	66	37.7	7.3	149.5	14.6	15.6	2.6
45	2.3	51	22.6	5.2	110.6	14.3	16.2	1.1
35	3.0	86	12.4	0	89.9	1.9	11.5	2.0
45	3.0	67	14.0	0.1	77.4	1.5	12.3	1.3
55	3.0	55	13.7	0.1	79.4	1.3	12.0	2.3
45	3.6	80	14.9	0.2	74.0	3.7	15.0	0.8
55	3.6	65	14.8	0.0	62.1	23.7	15.9	0.0
65	3.6	55	14.1	0.4	69.1	5.0	10.4	2.9
70	3.6	51	14.7	0.0	60.6	0.0	6.0	0.0
50	4.3	86	14.8	0.2	58.9	10.2	7.4	2.3
60	4.3	72	14.1	0.2	59.6	6.0	8.4	1.7
70	4.3	61	14.0	0.4	59.0	7.1	8.1	1.3
80	4.3	54	14.2	0.1	62.7	3.7	8.5	1.1
80	5.0	63	14.5	0.2	54.0	11.7	8.3	3.2
90	5.0	56	14.1	0.1	48.0	8.4	5.8	2.2

All of the results show a downward trend with increasing welding speed and power. Graphing the results may show some connection between the welding parameters and the measured mechanical properties. The following 3 figures contain plots of yield stress, UTS and maximum strain, vs. welding speed. Figure 4.21 is a plot of 0.2% offset yield stress (YS) against welding speed. YS falls rapidly from a high value of around 70 MPa, at very low welding speeds, to around 20 MPa at speeds of 40mm/s. At yet higher welding speeds, the YS falls off only slightly more, to 15 MPa, at the highest speeds investigated. There is a definite threshold in welding speed, of approximately 40 mm/s, above which the YS is not significantly lowered by a further welding speed increase.

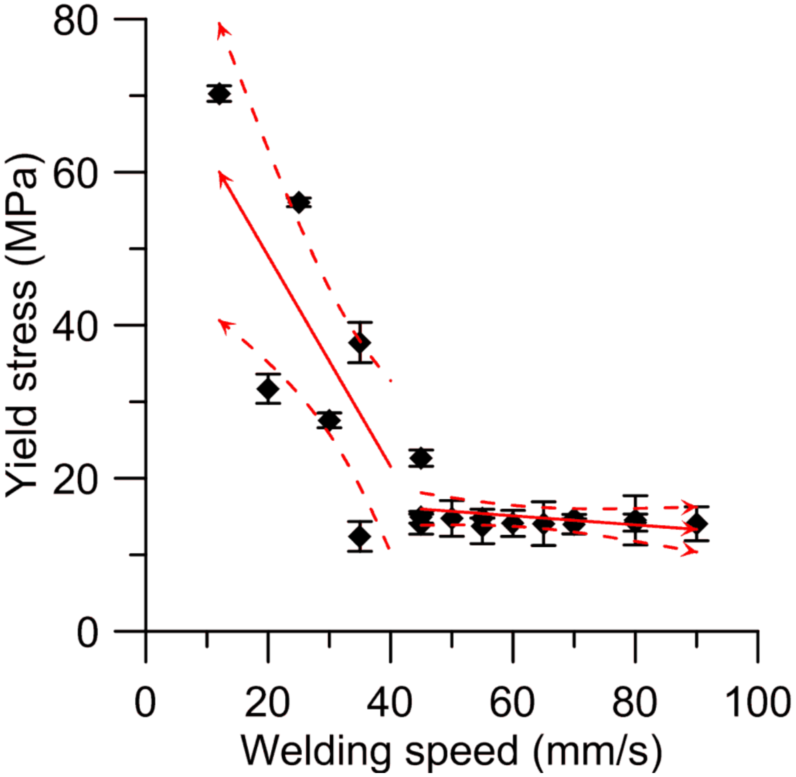

Figure 4.21: Effect of welding speed on yield stress.

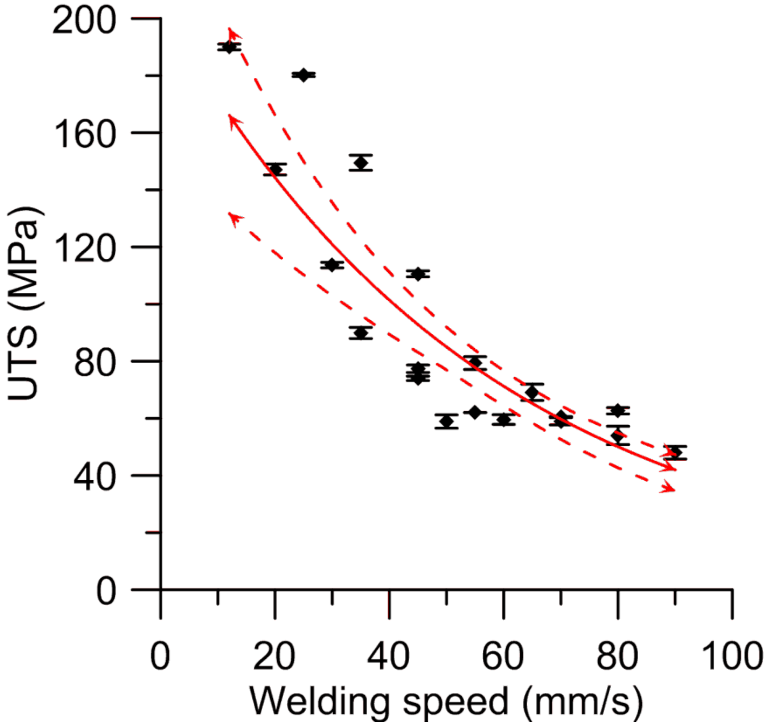

Figure 4.22: Effect of welding speed on UTS.

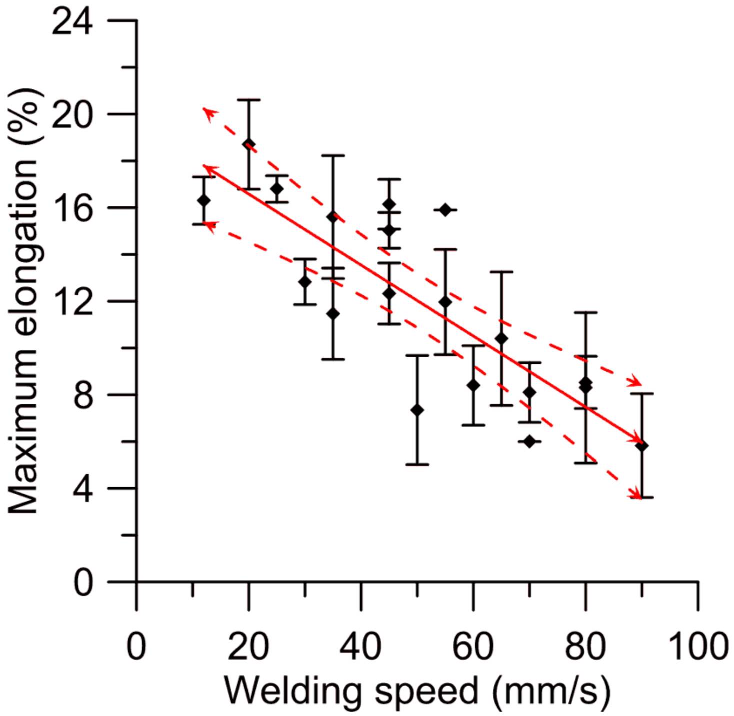

Figure 4.23: Effect of welding speed on maximum elongation.

Figure 4.22 is a plot of UTS vs. welding speed. UTS also falls rapidly with increasing welding speed. There is a gradual leveling-off in the curve; however, there is no distinct point of inflection, beyond which the UTS does not change. UTS values of above 180 MPa were recorded for welding speeds of 12 mm/s, falling to around 60 MPa for higher speeds.

Figure 4.23 is a plot of the maximum elongation achieved in the specimens, before failure. There is a reasonably linear trend of declining maximum elongation with increasing welding speed. Maximum strains range from 18 % for low speed welds at 12 mm/s, to around 6 % for high speed welds at 90 mm/s. In this plot, there is considerable variance in the results among some of the replicates, as witnessed by the error bars.

Solid lines indicate a best fit in all 3 plots. In Figure 4.21, 2 separate fit lines are used to account for the 2 distinct regions of the curve. In Figure 4.22, an exponential curve gives a better fit than a straight line. In Figure 4.23, a linear fit is the best model for the data. The dashed lines in all 3 plots represent the limits of the 95 % confidence interval. This can be interpreted as meaning that, if many more welds were tested, there is a 95 % chance that the test results would remain between the dashed lines.

In Figures 4.21 to 4.23, there is a strong correlation between the mechanical properties of the weld metal and the welding speed, where YS, UTS and maximum elongation all decrease with increasing welding speed. It can therefore be concluded that the best mechanical properties of the weld will be obtained by selecting the slowest possible welding speed and the lowest possible welding power.

It is known that an increase in welding speed results in a decrease in thermal gradient, G, at the weld pool tail, all else being equal [25]. It is therefore reasonable to ask how a lower thermal gradient might have affected the microstructure of the fusion zone, such that tensile properties would deteriorate. A closer look at the fusion zone microstructure, using higher magnification SEM and EDS elemental analysis, is shown in Figure 4.24, below.

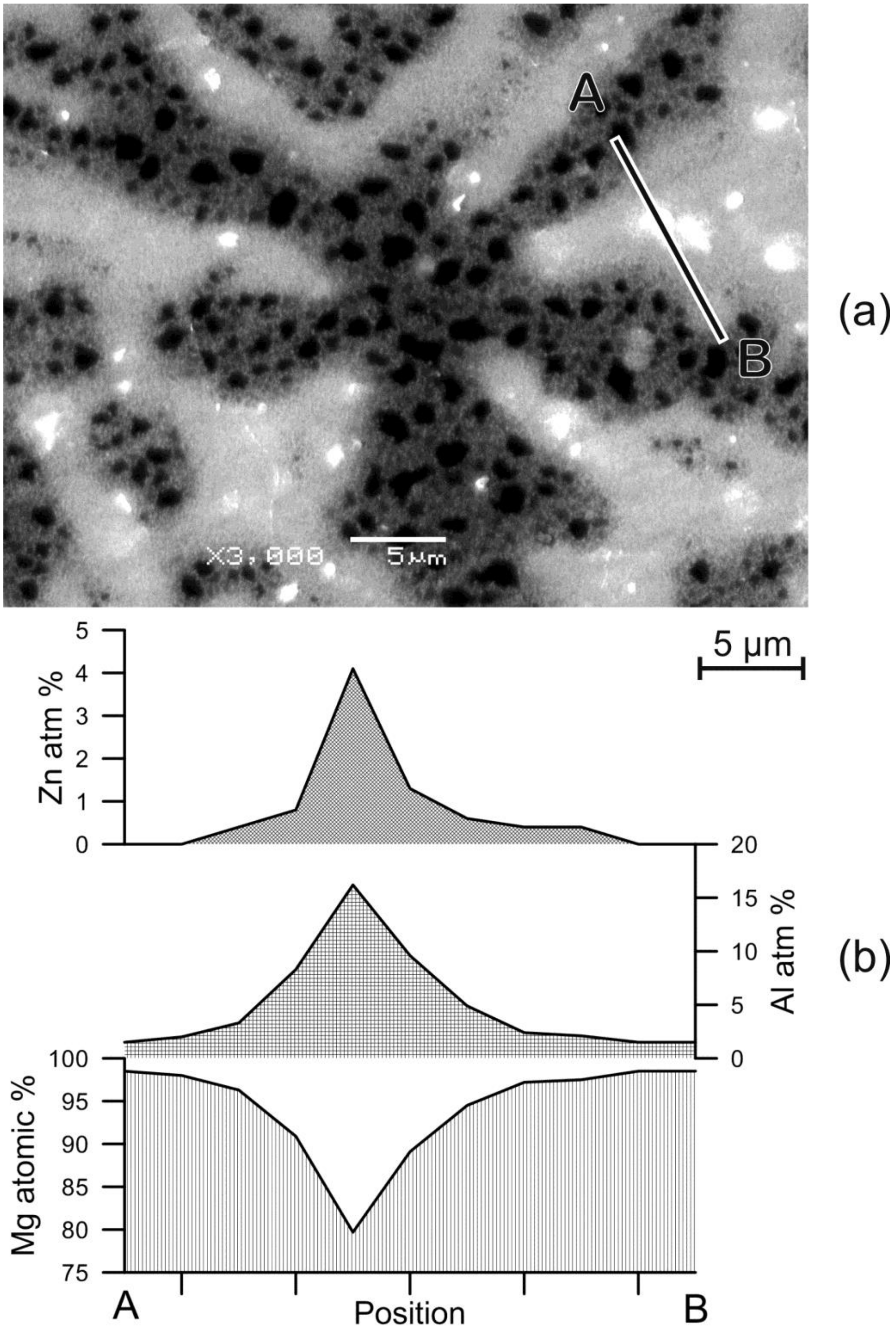

Figure 4.24: (a) High magnification SEM image of the dendritic microstructure in the weld fusion zone with (b) EDS line scans of Zn, Al and Mg elemental compositions, along the line A-B.

The SEM image in Figure 4.24a contains a characteristic, dark grey, 6-armed dendrite of solute lean, primary α-Mg surrounded by light grey, solute enriched α-Mg. There are also a number of white areas which correspond to $Mg_{17}(Al/Zn)_{12}$ β-phase particles in the interdendritic regions. Results from an EDS elemental line scan between points A and B, located on 2 adjacent dendrite arms, are plotted below the image, in Figure 4.24b. The results show increased levels of Aluminum and Zinc in the white particles and support the idea of β-phase forming in the inter-dendritic areas as a consequence of solute enrichment and alloy segregation.

It is necessary to examine and compare the composition of the fusion zones of welds made at different welding speeds, in order to determine why the mechanical properties depend so much on welding speeds. Figure 4.25 shows 2 SEM images of the fusion zone of 2 different welds: Figure 4.25a, made at a low welding speed of 12 mm/s and Figure 4.25b, made at a high welding speed of 90 mm/s. Both images are at the same scale, brightness and contrast, for comparison purposes.

The microstructures shown in Figures 4.25a & b both contain primary α-Mg dendrites (dark grey), enriched α-Mg between the dendrites (light grey) and some $Mg_{17}(Al/Zn)_{12}$ β-phase particles (white), at the grain boundaries. Differences between the microstructures include the relative amounts and morphology of these components. In the low speed weld (Figure 4.25a), the β-phase makes up 2.4 % of the area and is in the form of small, round, isolated particles. In the high speed weld (Figure 4.25b), the β-phase particles make up 4.5 % of the area and are in the form of interconnected, string or sheet-like structures that form along the grain boundaries. This is a significant difference in morphology, and could explain the decline in tensile properties with increasing welding speed.

Another difference is the area fraction of solute-lean α-magnesium dendrites, shown in dark gray. They occupy 25 % of the area of the slow speed weld and 37% of the area of the high speed weld. With a solute concentration of only around 1.5 wt%, they represent material that would have a lower yield stress than the more solute-rich areas and could reasonably be expected to contribute to a lower yield stress in the bulk weld metal. Conversely, the light gray areas represent a higher solute concentration (up to 13 wt%) in areas away from the dendrites. These areas can be expected to contribute to raising the yield stress in the bulk material.

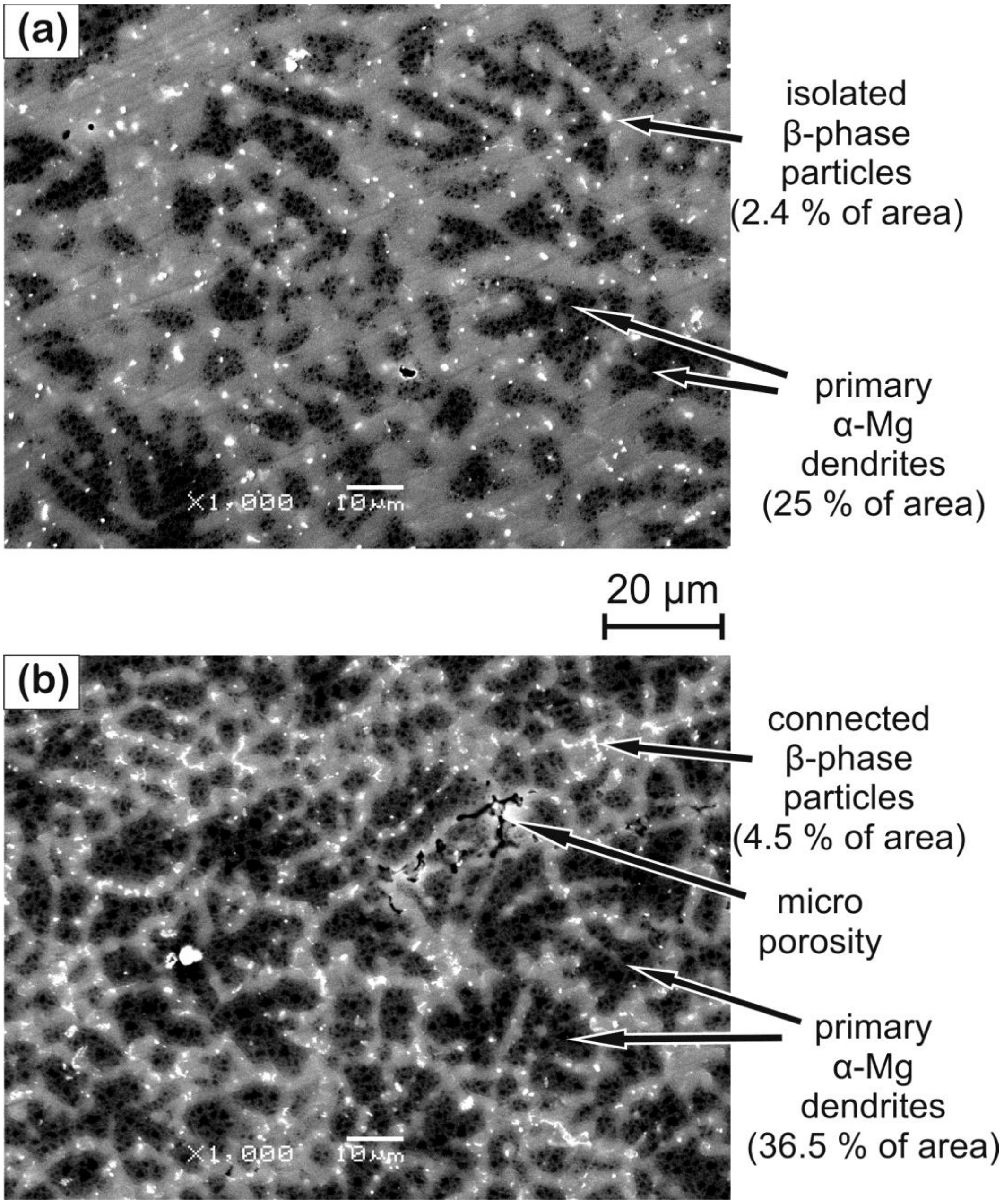

Figure 4.25: SEM images of the fusion zone microstructure: (a) welding speed 12 mm/s (b) welding speed 90 mm/s.

Some researchers [92] have suggested that the presence of hard β-phase particles contribute to higher yield strength in the bulk material, through the mechanism of Orowan strengthening. This can only be the case if the β-phase particles are very small, round and widely dispersed throughout the grains. However, this kind of morphology is not reported in the literature [21] [61] nor seen in the present experiments.

Figure 4.26 represents the left hand portion of the Mg-Al binary equilibrium phase diagram. Aluminum and zinc are mutually interchangeable as substitutional solute atoms in magnesium. The alloy AZ31B, therefore, can be reasonably represented as a Mg-4%(Al/Zn) binary alloy. AZ31B molten weld metal is shown on the diagram as a downward pointing blue arrow in the liquid region. The tie-line drawn horizontally from the liquidus indicates that the first solid to form will be α-magnesium, with about 1.5 wt% solute concentration. This agrees with the solute concentrations found in the center of the dendrites in Figure 4.24.

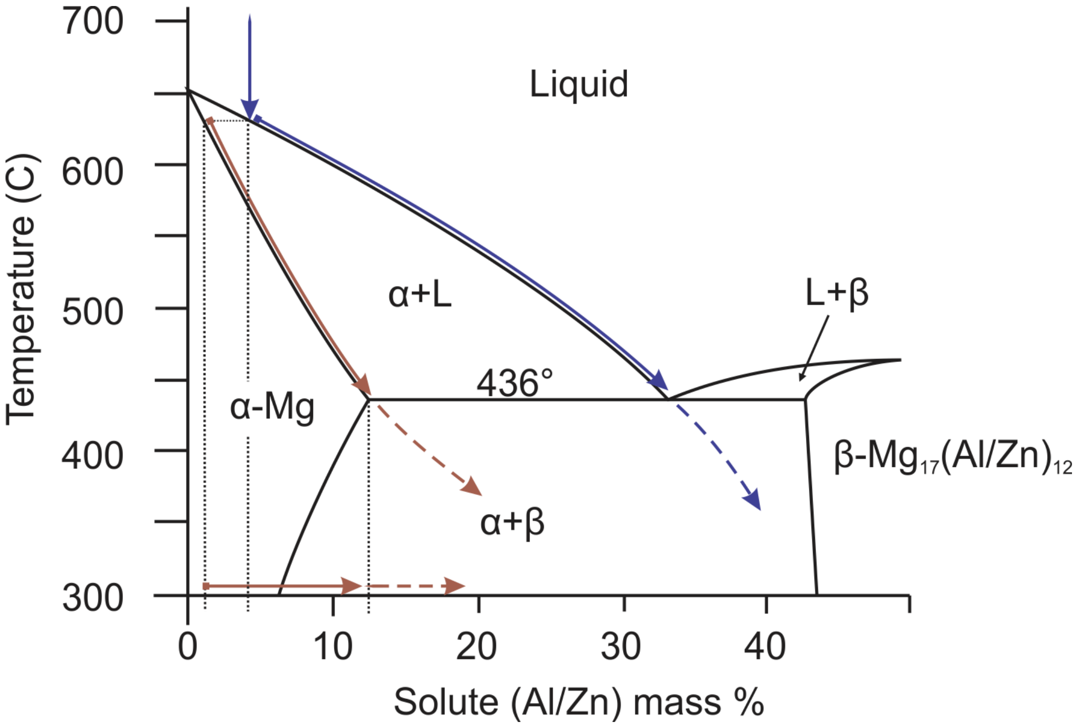

Figure 4.26: Left hand portion of the Mg-Al binary phase diagram. Adapted from ASM Handbook **[2]**.

As cooling and non-equilibrium solidification proceeds, the solid material increases in solute concentration, following the solidus line (shown in red) on the phase diagram. The remaining liquid becomes more and more solute-rich, as it follows the liquidus line (in blue) on the diagram. The volume of remaining liquid becomes very small, as solute segregation occurs. Once the solute concentration of the liquid exceeds 13 wt%, β-phase can nucleate along with the α-magnesium. The isolated pockets of solute-enriched liquid may achieve a high degree of undercooling before nucleation of the β-phase occurs, especially if the β-phase is not easily nucleated. In this case, the growth of the undercooled β-phase will be spontaneous, rapid and complete. There is no time for coupled eutectic growth to occur and the eutectic components take on a ‘divorced eutectic’ morphology, as is evident in Figures 4.21 and 4.25 [97].

The degree to which micro-segregation occurs during non-equilibrium solidification depends on the time available for diffusion in the solid [98] [99]. At low welding speeds, conditions at the solidification front are closer to equilibrium. The growth rate, R is low enough for significant diffusion to occur, which partially redresses the imbalance in solute concentration between the solid and the liquid. At higher welding speeds, the growth rate, R, is high enough that the solid has insufficient time to take up more solvent from the enriched liquid, before being too far from the solidification front, at too low a temperature, for significant diffusion to occur.

There are other differences between the microstructures shown in Figures 4.25a&b that would also play a role in affecting the mechanical properties of the weld. Small, solidification shrinkage micro-pores can be seen in the high speed weld, in some grain boundary areas. They coincide with locations of long strings of brittle, β-phase material and would certainly contribute to reduced mechanical properties in the weld. These pores would act as strain-localizers during deformation, provide crack initiation sites and would significantly decrease the ductility of the weld metal. The morphology of this type of porosity is quite different from the spherical shape of gas porosity and it has a more detrimental effect on mechanical properties. The long, narrow voids form along grain boundaries and provide initiation sites for cracking. Solidification shrinkage micro-porosity is caused by the specific volume change between liquid and solid that occurs on solidification and the restricted fluid flow through the interdendritic channels, during the last moments of solidification. Restricted fluid flow is more likely in the case of high welding speeds because the mushy zone of partially solidified metal in the tail of the weld pool is longer and the path of fluid flow more tortuous, than in the case of low speed welds. Some of the last liquid to freeze is not connected to the main pool of liquid metal or the free surface, but is trapped in isolated pockets. Shrinkage in the surrounding solid causes a drop in pressure in the last liquid pockets to freeze and micro-pores form. Although these solidification shrinkage micro-pores form as a result of specific volume change, they are still liable to fill with dissolved gases that may be present in the adjacent solid. As the partial pressure of the dissolved gas exceeds the low gas pressure in the micro-pore, the gas will come out of solid solution and enter the void. The key difference between gas porosity and shrinkage porosity is that gas porosity is formed earlier, when the metal is essentially liquid, and shrinkage porosity forms later, when the metal is almost solid [98]. Consequently, the 2 kinds of porosity have very different morphologies and shrinkage porosity is by far the more problematic, in terms of its effect on mechanical properties. Solidification shrinkage porosity can be reduced, and adequate mechanical properties maintained in the weld, by lowering the welding speed to achieve as short a weld pool tail as possible. The higher temperature gradient, G, of the low speed welds explains the absence of micro-pores in welds made at low speeds.

4.4 Summary of results

These experiments have demonstrated that the DSAW welding process, using plasma-arc welding torches, can be used to successfully join sheet AZ31B magnesium alloy in the butt-joint configuration. Thorough pre-weld material preparation was found to be essential. Any deficiencies in the cleaning or shielding of the magnesium would result in gas porosity and contamination of the weld by oxides. The parameter window of welding speed and welding power is fairly narrow for successful results. Parameters set outside of this window will result in either the formation of blowholes or an incomplete fusion defect. Secondary welding parameters of plasma gas flow rate and plasma torch orifice diameter were also found to be critical.

The quality of the welds was not uniform within the parameter window found to produce visually acceptable welds. The appearance of the welds deteriorated with increasing welding speed, as the weld profile progressively exhibited an undercut at higher welding speeds. Excessive spattering of the surface of the base metal also became evident at higher welding powers.

Hardness testing confirmed the formation of a HAZ near the weld and a fusion zone with lower hardness than the base metal. This softening is to be expected, as the metal is in the half-hard H-24 temper prior to welding and must inevitably revert to the fully annealed condition after welding. Transverse tensile testing of the welds resulted in joint efficiencies of around 80 %, a value similar to the difference in UTS between fully annealed and half-hard H-24 temper AZ31B. Other welding research involving this alloy has reported similar results.

Longitudinal tensile testing of exclusively the weld metal, revealed a more complex picture. Optimal mechanical properties were achieved at the lowest welding speed of 12 mm/s and the lowest welding power of 1.6 kW. Yield stress decreased with increasing welding speed up to around 40 mm/s. There was little further deterioration in mechanical properties at still higher speeds. The reason for this is unclear at this time.

Differences in microstructure were found between the low and high speed welds. High speed welds had a higher area fraction of brittle $Mg_{17}(Al/Zn)_{12}$ β-phase particles. Low and high speed welds also exhibited a different morphology of the β-phase particles. The β-phase particles in the low speed welds were small, round and more widely dispersed. In the high speed welds, the β-phase particles were larger, restricted to fewer sites and interconnected. They formed long, string or sheet-like structures at the grain boundaries and in between dendrite arms. This linear morphology of the β-phase has also been reported by others and would help to explain the reduced mechanical properties of the high speed welds. Solidification shrinkage micro-porosity was also observed in these same interdendritic areas in the high-speed welds. The key differences in microstructure and mechanical properties between the low and high speed welds are summarized in Table 4.4.

Table 4.4: Summary of different characteristics of the FZ metal in low and high speed welds.

	Low speed - Low power 12 mm/s 1.6 kW	High speed - High power 90 mm/s 5.0 kW
β-phase Area Fraction	2.4 %	4.5 %
β-phase Morphology	Small, round, widely dispersed particles	Larger, linear, interconnected in strings
Solute-lean α-Mg Dendrite Area Fraction	25 %	37 %
Micro-Porosity	Not observed	Clearly visible
Yield Stress	70 MPa	14 MPa
UTS	190 MPa	48 MPa
Max. Elongation	16 %	6 %

The mechanism that produces the differences in the area fraction of β-phase particles is solute enrichment of the liquid during non-equilibrium solidification, to the point where the eutectic products can form from the last liquid to solidify. At low welding speeds, there is sufficient time for diffusion to redress the imbalance in solute concentration between solid and liquid phases and less β-phase forms.

The mechanism that produces the solidification shrinkage micro-porosity in the high speed welds is related to different thermal gradients, G, in the weld pool tail, at different welding speeds. At low welding speeds, there is a fairly high thermal gradient at the tail of the weld. At higher welding speeds, the thermal gradient is lower. The low thermal gradient induces a longer mushy zone at the weld tail and a greater possibility of restricting the flow of the last liquid through the interdendritic channels, conditions which are known to be responsible for solidification shrinkage micro-porosity [98] [99].

Chapter 5

Summary and Conclusions

5.1 Summary of Research

Magnesium alloys are of interest to the automotive industry because of their low density, high specific strength and potential to reduce overall vehicle weight and fuel consumption. In order to incorporate more magnesium components into automotive structures, efficient welding and joining techniques must be developed. Specifically, an efficient method of making butt-joint configuration welds must be found in order to facilitate the use of sheet magnesium alloys in the form of tailor-welded blanks for structural applications. The existing welding processes, such as RSW, GTAW, GMAW, laser and hybrid laser-arc each have disadvantages when applied to magnesium alloy sheet.

The relatively new, double-sided arc welding (DSAW) process has been shown to produce high quality, full-penetration, conduction-mode, fusion welds in aluminum alloy sheet, for tailor-welded blank applications. The DSAW process has not yet been applied to AZ31B magnesium alloy, which has similar thermo-physical and oxide forming properties to aluminum alloys. Therefore, this research has explored the weldability of AZ31B magnesium alloy, using the DSAW process.

In this study, the DSAW process has been applied to the welding of AZ31B-H24 magnesium alloy sheet in the butt-joint configuration, as would be done when producing tailor-welded blanks in automotive manufacturing. The goals of the research were to:

1. Determine the range of welding speed and welding power that would result in visually acceptable welds.
2. Evaluate the influence of welding parameters on the visual appearance, mechanical properties and microstructure of the welds.

3. Explain any variation in mechanical properties in terms of the observed microstructure of the welds.

Experimental, double-sided, conduction-mode, autogenous welds were produced in 2 mm thick, rolled AZ31B-H24 magnesium alloy sheet, using a DSAW system equipped with 2 plasma-arc torches and associated control and data acquisition equipment. Successful welds were produced using welding speeds ranging from 12 mm/s to 100 mm/s and welding powers ranging from 1.6 kW to 8.7 kW. The welds were examined and characterized using standard metallographic techniques, mechanical testing and microstructural analysis.

5.2 Conclusions

As a result of these experiments, it can be concluded that the DSAW process is capable of producing acceptable, autogenous, butt-joint configuration welds in AZ31B magnesium alloy sheet, at welding speeds up to 100 mm/s. In order for the process to be successful, certain conditions are required. These conditions can be summarized as follows:

1. Heat input to the weld must be carefully controlled, through the primary process parameters of welding speed and welding power. There is a fairly narrow window of parameter combinations that results in successful welds. For the 2 mm thick sheet used in these experiments, a welding heat input of approximately 80 J/mm was required. Excessive heat input will result in blow-holes and insufficient heat input will result in partial joint penetration.
2. The magnesium alloy must be suitably prepared before welding. All traces of contamination, including the thin surface oxide layer, must be removed from the metal in the area of the weld, just prior to welding. In these experiments, both solvent degreasing and stainless steel wire wheel brushing of the metal in the weld vicinity were found to be necessary for successful welding. The metal was required to be brushed to a shiny lustrous finish in order to avoid

hydrogen gas porosity and oxide stingers in the weld. Any tendency towards hydrogen gas porosity or oxide stringers in the weld was progressively worse at higher welding speeds. These defects were observed only in welds made at speeds above 40 mm/s.

3. Shielding of the weld pool from the atmosphere must be complete. There must be no possibility of any contact between the hot weld pool and the atmosphere, otherwise oxide stringers and gas porosity will result.
4. Proper joint fit-up, in a rigid fixture with good clamping is required to resist the distortion that will otherwise occur. Any deficiency in the clamping arrangement is likely to result in a gap opening up between the sheets ahead of the weld. In that case, blowholes or edge pull-back are likely to occur and the 2 sheets will not weld together.

The overall weld quality varied considerably within the ranges of welding speed and welding power, giving acceptable welds. Appearance, geometry and mechanical properties of the welds were all degraded as welding speed and power were increased. The highest quality welds were achieved using a welding power of 1.6 kW and a welding speed of 12 mm/s, the lowest power possible, with the equipment used.

Weld appearance was determined by the degree of spatter forming on the surface of the base metal, adjacent to the weld. At the lowest welding speeds and powers, there was no spatter and a clean line at the weld toe separating the fusion zone from the base metal. As welding speeds and welding powers were increased, there was a progressive increase in the amount of observed spatter. Spatter can be attributed to the explosive boiling of the magnesium that can occur when a high power heat source is applied to the surface of magnesium. It can be concluded that the use of the lowest possible welding power, consistent with complete joint penetration, will result in the best weld appearance.

Weld geometry was determined by the degree of undercut and under-fill that was observed on the weld surface. At the lowest welding speeds and powers, there was no perceptible undercut or under-fill of the weld bead. As welding speeds and welding powers were increased, there was a progressive increase in the degree of undercut and under-fill. Under-fill can be attributed to the evaporative loss of magnesium that will be greater when a high power heat source is applied to the weld pool. Undercut is a known defect that occurs when welding at high speeds and forms a notch at the weld toe. Since magnesium is a notch-sensitive metal, undercut is a particularly undesirable welding defect for fatigue life.

The mechanical properties of the welds were optimum when welding speeds and welding powers were as low as possible. As welding speeds and powers were increased, there was a progressive decline in mechanical properties. Using a welding speed of 12 mm/s and power of 1.6 kW, the resulting weld metal had a yield stress of 70 MPa, a UTS of 190 MPa and a maximum elongation of 16 %. These values are close to those of the annealed base metal and represent properties that can reasonably be expected.

As the welding speed and welding power is increased, there is a progressive deterioration in the mechanical properties of the weld. Using a welding speed of 90 mm/s and power of 8.7 kW, the resulting weld metal properties were reduced to a yield stress of 14 MPa, a UTS of 48 MPa and a maximum elongation of 6 %. This represents a deterioration of mechanical properties, in the high speed weld metal, to values around a third of those in the low speed weld metal. It can therefore be concluded that the use of the lowest possible welding speed and power will result in the best possible mechanical properties in the weld metal.

The deterioration in mechanical properties in the high speed welds is associated with 2 microstructural features:

1. Formation of greater volumes of $Mg_{17}Al_{12}$ β-phase particles at high welding speeds than at low welding speeds. The observed volume fraction of β-phase rose from 2.4 % at a low

welding speed of 12 mm/s to 4.5 % at a high welding speed of 90 mm/s. The morphology of the β-phase particles also changed from being small, round, widely dispersed, individual particles in the low speed welds, to becoming larger, string-like, interconnected particles, formed along grain boundaries, in the high speed welds. Since β-phase particles are very brittle, they provide ready fracture paths along grain boundaries in the welds made at high speeds and cause the onset of inter-granular cracking, loss of strength and ductility. It can be concluded that the creation of greater volumes of β-phase particles, in string-like morphologies along grain boundaries, contributes to reduced mechanical properties in high speed welds.

2. Formation of solidification shrinkage micro-porosity in the interdendritic and inter-granular areas. The morphology of this type of porosity is quite different from the spherical shape of gas porosity and it has a more profound effect on mechanical properties. The long, narrow voids form along grain boundaries and provide initiation sites for cracking. Solidification shrinkage micro-porosity is caused by the specific volume change on solidification and the restricted fluid flow along the interdendritic channels, during the last moments of solidification. This is more likely to occur in the case of high welding speeds. It can be concluded that solidification shrinkage porosity can be reduced, and good mechanical properties maintained, by lowering the welding speed to achieve as short a weld pool tail as possible.

5.3 Recommendations for Future Work

Avoiding the problems caused by the brittle β-phase can be approached in 2 ways. Either the formation of the β-phase should be suppressed from forming, or decomposed, after it has formed. The former approach involves finding ways to limit solute segregation during non-equilibrium solidification and hence the enrichment of the small quantities of the last remaining liquid, to the stoichiometric ratio of the β-phase. The latter approach might involve a post-welding heat treatment of the entire weldment or a post weld heating and annealing pass of just the weld metal to promote dissolution of the non-equilibrium phase.

Solidification shrinkage micro-porosity is worsened by the low temperature gradient and consequent long mushy zone at the tail of high speed welds. Techniques to reduce solidification shrinkage micro-porosity, while keeping welding speeds high, might involve lowering the temperature in the material behind the weld. If the temperature gradient behind the weld could be increased, it would shorten the length of the mushy zone and alleviate the restricted fluid flow that causes shrinkage porosity.

Experimental research in the areas mentioned above would constitute a logical progression in the development of expertise in welding AZ31B magnesium alloy sheet. It would also be appropriate to extend the research to the joining of dissimilar thicknesses of AZ31B sheet, as would be common in tailor-welded blanks.

Appendix A: Data used to establish the process window shown in Figure 4.3.

Welding speed (mm/s)	Welding Power (kW)	Heat energy per unit length, H_J (J/mm)	Weld width (mm)	Result
10	1.3	130	3.9	Acceptable
10	1.8	180	6.0	Blow-holes
20	1.3	65	3.8	Acceptable
20	1.8	90	4.3	Acceptable
25	2.3	92	4.3	Acceptable
20	3.1	155	3.1	Blow-holes
35	2.3	66	3.3	Acceptable
40	1.8	45	3.2	Lack of fusion
40	2.3	58	3.5	Acceptable
40	3.1	78	3.9	Acceptable
40	4.1	103	4.1	Blowholes
60	2.3	38	2.3	Lack of fusion
60	3.1	52	3.6	Acceptable
60	4.1	68	4.1	Acceptable
60	5.0	83	4.4	Acceptable
60	5.5	92	4.3	Blow-holes
80	3.4	43	2.9	Lack of fusion
80	4.5	56	3.7	Acceptable
80	5.5	69	4.0	Acceptable
80	6.3	79	3.6	Acceptable
80	7.1	89	4.2	Blow holes

Welding speed (mm/s)	Welding Power (kW)	Heat energy per unit length, H_J (J/mm)	Weld width (mm)	Result
90	5.5	61	3.5	Acceptable
90	7.3	81	4.2	Acceptable
100	5.5	55	3.4	Lack of fusion
100	5.9	59	4.0	Acceptable
100	6.3	63	4.4	Acceptable
100	7.1	71	4.1	Acceptable
100	8.2	82	3.6	Acceptable
100	8.8	88	3.5	Acceptable
110	7.3	66	3.2	Acceptable
120	6.3	53	3.2	Lack of fusion
120	7.9	66	3.8	Lack of fusion

References

[1] S. Das, "Magnesium for Automotive Applications: Primary Production Cost Assessment," *Journal of Metals,* vol. 60, no. 11, pp. 22-26, November 2003.

[2] ASM Handbook Committee, "ASM Handbook, Volume 2: Properties and Selection: Nonferrous Alloys and Special-Purpose Materials," 10th ed., Materials Park, OH, ASM International, 1992.

[3] J. Jackman, J. Carpenter and N. Li, "Automotive Mg Research and Developement in North America," *Material Science Forum,* vol. 546, pp. 11-24, 2007.

[4] M. Kulekci, "Magnesium and its alloys applications in automotive industry," *Int'l Journal of Advanced Manufacturing Technologies,* vol. 39, no. 9, pp. 851-865, 2008.

[5] Magnesium Elektron, "Magnesium in Automotive," December 2012. [Online]. Available: www.magnesium-elektron.com.

[6] M. P. Groover, Fundamentals of Modern Manufacturing, 2nd ed., New York: John Wiley and Sons, Inc., 2002.

[7] H. Friedrich, "Research for a new age of magnesium in the automotive industry," *Journal of Materials Processing Technology,* no. 117, pp. 276-281, 2001.

[8] A. Kelkar, "Analysis of Aluminum in Autobody Designs and its Strategic Implications for the Aluminum Industry," MASc Thesis, Massachusetts Institute of Technology, Cambridge, Mass, USA, 2001.

[9] S. Schumann and H. Friedrich, "Automotive Applications of Magnesium in Europe," in *Magnesium Technology,* Berlin, Springer, 2004, pp. 499-630.

[10] S. Mariano, "Comparing Steel and Aluminum Automotive Structures by Technical Cost Modelling," *Journal of Metals,* vol. 45, no. 6, pp. 20-22, June 1993.

[11] E. Doege and K. Droder, "Sheet metal forming of magnesium wrought alloys — formability and process technology," *Journal of Materials Processing Technology,* vol. 115, pp. 14-19, 2001.

[12] E. Ghali, W. Dietzel and K. U. Kainer, "General and Localized Corrosion in Magnesium Alloys: A Critical Review," *Journal of Materials Engineering and Performance,* vol. 13, no. 1, pp. 7-23, February 2004.

[13] X. Cao, M. Jahazi, J. P. Immarigeon and W. Wallace, "A Review of Laser Welding Techniques for Magnesium Alloys," *Journal of Materials Processing Technology,* vol. 171, pp. 188-204, 2006.

[14] B. Rooks, "Tailor-welded blanks bring multiple benefits to car design," *Assembly Automation,* vol. 21, no. 4, pp. 323-328, 2001.

[15] E. A. Brandes and G. B. Brook, Eds., Smithell's Light Metals Handbook, Oxford, UK: Butterworth-Heinemann, 1998.

[16] S. Lee, "Thermal conductivity of Magnesium Alloys in the Temperature range of -125 to 400 C," *Intl. Journal of Thermophysics,* 2011.

[17] B. Mordike and P. Lukac, "Physical Metallurgy of Magnesium," in *Magnesium Technology,* Berlin, Springer, 2004, pp. 63-107.

[18] G. L. Song and Z. Q. Xu, "The surface, microstructure and corrosion of magnesium alloy AZ31 sheet," *Electrochimica Acta,* vol. 55, pp. 4148-4161, 2010.

[19] R. C. Zeng and K. U. Kainer, "Review of studies on corrosion of magnesium alloys," *Transactions of the Nonferrous Metals Society of China,* vol. 16, pp. 763-771, 2006.

[20] G. L. Song, "Corrosion electrochemistry of magnesium and its alloys," in *Corrosion of Magnesium Alloys*, Oxford, UK, Woodhead Publishing, 2011, pp. 3-34.

[21] L. Liu, Ed., Welding and joining of magnesium alloys, Oxford, UK: Woodhead Publishing, 2010.

[22] W. F. Smith, Structure and Properties of Engineering Alloys, New York: McGraw Hill, 1981.

[23] L. Xiao, L. Liu, Y. Zhou and S. Esmaeili, "Resistance-spot-welded AZ31 magnesium alloys: Part 1. Dependence of fusion zone microstructures on second phase particles," *Metallurgical and Materials Transactions A,* vol. 41A, pp. 1511-1522, June 2010.

[24] N. Hort, Y. Huang and K. U. Kainer, "Intermetallics in magnesium alloys," *Journal of Advanced Engineering Materials,* vol. 8, no. 4, pp. 235-240, 2006.

[25] S. Kou, Welding Metallurgy, Hoboken, NJ: John Wiley and Sons, Inc., 2003.

[26] R. E. Smallman and R. J. Bishop, Modern Physical Metallurgy and Materials Engineering, 6th ed., Oxford, UK: Butterworth-Heinemann, 1999.

[27] National Advisary Committee for Aeronautics, "Technical Note no. 842. Weather exposure tests of metals used in aircraft," NASA Archives, Washington, 1943.

[28] W. Helmut, R. Micheal and B. Belkacem, "Metal-inert gas welding of magnesium alloys," *Journal of Welding and Cutting*, vol. 55, no. 2, pp. 80-84, 2003.

[29] T. Bajor, Z. Muskalski and M. Suliga, "Research on the drawing process with a large total deformation wires of AZ31 alloy," in *Journal of Physics Conference Series: 15th International Conference on the Strength of Materials*, Dresden, Germany, August 2009, 2010.

[30] S. Zhou, L. Liu, J. P. Jung, M. Y. Lee and Y. Zhou, "Effects of Welding Parameters and Surface Pretreatments on Resistance Spot Welding of AZ31B Mg Alloy," *Metals and Materials International,* vol. 16, no. 6, pp. 967-974, 2010.

[31] Z. Wang, M. Gao, H. Tang and X. Zeng, "Characterization of AZ31B wrought magnesium alloy joints welded by high power fiber laser," *Materials Characterisation,* vol. 62, pp. 943-951, 2011.

[32] L. Liu, "Low power laser-arc hybrid welding behaviour in AZ based alloys," *Metallurgical and Materials Transactions A,* vol. 39A, pp. 1702-1711, July 2008.

[33] Y. M. Zhang and S. B. Zhang, "Method of arc welding using dual serial opposed torches.". US Patent 5,990,446, 23 Nov. 1999.

[34] Welding Handbook, Volume 2, Welding Processes, 8th ed., Miami, FL: American Welding Society, 1991.

[35] Y. M. Zhang and S. B. Zhang, "Double-sided arc welding increases weld joint penetration," *Welding Journal,* vol. 77, no. 6, pp. 57-61, 1998.

[36] Y. A. Kwon, "Double-sided arc welding of AA5182 alloy sheet," MASc thesis, University of Waterloo, Waterloo, Ontario, Canada, 2003.

[37] J. Moulton, "Double-sided arc welding of AA5182 aluminum tailor welded blanks," MASc thesis, University of Waterloo, Waterloo, Ontario, Canada, 2005.

[38] N. S. Joshi, "Double-Sided Arc Welding of AA5182 Aluminum Alloy Sheet in the Lap-Joint Configuration," MASc thesis, University of Waterloo, Waterloo, Ontario, Canada, 2010.

[39] Y. A. Kwon and D. C. Weckman, "Analytical thermal model of conduction mode double-sided arc welding," *Science and Technology of Welding and Joining,* vol. 13, no. 6, pp. 539-549, 2008.

[40] Y. A. Kwon and D. C. Weckman, "Double-Sided Arc Welding of 5182 Aluminum Alloy Sheet," *Science and Technology of Welding and Joining,* vol. 13, no. 6, pp. 485-495, 2008.

[41] J. A. Moulton and D. C. Weckman, "Double-Sided Arc Welding of AA5182-O Aluminum Sheet for Tailor Welded Blank Applications," *Welding Journal,* vol. 89, no. 1, pp. 11s-23s, 2010.

[42] H. J. Zhang, G. J. Zhang and L. Wu, "Effects of arc distance on angular distortion by asymmetrical double-sided arc welding," *Science and Technology of Welding and Joining,* vol. 12, no. 6, pp. 564-571, 2007.

[43] J. F. Lancaster, Ed., The Physics of Welding, 2nd ed., Oxford, UK: Pergamon Press, 1986.

[44] T. Q. Li, C. S. Wu, Y. H. Feng and L. C. Zheng, "Modelling the thermal fluid flow and keyhole shape in stationary plasma arc welding," *Int'l Journal of Heat and Fluid Flow,* vol. 34, pp. 117-125, April 2012.

[45] A. B. Short, D. G. McCartney, P. Webb and E. Preston, "Influence of nozzle orifice diameter in keyhole plasma arc welding," *Science and Technology of Welding and Joining,* vol. 16, no. 5, pp. 446-452, 2011.

[46] A. Punkari, "Variable Polarity Plasma Arc Welding and Dual-Beam Nd:YAG Laser Welding of Aluminum Alloys," MASc Thesis, University of Waterloo, Waterloo, Ontario, Canada, 2002.

[47] H. B. Cary, Modern Welding Technology, 5th ed., Upper Saddle River, NJ: Pearson Education, 2002.

[48] P. Fuerschbach, "Cathodic Cleaning and Heat Input in Variable Polarity Plasma Arc Welding of Aluminum," *Welding Journal*, vol. 77, no. 2, pp. 76 - 85, 1998.

[49] A. Roccaro, R. Filippo and M. Salato, "Application Note 1045: AC TIG Welding: Output Inverter Design Basics," International Rectifier, El Segundo, CA, USA, 2003.

[50] T. Okada, Y. Iwamoto, Y. Wakino, H. Yamamoto and K. Okazaki, "The effects of polarity in TIG arc welding of aluminum with thyristor controlled power source," *Journal of Light Metal Welded Construction*, vol. 16, no. 12, pp. 537-543, 1982.

[51] Welding Handbook Committee, "Magnesium and Magnesium Alloys," in *Welding Handbook Vol 3: Materials and Applications*, W. Oates, Ed., Miami, FL, American Welding Society, 1996, pp. 122-162.

[52] N. T. Williams and J. D. Parker, "Review of resistance spot welding of steel sheet," *International Materials Reviews,* vol. 49, no. 2, pp. 45-75, 2004.

[53] J. E. Gould, "Joining Aluminum Sheet in the Automotive Industry - A 30 Year History," *Welding Journal,* vol. 91, no. 1, pp. 23-34, Jan 2012.

[54] F. Czerwinski, "Welding and Joining of Magnesium Alloys," in *Magnesium Alloys - Design, Processing and Properties*, Published online - http://www.intechopen.com/books, In Tech, 2011, pp. 469-490.

[55] N. K. Babu, S. Brauser, M. Rethmeier and C. E. Cross, "Characterization of microstructure and deformation behaviour of resistance spot welded AZ31B magnesium alloy," *Science and Technology of Welding and Joining A,* vol. 549, pp. 149-156, 2012.

[56] L. Xiao, L. Liu, S. Esmaeili and Y. Zhou, "Microstructure Refinement After the Addition of Titanium Particles in AZ31 Magnesium Alloy Resistance Spot Welds," *Metallurgical and Materials Transactions A,* vol. 43A, pp. 598-609, Feb 2012.

[57] Y. N. Zhang, X. Cao, S. Larose and P. Wanjara, "Review of tools for friction stir welding and processing," *Canadian Metallurgical Quarterly,* vol. 51, no. 3, pp. 250-261, July 2012.

[58] Afrin, D. L. Chen and X. Cao, "Microstructure and tensile properties of friction stir welded AZ31B magnesium alloy joints," *Materials Science and Engineering A,* vol. 472, pp. 179-186, 2008.

[59] A. Kostka, R. S. Coelho, J. dos Santos and A. R. Pyzalla, "Microstructure of friction stir welding of aluminum alloy to magnesium alloy," *Scripta Materiaila,* vol. 60, pp. 953-956, 2009.

[60] L. Commin, M. Dumont, J. E. Masse and L. Barallier, "Friction stir welding of AZ31 magnesium alloy rolled sheets: Influence of processing parameters," *Acta Materialia,* vol. 57, pp. 326-334, 2009.

[61] G. Padmanaban, V. Balasubramanian and J. K. Sarin Sundar, "Influences of Welding Processes on Microstructure, Hardness and Tensile Properties of AZ31B," *Journal of Materials Engineering and Performance,* vol. 19, no. 2, pp. 155-165, 2010.

[62] G. Song and P. Wang, "Pulsed MIG welding of AZ31B Magnesium Alloy," *Materials Science and Technology,* vol. 27, no. 2, pp. 518-524, 2011.

[63] F. Koenigsberger and J. R. Adair, Welding Technology, New York: Hart Publishing, 1968.

[64] M. Rethmeier and S. Weisner, "Characteristic features of MIG welding of magnesium alloys," *Zeitschrift fur Metallkunde,* vol. 92, no. 3, pp. 281-285, 2001.

[65] M. Gao, X. Y. Zeng, B. Tan and J. C. Feng, "Study of laser-MIG hybrid welded AZ31 magnesium alloy," *Science and Technology of Welding and Joining,* vol. 14, no. 4, pp. 274-281, 2009.

[66] G. Song, P. Wang and L. Liu, "Study on ac-PMIG welding of AZ31B magnesium alloy," *Science and Technology of Welding and Joining,* vol. 15, no. 3, pp. 219-225, 2010.

[67] L. Liu and C. Dong, "Gas tungsten-arc filler wire welding of AZ31B magnesium alloy," *Material Letters,* vol. 60, pp. 2194-2197, 2006.

[68] N. K. Babu and C. E. Cross, "Grain Refinement of AZ31 Magnesium Alloy Weldments by AC Pulsing Technique," *Metallurgical and Materials Transactions A,* vol. 43A, pp. 4145-4154, November 2012.

[69] K. C. Mills, B. J. Keene, R. F. Brooks and A. Shirali, "Marangoni and Interfacial Phenomena in Materials Processing," *Philosophical Transactions: Mathematical, Physical and Engineering Sciences,* vol. 356, no. 1739, pp. 911-925, April 1998.

[70] Z. Sun, D. Pan and J. Wei, "Comparative evaluation of tungsten inert gas and laser welding of AZ31 magnesium alloy," *Science and Technology of Welding and Joining,* vol. 7, no. 6, pp. 343-351, 2002.

[71] G. Padmanaban, V. Balasubramanian and G. Madhusudhan Reddy, "Fatigue crack growth behaviour of pulsed current TIG, Friction Stir and laser welded AZ31B magnesium alloy joints," *Journal of Materials Processing Technology,* vol. 211, pp. 1224-1233, 2011.

[72] A. F. Hobbacher, "The new IIW recommendations for fatigue assessment of welded joints and components – A comprehensive code recently updated," *Int'l Journal of Fatigue,* vol. 31, pp. 50-58, 2009.

[73] R. S. Coehlo, A. Kostka, H. Pinto, S. Riekehr, M. Kocak and A. R. Pyzalla, "Microstructure and mechanical properties of magnesium alloy AZ31B laser beam welds," *Materials Science and Engineering A,* vol. 485, pp. 20-30, 2008.

[74] J. D. Kim, J. H. Lee and J. S. Kim, "Characteristics of Butt-Welded Joints on AZ31 Magnesium Alloy using a Nd:YAG Laser," *Int'l Journal of Precision Engineering and Manufacturing,* vol. 11, no. 3, pp. 369-373, 2010.

[75] S. M. Chowdhury, D. L. Chen, S. D. Bhole, E. Powidajko, D. C. Weckman and Y. Zhou, "Microstructure and Mechanical Properties of Fiber-Laser-Welded and Diode-Laser-Welded AZ31 Magnesium Alloy," *Metallurgical and Materials Transactions A,* vol. 42A, pp. 1974-1989, July 2011.

[76] J. Tusek and M. Suban, "Hybrid welding with arc and laser beam," *Science and Technology of Welding and Joining,* vol. 4, no. 5, pp. 308-311, 1999.

[77] C. Bagger and F. O. Olsen, "Review of laser hybrid welding," *Journal of Laser Applications,* vol. 17, no. 1, pp. 2-14, February 2005.

[78] B. Ribic, T. A. Palmer and T. DebRoy, "Problems and issues in laser-arc hybrid welding," *Int'l Materials Reviews,* vol. 54, no. 4, pp. 223-244, 2009.

[79] L. Liu and M. Chen, "Interactions between laser and arc plasma during laser–arc hybrid welding of magnesium alloys," *Optics and Lasers in Engineering,* vol. 49, pp. 1224-1231, 2011.

[80] M. Chen and L. Liu, "Study on Attraction of Laser to Arc Plasma in Laser-TIG Hybrid Welding on Magnesium Alloy," *IEEE Transactions on Plasma Science*, vol. 39, no. 4, pp. 1104-1109, April 2011.

[81] A. Mahrle and E. Beyer, "Hybrid laser beam welding - Classification, characteristics, and applications," *Journal of Laser Applications,* vol. 18, no. 3, pp. 169-180, August 2006.

[82] Y. M. Zhang, C. Pan and A. T. Male, "Improved microstructure and properties of 6061 aluminum alloy weldments using a double-sided arc welding process," *Metallurgical and Materials Transactions A,* vol. 31A, no. 10, pp. 2537-2543, Oct 2000.

[83] Y. M. Zhang, C. Pan and A. T. Male, "Solidification behaviour of Al-Mg aluminum alloy using double-sided arc welding process," *Journal of Materials Science Letters,* vol. 19, pp. 831-833, 2000.

[84] G. F. Vandervoort, Ed., Metallography Principles and Practice, Materials Park, OH, USA: ASM International, 1999.

[85] ASTM E92, Standard Test Method for Vickers Hardness of Metallic Materials, West Conshohocken, PA: ASTM Int'l, 2003.

[86] ASTM E8M-04, Standard Test Method for Tension Testing of Metallic Materials, West Conshohocken, PA: ASTM Int'l, 2004.

[87] W. Milek, P. B. Dickerson, D. D. Rager and W. W. Sanders, "Ch. 5: Design for Welding," in *Welding Handbook, 8th Edition Vol 1: Welding Technology*, Miami, FL, American Welding Society, 1987, pp. 125-216.

[88] J. Campbell, Castings, 2nd ed., Oxford, UK: Butterworth-Heineman, 2003.

[89] T. C. Nguyen, D. C. Weckman, D. A. Johnson and H. W. Kerr, "High speed fusion weld bead defects," *Science and Technology of Welding and Joining,* vol. 11, no. 6, pp. 618-633, 2006.

[90] E. Soderstrom and P. Mendez, "Humping mechanisms present in high speed welding," *Science and Technology of Welding and Joining,* vol. 11, no. 5, pp. 572-579, 2006.

[91] H. Iwasaki, "Fatigue of Welded Magnesium Joints," *Materials Transactions,* vol. 45, no. 2, pp. 419-422, 2004.

[92] H. G. Dong, C. Q. Liao and L. Q. Yang, "Microstructure and mechanical properties of AZ31B magnesium alloy gas metal arc weld," *Trans. Non-ferrous metals Soc. of China,* vol. 22, pp. 1331-1336, 2012.

[93] S. Felicelli, L. Wang and M. Claudio, "A Model for Gas Microporosity in Aluminum and Magnesium Alloys," *Metallurgical and Materials Transactions B,* vol. 40B, no. 2, pp. 169-180, April 2009.

[94] David Porter, Kenneth Easterling and Mohamed Sherif, Phase Transformations in Metals and Alloys, Boco Raton, FL, USA: CRC Press, 2009.

[95] The Aluminum Association, Qualification standard for structural welding of aluminum, B. Altshuller, Ed., Washington: The Aluminum Association, 1988.

[96] R. Smerd, S. Winkler, C. Salisbury, M. Worswick, D. Lloyd and M. Finn, "High strain rate tensile testing of automotive aluminum alloy sheet," *Intl. Journal of Impact Engineering,* vol. 32, no. 1-4, pp. 541-560, Dec 2005.

[97] M. S. Dargusch, M. Nave, S. D. McDonald and D. H. StJohn, "The effect of aluminium content on the eutectic morphology of high pressure die cast Mg-Al alloys," *Journal of Alloys and Compounds,* vol. 492, pp. L64-L69, 2010.

[98] M. C. Flemings, Solidification Processing, New York: McGraw-Hill, 1974.

[99] J. A. Dantzig and M. Rappaz, Solidification, Boca Raton, Fl: CRC Press, 2009.